Micromachined Capacitive Silicon Bulk Acoustic Wave Gyroscopes

A Dissertation
Presented to
The Academic Faculty

By

Houri Johari

In Partial Fulfillment
Of the Requirements for the Degree
Doctor of Philosophy in the
School of Mechanical Engineering

Georgia Institute of Technology

December 2008

Micromachined Capacitive Silicon Bulk Acoustic Wave Gyroscopes

Approved by:

Professor Farrokh Ayazi, Advisor
School of Electrical and Computer Engineering
Georgia Institute of Technology

Professor F. Levent Degertekin, ME advisor
School of Mechanical Engineering
Georgia Institute of Technology

Professor Peter J. Hesketh
School of Mechanical Engineering
Georgia Institute of Technology

Professor Suresh K. Sitaraman
School of Mechanical Engineering
Georgia Institute of Technology

Professor Paul Kohl
School of Chemical and Bimolecular Engineering
Georgia Institute of Technology

Date Approved:

10/28/2008

I dedicate this dissertation to my loving mom for
her support, encouragement, and wisdom.

ACKNOWLEDGMENTS

I would like to express my deep appreciation and sincere gratitude to my mentor and advisor, Professor Farrokh Ayazi for his guidance, support and encouragement. I have been honored to work under his supervision and learn from his advice and useful insights throughout my PhD program.

I would like to thank my dissertation defense committee members, Professor Levent Degertekin, Professor Peter Hesketh, Professor Suresh Sitaraman and Professor Paul Kohl for their interest in my work. It has been a great privilege to benefit from their input and help in construction of my dissertation.

This research would not have been enabled without any single help and support that I had received from each of my colleagues in Integrated MEMS Laboratory at Georgia Tech. Particularly, I would like to thank my former colleagues Dr. Siavash Pourkamali, Dr. Reza Abdolvand and Dr. Pejman Monajemi for their help and invaluable discussions in MEMS fabrication, Dr. Babak Vakili Amini and Dr. Ajit Sharma for their kindest help in testing. Also, my special thanks go to my lab-mates, Jalpa Shah and Milap Dalal who have been primarily responsible for the development of the interface electronics. In addition, I would like to thank all the staffs, especially Mr. Gary Spinner and Mr. Tran-Vinh Nguyen, of the Microelectronics Research Center cleanroom at the Georgia Institute of Technology for all their help and hard work.

Finally, I thank my lovely family particularly my dear mom for their invaluable supports and encouragements. Last but not least, I wish to thank my fiancé, Mr. Preston Galle, for all his help, support and positive attitude during the course of my graduate studies.

TABLE OF CONTENTS

LIST OF TABLES

LIST OF FIGURES

LIST OF SYMBOLS

α	Thermal expansion coefficient
α_1	The coefficient matrix in eignvalue solver in COMSOL
a	The coefficient matrix in eignvalue solver in COMSOL
$a_{Coriolis}$	Coriolis acceleration
ARW	Angle random walk
A_1	The drive amplitude constant
A_2	The sense amplitude constant
A_g	Angular gain
A_v	Voltage amplifier gain
β	A Coefficient in out-of-plane mode equations
β_1	The coefficient matrix in eignvalue solver in COMSOL
$\beta_{rotation\text{-}angle}$	The angle of rotation
BW	Frequency bandwidth
C	Specific heat density
C_1	The coefficient matrix in eignvalue solver in COMSOL
C_0	Initial capacitance
C_1	The damping coefficient at the drive
C_2	The damping coefficient at the sense
C_d	Capacitance between the drive electrode and the disk
$C_{effec\text{-}mass}$	Effective mass coefficient
C_{pad}	Pad capacitance
$C_{parasitic}$	Parasitic capacitance
C_s	Capacitance between the sense electrode and the disk
C_x	Damping in x direction
C_y	Damping in y direction
D_1	Generalized force at the drive
D_2	Generalized force at the sense
d_a	The coefficient matrix in eignvalue solver in COMSOL
D_0	The initial capacitive gap
Δd	The capacitive gap change
Δf	The frequency split between two modes
$\Delta\theta_n$	The electrode angle spans
δC	The capacitance change
E	Young's modulus
ε_0	Electric constant (8.85×10^{12} F/m)
ε_r	Normal strain in r direction
ε_θ	Normal strain in θ direction
ε_z	Normal strain in z direction
η	Thermoelastic coefficient
ϕ	The normalized x-direction coordinate
ϕ_{r1}	The drive mode shape function at r direction
ϕ_{r2}	The sense mode shape function at r direction

$\phi_{\theta 1}$	The drive mode shape function at θ direction
$\phi_{\theta 2}$	The sense mode shape function at θ direction
F_1	The electrical forces at the drive mode
F_2	The force at the sense mode
f	The natural frequency
f_{Corilios}	The Coriolis frequency
$F0drive$	The amplitude for the drive force
$Fdrive$	The drive force
γ	Coriolis coefficient
γ_1	The coefficient matrix in eignvalue solver in COMSOL
$\gamma_{r\theta}$	Shear strain in $r\theta$ direction
γ_{rz}	Shear strain in rz direction
$\gamma_{z\theta}$	Shear strain in θz direction
h	Disk thickness
h_m	Frequency parameter
Im	Imaginary part
I_{noise}	Input referred noise
I_s	The output current from the sense
φ	The normalized y-direction coordinate
J_m	Bessel function
κ	Thermal conductivity
K	The scale factor to normalize the position
k	A Coefficient in out-of-plane mode equations
k_B	Boltzmann constant (1.38×10^{-23} J/K)
K_{e1}	Electrical stiffness at the drive mode
K_{e2}	Electrical stiffness at the sense mode
k_m	Frequency parameter
K_{m1}	Mechanical stiffness at the drive mode
K_{m2}	Mechanical stiffness at the sense mode
K_x	Stiffness in x-direction
K_y	Stiffness in y-direction
λ	Lame coefficient
Le	The electrode length
m	Mode number
μ	Lame coefficient
M_1, M_2, M	Total mass
ν	Linear velocity
Q	Quality factor
q_1, q_{drive}	Drive amplitude
q_2	Sense amplitude
Q_{EFF}	Effective quality factor
Q_{TED}	Thermoelastic damping quality factor
R	Disk radius
r	Radial direction in cylindrical coordinate
ρ	Mass density
Re	Real part

R_f	The gain at the TIA amplifier
ψ	The normalized *z*-direction coordinate
θ	Tangential direction in cylindrical coordinate
σ_r	Normal stress in *r* direction
σ_θ	Normal stress in θ direction
σ_z	Normal stress in *z* direction
T_i, T	Kinetic energy
t	Time
T	Temperature
$\overline{T}$	The normalized temperature
T_0	Absolute temperature
T_{init}	Initial temperature
τ	Normalized time coefficient
$\tau_{r\theta}$	Shear stress in $r\theta$ direction
τ_{rz}	Shear stress in rz direction
$\tau_{\theta z}$	Shear stress in θz direction
θ_l	The vibration pattern angle
θ_n	The angle from the *x*-axis to the center of the *n*th electrode
υ	Poisson ratio
U_i	Potential energy
u	Displacement
$\bar{u}$	The normalized displacement
u_0	Normalized displacement coefficient
U_e	Electrical potential energy
u_ϕ	Displacement at the normalized ϕ direction
u_φ	Displacement at the normalized φ direction
U_m	Mechanical potential energy
U_r	Maximum dimensionless displacement in *r* direction
u_r	Displacement in *r* direction
U_θ	Maximum dimensionless displacement in θ direction
u_θ	Displacement in θ direction
u_ψ	Displacement at the normalized ψ direction
V	Volume
v	Velocity
V_d	The voltage between the drive electrode and the disk
$v_{d\text{-}ac}$	The ac signal the drive voltage
v_{out}	Output voltage
V_p	Polarization voltage
V_s	The voltage between the sense electrode and the disk
V_{Td}	The voltage between the tuning drive electrode and the disk
$V_{T\text{-}drive}$	Tuning voltages for the drive
V_{Ts}	The voltage between the tuning sense electrode and the disk
$V_{T\text{-}sense}$	Tuning voltages for the sense
Ω_x	Rotation rate around *x*-axis
Ω_y	Rotation rate around *y*-axis

Ω_z	Rotation rate around *z*-axis
Ω_{min}*(Brownian)*, MNEΩ	Mechanical (Brownian) noise, Mechanical noise equivalent
Ω_{min}(Electronic), ENEΩ	Electronic noise, Electronic noise equivalent
Ω_{min}(Total), TNEΩ	Total noise, Total noise equivalent
ω_0	Natural angular Frequency
ω_{drive}	The drive angular frequency
ξ	The elastic wave constant ratio
χ	A Coefficient in out-of-plane mode equations

SUMMARY

Gyroscopes are angular velocity sensors that are used for measuring rate or angle of rotation. The application domain of silicon microgyroscopes is quickly expanding from automotive to aerospace and consumer electronics industries. Examples include anti-skid and safety systems in cars, inertial measurement units (IMUs), image stabilization in digital cameras, and smart user interfaces in handheld devices. As potential high volume consumer applications for micromachined gyroscopes continue to emerge, design and manufacturing techniques that improve the performance, reliability and shock survivability of gyroscope while providing multi-axial functionality become increasingly important.

Today, state-of-the-art silicon micromachined vibratory gyroscopes can achieve high performance with low operational frequency (3-30kHz) at the cost of large form factor, high operating voltages and very low pressure package environment. Additionally, temperature compensation is required to guarantee stable performance over temperature. These all add up to make the finished product elaborate and costly. In this dissertation, capacitive bulk acoustic wave (BAW) silicon disk gyroscopes are introduced as a new class of micromachined vibratory gyroscope to investigate the operation of Coriolis-based gyroscopes at high frequency and further meet consumer electronics market demands. Capacitive BAW gyroscopes, operating at high frequency of 1-10MHz, are stationary devices with vibration amplitudes less than 20nm, resulting in high operational bandwidth and high shock tolerance, which are generally unavailable in low frequency gyroscopes. BAW gyroscopes require low operating voltages, which simplifies the interface circuit design and implementation in low-voltage CMOS technologies. They

also demonstrate appropriate thermally-stable performance in air, which eliminates the need for vacuum packaging and temperature compensation, resulting in superior reliability and reduced cost.

This dissertation presents the design, implementation and characterization of z-axis capacitive BAW disk gyroscopes in (100) and (111) single crystal silicon. A revised high aspect-ratio poly- and single crystalline silicon (HARPSS) process was utilized to implement these devices in thick silicon-on-insulator (SOI) substrates (35-60μm) with very small capacitive gap sizes (~200 nm). The prototype devices show ultra-high quality factors (Q) in excess of 200,000 and large bandwidth of 15-30Hz under very high-Q mode-matched condition. The measured rate sensitivity for a 6MHz-disk gyroscope with $Q_{\text{matched-mode}}$ of 235,000 was 270μV/°/sec in (100) silicon.

Another major contribution of this dissertation is to optimize the design and implementation of BAW disk gyroscopes for self-matched mode operation. Operating a vibratory gyroscope in matched mode is a straightforward way to improve performance parameters. But, it is very challenging to achieve without applying large voltages, which are difficult to generate with CMOS electronics. In this work, self-matched mode operation was provided by enhanced design of the perforations of the disk structure. In addition, the operating frequencies of the secondary elliptic modes were high enough to marginalize air damping losses. At the same time, the high operating frequency offers a very large device bandwidth of ~ 400Hz when these devices are operated in air. The rate sensitivity of the optimized device in air was measured to be 65μV/°/sec for a 7.3MHz device with $Q_{matched\text{-}mode}$ of 15,000. In addition, these most advanced devices were characterized over a typical consumer electronics temperature range. It was observed that

the modes remained matched and the measured Q and scale factor demonstrate the high performance stability of BAW gyroscopes even at elevated temperatures.

To complete this thesis, a gyroscope with planar-axis sensitivity (x-axis) is developed as an extension of the *z*-axis BAW gyroscope design. The x-axis gyroscope uses out-of-plane modes of a silicon disk structure. A rate sensitivity of 73μV/°/sec around the *x*-axis was measured for this device with a $Q_{matched\text{-}mode}$ of 17,000 in (100) silicon. A multi-axis single-proof-mass gyroscope was introduced to measure the rotation rate around the *x* or *y*-axis and the *z*-axis by operating in in-plane and out-of plane modes. Like the single-axis devices, these gyroscopes were also optimized to achieve self-matched mode operation. The optimized multi-axis gyroscope exhibits matched in-plane mode and out-of-plane modes.

In conclusion, the experimental results establish the suitability of BAW gyroscopes for consumer electronic applications.

CHAPTER 1

INTRODUCTION

1.1 APPLICATION AND MARKET DEMAND

A gyroscope is a sensor that measures the rate or angle of rotation. Micromachined gyroscopes have the potential to dominate the rate-sensor market mainly due to their small size, low power and low cost. The application domain of micromachined gyroscopes is quickly expanding from automotive to aerospace and consumer electronic industries [1]. A multitude of applications exist in the automotive sector including navigation, anti-skid, roll-over detection, next generation airbag and anti-lock brake (ABS) systems [2]. Micro-gyroscopes can also be used for inertial navigation. Inertial navigation is the process of determining an object's position based on measurements provided by accelerometers and gyroscopes contained within the object. An inertial measurement unit (IMU) typically uses three accelerometers and three gyroscopes oriented along their respective sensing axes to gather information about an object's direction and heading. IMUs are vital components in aircraft, GPS-augmented navigation, and personal heading references [3]. In addition, there are numerous emerging consumer applications for micro-gyroscopes, including image stabilization in digital cameras, smart user-interfaces in handhelds, gaming and inertial pointing devices [4]. As potential high volume consumer applications for micromachined gyroscopes continue to emerge, design and manufacturing techniques that improve their

performance, shock survivability, and reliability without driving up the cost are becoming increasingly important.

Today, state-of-the-art micromachined vibratory gyroscopes operate in flexural modes, which typically occur in the frequency range of 3-30 kHz [5]. In these gyroscopes, resolution, the primary performance parameter, is limited by the mechanical noise floor (Brownian noise). The Brownian noise depends inversely on the drive amplitude (q_{drive}) and the square roots of the resonant frequency (ω_0) and the mass (M). Although all three above parameters should be maximized to lower the mechanical noise floor, the linear relationship between the electronic noise floor and resonance frequency has driven classical optimizations towards focusing on only the mass and drive amplitude [6-9]. Increasing the mass and drive amplitude results in large form factors and exceedingly high operating voltages.

The next most critical gyroscope performance parameters are scale factor and bias drift. These are directly affected by the mechanical quality factor (Q) which is a measure of energy dissipation in a vibratory structure. A gyroscope with a higher Q is universally desired since a higher Q in a gyroscope translates into larger scale factor and better bias stability. Although low frequency gyroscopes can achieve quality factors on the order of 50,000 in high vacuum (1-10mTorr) and room temperature, their quality factors are severely limited by air damping and thermoelastic damping (TED) [10]. The quality factor of these devices in low vacuum or at atmospheric pressure falls to less than 100. On the other hand, even in high vacuum, thermoelastic damping presents a dominant loss mechanism at elevated temperature [11]. These factors are enough to predicate the high performance of low frequency gyroscopes upon a narrow operating environment (high

vacuum pressure and room temperature). Thus, these devices must be packaged in a high vacuum, making the finished device costly. Also, corresponding to their required performance, these devices might need to be integrated with a temperature controller. This adds further cost and more complexity to these products.

Major evolutions in low frequency flexural gyroscopes have refined the performance of these devices to inertial grade [11-12], but at the cost of large form factors, high operating voltages, and expensive, constrained environmental conditions. Although these issues might not be crucial in high-precision markets such as the defense, navigation and space industries, they likely present prohibitive concerns in high volume markets such as consumer electronics [13]. At the same time, numerous consumer applications require gyroscopes with fast response time and high shock survivability, which is generally unavailable in current low frequency gyroscopes. All these demands call for innovative designs and major advances in fabrication technology to offer more broadly practical gyroscopes.

Besides single-axis gyroscopes, multi-axis silicon gyroscopes find growing applications in consumer electronics and handheld devices. They are increasingly required to have high performance, small size, and low power consumption. To date, commercialized multi-axis vibrating gyroscopes [14, 15] utilize multiple proof masses for detecting rotation rates around multiple axes. Consumer applications require stable high performance multi-axis gyroscopes with small form factor, fast response time and high shock survivability, which is generally unavailable at low cost in low frequency vibrating gyroscopes. Thus, proposing multi-axis gyroscopes that fulfill the above requirements in reduced cost would make a difference in the consumer electronic industry.

1.2 MOTIVATION

The objective of this thesis is to investigate the operation of Coriolis-based vibratory gyroscopes at high frequency. To do this, a new class of micromachined gyroscope, a capacitive silicon bulk acoustic wave (BAW) gyroscope, is introduced and further developed in this dissertation.

A capacitive BAW gyroscope provides a novel approach to break through the Brownian noise constraint on the resolution in current low-frequency gyroscopes. The mechanical noise floor is improved by

(1) increasing the resonant frequency by 2 to 3 orders of magnitude to 2-8 MHz, instead of increasing the mass and drive amplitude, and

(2) substantially increasing and thermally stabilizing the Q by utilizing stiff bulk acoustic modes, which experience significantly less thermoelastic damping compared to flexural modes.

The very high value and low thermal sensitivity of Q in the bulk acoustic modes will further translate into superior bias stability, even at elevated temperatures.

The elimination of the Brownian noise constraint in BAW gyroscopes removes high mass and large vibration amplitude as central design goals, freeing these devices to be designed for minimal form factors and operating voltages. The proposed BAW gyroscopes have a smaller form factor compared with current commercialized gyroscopes (e.g., ADXRS150 by Analog Devices [16] and IDG1004 by InvenSense [17]). Operating gyroscopes in their BAW modes makes them substantially stiff with vibration drive amplitudes less than 20nm. Due to their very small drive amplitudes, they require very low operating DC

voltages (V_p<5V) as well as AC actuation voltages (160mV). This facilitates the interface circuit design and implementation of these devices in standard 5V CMOS. In addition, the large stiffness of BAW gyroscopes makes them less sensitive to environmental pressure, obviating the need for vacuum encapsulation. This simplifies wafer-scale packaging for reduced manufacturing cost.

Additional concerns in gyroscope applications include device bandwidth ($f_0/2Q$), shock survivability and flicker noise ($1/f_0$). Due to the high frequency operation of BAW modes, these devices offer large device bandwidth, ~15-30Hz, under high-Q, matched-mode condition, while flexural modes, due to their significantly lower frequencies, limit the device bandwidth to sub-Hz values in their high matched mode Q. In consumer electronic gyroscopes applications, reliability is strongly determined by shock resistance. Since BAW gyroscopes are solid-state devices with very large stiffness and small drive amplitude, they exhibit superior shock resistance. Furthermore, flicker noise which occurs in the operating resonance frequency of less than 100kHz is not a concern in high frequency BAW gyroscopes.

The next goal of this dissertation is to optimize the design and implementation of BAW disk gyroscopes to achieve self-matched mode, operation in air, and very large bandwidth. The self-matched mode operation is provided through an enhanced design of the perforations of the disk structure, removing considerable complexity from the interface circuitry. Operating these devices in the MHz frequency range of their matched-mode in air can also offer very large bandwidth of ~400Hz. In addition, the operating frequency of the secondary elliptic modes in these optimized disks is high enough to mitigate air damping losses. This eliminates the need for vacuum packaging, resulting in

better long-term reliability and substantially reduced cost. Furthermore, these optimized devices demonstrate very high thermal stability of their matched-mode Q and scale factors, resulting in no need for a temperature controller.

The ultimate aim of this dissertation is to design and implement multi-axis gyroscopes. A *z*-axis BAW gyroscope is extended into a multi-axis gyroscope. This novel approach can potentially achieve multi-axis gyroscopes using a single-disk and eliminate the issues with integration of multiple proof masses, resulting in a very small form factor. Also, from the *z*-axis BAW gyroscope design, the multi-axis devices inherit high shock tolerance and large frequency bandwidth. The multi-axis disk gyroscopes operate in in-plane and out-of plane modes to enable measurement of rotation rate around *x*-axis or *y*-axis as well as *z*-axis. The operating frequency is in the range of 1-8MHz for both in-plane and out-of plane modes. Due to their high frequency of operation, these devices also show reduced susceptibility to common damping mechanisms. This affords them very high, thermally-stable quality factors without the typically required high vacuum environment, and the associated packaging, manufacturing, and reliability complications.

In this dissertation, the design, implementation and characterization of micromachined capacitive bulk acoustic wave silicon disk gyroscopes were investigated. In order to fully realize the potential of BAW gyroscopes as attractive replacements to current gyroscopes in consumer electronic application, the overall performance of these devices are precisely studied and discussed in this dissertation.

1.3 DISSERTATION ORGANIZATIONS

This dissertation is organized in seven chapters. **CHAPTER 1** outlines the application and market demand for micromachined gyroscopes and presents the motivation behind this work. **CHAPTER 2** reviews the history of micromachined vibratory gyroscopes presented in literature and studies the multi-axis gyroscopes as well as the commercialized MEMS gyroscopes. **CHAPTER 3** starts by introducing capacitive silicon bulk acoustic wave (BAW) gyroscopes and continues with an explanation of their principles of operation. The focus of this chapter is the design and modeling of BAW disk gyroscopes, operating in their elliptic degenerative modes. At the end, thermoelastic damping is modeled and the Q_{TED} is estimated for these devices employing multiphysics in COMSOL. **CHAPTER 4** introduces the fabrication features and process flow to enable the implementation of BAW disk gyroscopes in SOI substrates. Also, the critical fabrication steps were explained in details. **CHAPTER 5** starts by explaining the experimental test setups and procedures used for the measurements. The measurement results for BAW gyroscopes implemented in both (111) and (100) single crystal silicon are further presented. This includes the frequency responses of these devices as well as the performance characterization. In addition, the optimized design and implementation of BAW gyroscopes in single crystal silicon are presented in this chapter. This is aimed at minimizing the frequency separation between the two modes, consequently facilitating the matched-mode operation along with the operation in air. **CHAPTER 6** introduces a novel high frequency multi-axis capacitive gyroscope. This is an adaptation of the BAW gyroscope design for measuring the rotation rates around the *x* or *y* and *z* axes. The multi-axis disks were further optimized for minimal frequency separation in their both in-plane

and out-of plane modes and their measured results are also presented in this chapter. **CHAPTER 7** provides an overview of the contributions of this research and possible future directions in the area of the device performance optimization.

CHAPTER 2

REVIEW OF GYROSCOPES

2.1 HISTORY

Gyroscopes are a class of inertial sensors used to measure the rate or angle of rotation. The gyroscope effect was discovered in 1817 by Johann Bohnenberger but invented and named in 1852 by Léon Foucault for an experiment involving the rotation of the Earth [18]. Generally speaking, three major classes of gyroscopes have been developed and widely used: mechanical, optical and vibratory gyroscopes. In this section, a brief analysis of each gyroscope class is provided and their drawbacks for consumer electronics applications are discussed.

2.1.1 MECHANICAL GYROSCOPES

A gimbaled gyroscope is a mechanical device comprised of a spinning wheel mounted on two gimbals, allowing the rotation of an object along the three-axis. A high speed, rotating inertial disk is loosely coupled to the frame. When a rotation is applied to the frame, a torque (rotation) is created in the spinning disk due to conservation of angular momentum. The induced torque is monitored by a meter which counteracts the torque with springs or a similar restoring force. A three-axis gimbaled may allow a mounted object to remain in a horizontal plane regardless of the motion in support [19]. Figure 2-1 shows a schematic of a gimbaled gyroscope and the principle of operation to measure roll rotation [20, 21].

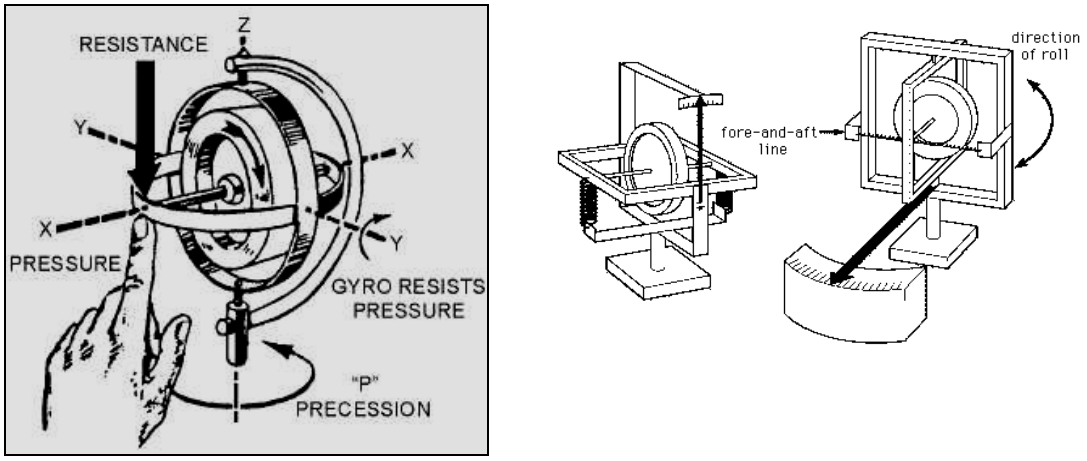

(a) (b)

Figure 2-1: (a) A gimbaled spinning wheel gyroscope, (b) illustration of detecting roll rotation in a gimbaled [20, 21].

It is worth nothing that a mechanical gyroscope measures angle of rotation, however optical and vibratory gyroscopes measure the angular velocity (rotation rate). The main disadvantage of the mechanical gyroscopes is that they require moving parts. This introduces friction and wear into the system, in turn inducing long-term performance drifts. To minimize these effects, high-precision bearings and special lubricants are required. This adds to the overall cost to the manufacture and maintenance of the device. Also, the existence of moving parts in gimbaled gyroscopes makes them too bulky and expensive for many low-cost emerging applications.

2.1.2 OPTICAL GYROSCOPES

Fiber optic gyroscopes (FOG) and ring laser gyroscopes (RLG) can be categorized as optical gyroscopes, in which the interference of light is used to detect mechanical rotation. In fiber optic gyroscopes (FOG), two light beams travel along the fiber in opposite directions. Due to the Sagnac effect [22] the beam traveling against the rotation experiences a slightly shorter path than the other beam. The phase-shift introduced

between the beams causes interference patterns in the combined beam, and its intensity behaves as a function of the applied rotation rate. Figure 2-2 illustrates the Sagnac effect in a Fiber optic gyroscope [22] and an example of FOG [23].

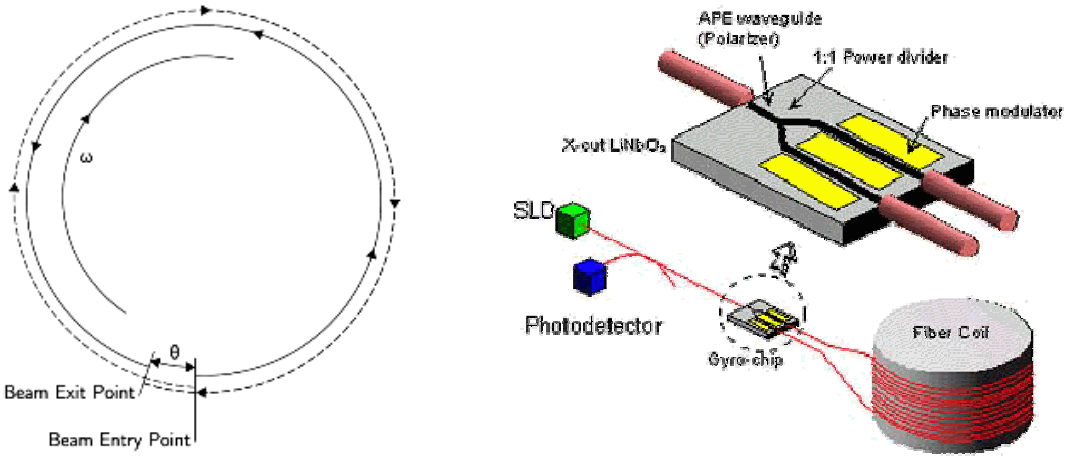

(a) (b)

Figure 2-2 : (a) Illustration of the Sagnac effect utilized in optical gyroscopes, (b) A schematic of IFOG [22, 23].

A Ring laser gyroscope (RLG) is composed of segments of transmission paths configured as either a square or a triangle and connected with mirrors. One of the mirrors is partially silvered, allowing light through to the detectors. A laser is launched into the transmission path in both directions, establishing a resonating standing wave over the length of the path. As the apparatus rotates, light in one branch travels a different distance than the other branch. This changes the phase and resonant frequency of one direction with respect to the light traveling in the other direction, creating a rotation-modulated interference pattern at the detector. The angular position is measured by counting the interference fringes. Figure 2-3 shows schematic diagram of a solid-state laser in a ring laser gyroscope [24] along with an example of ring laser gyroscope [25].

Unlike mechanical gyroscopes, optical gyroscopes contain no moving parts and require only a few seconds to start up. However, optical gyroscopes rely on the complicated assembly of several external components such as lasers, and power-intensive detection mechanisms, resulting in high assembly and maintenance cost. In addition, the accuracy of an optical gyroscope is largely dependent on the length of the light transmission path (larger is better), which is constrained by the size of the device. The optical gyroscopes generally are notorious for their high power consumption and low reliability.

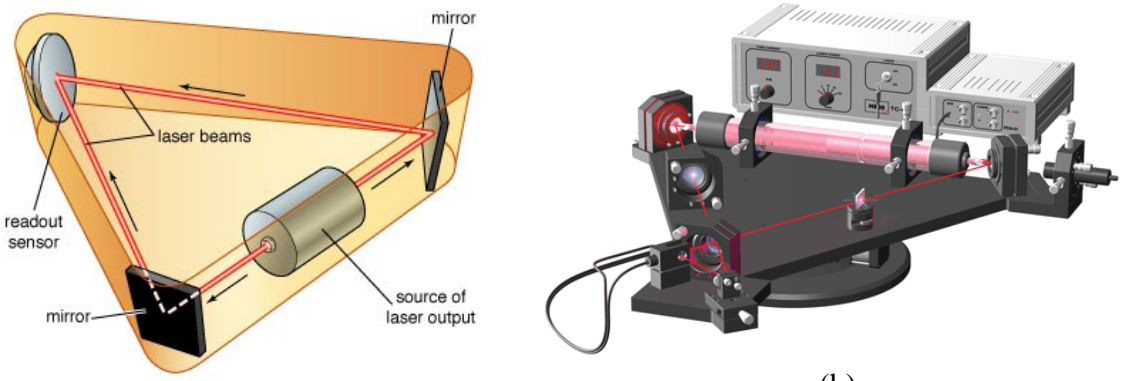

(a) (b)

Figure 2-3: (a) Schematic diagram of a RLG, (b) An example of RLG [24, 25].

2.1.3 VIBRATORY GYROSCOPES

The traditional gimbaled spinning wheel and optical gyroscopes are two well-known approaches to high precision in gyroscopes; however these devices are currently too expensive and bulky for many emerging low-cost applications. Another popular class of successful gyroscope designs is known as vibratory gyroscopes; these occupy the focus of this dissertation. Vibrating mechanical elements are used to sense the rotation rate by measuring Coriolis accelerations. This eliminates any need for moving parts, allowing a simple device structure. In addition, vibratory gyroscopes are excellent candidates for

miniaturization using micromachining techniques due to the absence of rotating parts (e.g. bearings) in their structure. Thereby, they can be readily miniaturized and batch fabricated to produce low-cost, small-size and low-power devices. Additionally, vibratory gyroscopes offer the possibility of sensing rotation about more than one axis, with smaller form factors and power consumption than other types of gyroscopes. Examples of vibratory gyroscopes are piezoelectric gyroscopes [26], hemispherical resonator gyroscopes [27], tuning fork gyroscope [28] and vibratory wheel gyroscopes [29], which are discussed in the following sections.

2.2 PRINCIPLE OF OPERATION

All vibratory gyroscopes use vibrating mechanical elements to sense the Coriolis acceleration arising from rotation in rotating reference frames. Coriolis acceleration results from the motion orthogonal to the angular velocity (Ω) of a rotating system. For a particle with linear velocity $\vec{v}$, this is expressed as $\vec{a}_{Corilios}$:

$$\vec{a}_{Corilios} = -2\vec{v} \times \vec{\Omega} \qquad (2\text{-}1)$$

From this acceleration, a fictitious force known as "Coriolis force" is derived. This force is exerted on a moving body in the local rotating frame. As (2-1) shows, this acts orthogonal to the body's velocity direction and is proportional to the applied rotation rate. This effect is named after Gaspard-Gustave Coriolis, a French scientist, who described it in 1835, though the mathematics appeared in the tidal equations of Laplace in 1778 [30]. Figure 2-4 shows the Coriolis force results from a linear motion orthogonal to an applied rotation.

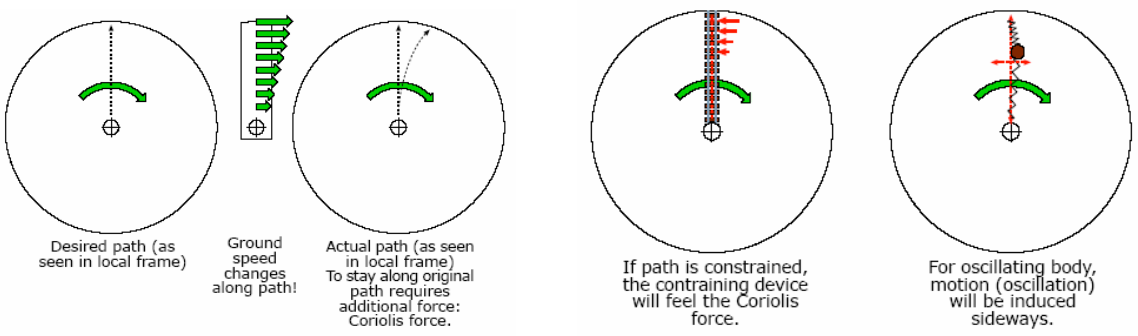

Figure 2-4: The illustration of a Coriolis force results from a linear motion orthogonal to the axis of rotation [30].

A typical vibratory rate gyroscope consists of a mass-spring system that has two or more orthogonal vibration modes, as shown in Figure 2-5. The mass is excited at the resonant frequency of a selected mode, the so-called drive mode, in the reference frame of the device. When the device and its reference frame reference experience rotation, a corresponding Coriolis force induces oscillation in any modes orthogonal to the drive mode. Sensors measure the latter motion directly, but the signal they provide is proportional to the rate of rotation.

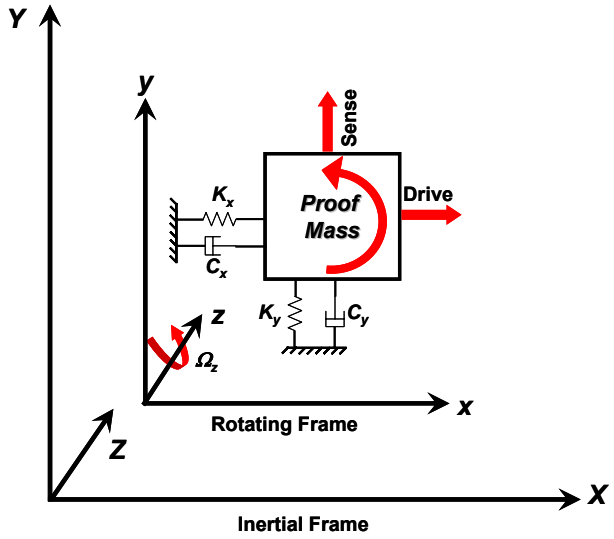

Figure 2-5: The illustration of a single proof-mass vibratory gyroscope.

The equation of motion for a mass-spring system moving in a non-inertial reference frame can be found using Lagrange dynamic method. In order to do that, the potential and kinetic energy as well as the generalized forces, such as damping forces, need to be derived for the system. Subsequently, the equation of motion (EOM) for a single-mass vibratory gyroscope in the local frame of reference can be expressed in the general form of [31]:

$$M\ddot{x} + C_x\dot{x} + K_x x - M\Omega_z{}^2 x - (\dot{\Omega}_z)y - 2M\Omega_z\dot{y} = F_{0drive}\sin(\omega_{drive}t) \quad (2\text{-}2)$$

$$M\ddot{y} + C_y\dot{y} + K_y y - M\Omega_z{}^2 y - (\dot{\Omega}_z)x - 2M\Omega_z\dot{x} = 0 \quad (2\text{-}3)$$

Where M, C and K are respectively the mass, damping coefficient and total stiffness; Ω_z, F_{0drive} and ω_{drive} are the applied rotation rate around z-axis, drive force, and the angular frequency of the drive signal, respectively.

The terms $-2M\Omega_z\dot{y}$ and $-2M\Omega_z\dot{x}$ are the rotation-induced Coriolis force components and constitute the dynamic coupling between the vibratory modes, which are utilized for angular rate measurements in a vibratory gyroscope.

The angular acceleration terms ($\dot{\Omega}_z$) in the EOM is usually ignored. This is because the ratio of angular acceleration to the Coriolis acceleration is inversely proportional to the natural frequency of the modes. Since the operating frequencies are in the range of kHz, the angular acceleration is insignificant in comparison with the Coriolis acceleration even when a large rotation rate is applied. Also, the Coriolis signal is modulated with a fixed drive frequency (ω_{drive}), permitting frequency-selective removal of the angular acceleration signal components.

At the end, a mechanism is needed to apply an excitation force such as $F_{drive} = F_{0drive}\sin(\omega_{drive}t)$ to maintain the drive mode oscillation. And a second mechanism must be implemented to measure excitation of the sense mode. A number of schemes, such as piezoelectric, capacitive electrostatic or electromagnetic actuation, have been used to implement the drive and sense mechanisms for Coriolis-based microgyroscopes. The subject matter of this dissertation refers mainly to the case of capacitive-based silicon vibratory microgyroscopes.

2.3 PERFORMANCE PARAMETERS

Several specifications are used to determine the performance of a vibratory gyroscope. These performance metrics are briefly discussed below.

2.3.1 RESOLUTION

Resolution is the minimum rotation rate that can be distinguished from the noise floor of the system, typically rationalized per square root of bandwidth of detection. This is expressed in units of (°/s/√Hz) or (°/hr/√Hz). The overall resolution of a micro-gyroscope, the total noise equivalent rotation (TNEΩ), is determined by two uncorrelated components:

- the mechanical (or Brownian) noise equivalent rotation (MNEΩ), originating in the micromachined mechanical structure, and
- the electronic noise equivalent rotation (ENEΩ), originating in the interface circuitry.

The minimum resolvable rotation rate is expressed as:

$$\Omega_{\min}\,(\text{Total}) = \sqrt{\Omega_{\min}\,(\text{Brownian})^{\,2} + \Omega_{\min}\,(\text{Electronic})^{2}} \tag{2-4}$$

Brownian motion of a structure, which is a result of molecular collisions with the surrounding medium, represents the mechanical noise component of the resonating mechanical element in a gyroscope [32]. By equating the displacement caused by Brownian motion to the displacement induced by Coriolis acceleration, one can derive the mechanical resolution of a vibratory micro-gyroscope for matched-mode operation.

$$\Omega_{\min}(Brownian) \propto \frac{1}{q_{drive}}\sqrt{\frac{4k_B T_0}{\omega_0 M Q_{EFF}}}\sqrt{BW} \tag{2-5}$$

Where q_{drive} is the drive amplitude; ω_0, M, and Q_{EFF} are the natural angular frequency, the effective mass and effective quality factor at the sense mode, respectively; k_B is the Boltzmann constant (1.38×10^{-23} J/K), BW is the measurement bandwidth (Hz) and T_0 is the absolute temperature.

The electronic noise floor is dependent upon the noise of the interface circuitry. Assuming the input-referred noise (I_{noise}) has a white spectrum near the resonant frequency; electronic noise of the interface circuitry for matched-mode operation is expressed in [33] as:

$$\Omega_{\min}(electronic) \propto \frac{d_0}{V_p C_{s0} q_{drive} Q_{EFF} A_g} I_{noise}\sqrt{BW} \tag{2-6}$$

where d_0, C_{s0}, A_g and V_p are respectively the capacitive gap, sense capacitance, angular gain and polarization voltage. It is evident that drive amplitude, device mass, sense gap, angular gain and effective quality factor, all play key roles in determining the overall noise floor.

The noise floor of a gyroscope is often expressed in terms of angle random walk (*ARW*). This is a measure of the angular error buildup with time that is due to white noise in the angular rate signal. This error is typically expressed in degrees per square root of hour (°/√hr). The relation between the noise floor per unit bandwidth and the *ARW* is given by:

$$Noise\ floor\left(\circ / hr / \sqrt{Hz}\right) = ARW\left(\circ / \sqrt{hr}\right) \times 60 \tag{2-7}$$

It is worth noting that the resolution of current low frequency gyroscopes is limited by the Brownian noise, and not by the electronic noise.

2.3.2 SCALE FACTOR

The scale factor of a micro-gyroscope is the ratio of a change in the output signal to a change in the input applied rotation. Scale factor is generally evaluated as the slope of the straight line that can be fitted by the method of least squares to input-output data [34], and is generally expressed as (2-8) in units of Volt/°/sec. In capacitive gyroscopes, sense mode vibration, presumably Coriolis-induced, is detected through changes in the sense capacitance. Accordingly, the expected scale factor is given as follows,

$$Scale\ factor = \frac{2V_p C_s Q_{EFF} q_{drive}}{(C_s + C_{parasitic}) d_0 \omega_0} \tag{2-8}$$

where V_p, C_s, $C_{parasitic}$, and d_0 are respectively the polarization voltage, the capacitance at the sense, the parasitic capacitance and the capacitive gap at the sense.

In a vibratory gyroscope, sensitivity (sense mode deflection) is proportional to the effective quality factor (Q_{EFF}) and the drive amplitude at the driven axis (q_{drive}), but is inversely proportional to the operating frequency (ω_0). Q_{EFF} in turn is significantly dependent on the separation between the drive and sense resonant mode frequencies. If

matched-mode operation is attained, the sensitivity is significantly enhanced due to the Q_{EFF} increase. For a given resonant frequency, having a higher gap-aspect ratio at the sense capacitance gives larger changes in the sense capacitance, thereby generating a larger electrical signal for a given input rotation rate. As a result, high effective quality factors (Q_{EFF}), large drive amplitudes, low parasitics, and high gap-aspect ratio at the sense electrode all contribute to a high gyroscope scale factor.

2.3.3 ZERO RATE OUTPUT (ZRO) AND DRIFT

Zero rate output (ZRO) is the measure of an output signal from a gyroscope in the absence of an input rotation rate. The drift of the ZRO over time, expressed in (°/hr), is known as bias drift, and is an important performance metric that ultimately determines the long-term stability of a gyroscope. The zero rate output can originate from geometrical irregularities in the vibrating structure or the sense and drive electrodes as well as from electrical coupling between these electrodes. By electrically and mechanically decoupling the sense and drive modes, and by minimizing the fabrication process errors, ZRO can be significantly reduced [34, 35].

Exploiting the relationship between bias drift and noise floor, a measure of the power spectral density (PSD) was used to measure bias drift. Generally, the zero rate output (ZRO) of the device is sampled for a period of time. An Allan variance analysis is performed on long-term ZRO recordings to characterize the long-term stability of the matched-mode device [33, 36]. The minima of the Allan variance plot represent the bias stability. Large sensitivity, high quality factor (Q) and matched-mode operations are key parameters in improving the bias drift.

2.3.4 BANDWIDTH AND DYNAMIC RANGE

The bandwidth of the microgyroscope determines the response time of the system. Response or settling time is the time required for the output to settle to within a certain range of the expected value for an input step function. In a vibratory gyroscope, the sensor bandwidth (BW) is related to the resonant frequency (ω_0) and quality factor (Q) by:

$$BW = \frac{\omega_0}{2Q} \tag{2-9}$$

High bandwidth is always desirable for a gyroscope. Some applications such as automotive and consumer electronic require very fast response time (at least $\tau < 0.03$ Sec, BW=33Hz) and other applications like inertial navigation can tolerate longer response times. To date, the most advanced gyroscopes suffer from very small bandwidth, necessitating complex circuits to compensate for their long response time. This introduces not only additional sources of errors but also additional cost, driving a strong preference for achieving large bandwidth from the mechanical structure (*i.e.* via ω_0 and Q).

Dynamic range refers to the range of input values over which the output is detectable. It is typically computed as the ratio between the maximum input rotation rate (full scale rate) that the sensor can tolerate and the system noise floor.

In general, gyroscopes can be classified into three different categories based on their performance: inertial-grade, tactical-grade, and rate-grade devices. Table 2-1 summarizes the required performance specification for each aforementioned class of gyroscopes.

Table 2-1: Performance requirements for different classes of gyroscopes.

Device Parameter	Rate Grade	Tactical Grade	Inertial Grade
Angle random walk (deg/√hr)	> 0.5	0.5 – 0.005	< 0.001
Bias drift (deg/hr)	10 – 1000	0.1 – 10	< 0.01
Scale factor accuracy (%)	0.1 – 1	0.01 – 0.1	< 0.001
Full scale range (deg/sec)	50 – 1000	> 500	> 400
Maximum shock in 1msec (G)	10^3	$10^3 – 10^4$	10^3
Frequency bandwidth (Hz)	> 70	~ 100	~ 100

2.4 CLASSIFICATIONS OF VIBRATORY GYROSCOPES

Vibratory gyroscopes are based on a transfer of energy between two vibration modes of a structure, and can operate in either matched-mode or split-mode condition. Under a matched-mode condition, the sense mode is designed to have the same (or nearly the same) resonant frequency as the drive mode. Hence, the rotation-induced Coriolis signal is amplified by the mechanical quality factor (Q) of the sense mode. In a split-mode condition, the drive and sense modes have separate resonant frequencies, and the sense mode is a controlled mode for measuring the Coriolis acceleration [38, 39]. Due to Q amplification, gyroscopes operated under matched-mode configuration offer higher sensitivity and better resolution. Matched-mode devices are classified into two types depending upon the nature of their operating modes. Type I devices rely on non-degenerative vibration modes. Tuning fork [8, 40] and frame [41] gyroscopes are examples of type I gyroscopes. In contrast, degenerative vibration modes are employed by type II gyroscopes, whose subclasses comprise shell, cylindrical, ring /star and disk gyroscopes [7, 9, 42].

2.5 REVIEW OF MICROMACHINED SILICON GYROSCOPES

Micromachining is a recently developed method to simultaneously scale down the size and cost of devices, often attracting high volume applications. The first batch-fabricated silicon micromachined vibratory gyroscope was demonstrated by the Charles Stark Draper Laboratory in 1991. This silicon bulk mechanical device was a double-gimbal vibratory gyroscope supported by torsional flexures [43]. In this design, an outer gimbal was electrostatically excited at constant amplitude using drive electrodes. In the presence of rotation normal to the plane of the device, this oscillatory motion was transferred to the inner gimbal along the stiff axis of the inner flexures.

Two years later, in 1993, the Charles Stark Draper Laboratory reported a silicon-on-glass tuning fork gyroscope [44] fabricated through the dissolved wafer process [45]. This gyroscope was electrostatically vibrated in its plane using a comb drive actuators. The applied rotation signal normal to the drive mode would then excite the out-of-plane rocking mode of the structure which was capacitively monitored.

Since 1993, silicon micromachined vibratory gyroscopes have been broadly developed and reported, as discussed later in this section. A diverse set of micromachining fabrication technology such as surface-micromachining, bulk-micromachining, and mixed-mode micromachining has been employed to implement several architectures such as frame, tuning fork and shell-type structures.

Surface micromachined devices dominated initial MEMS gyroscope research primarily because of their potential for simple integration with interface electronics. However, they were found to suffer from thin-film residual stress, squeeze-film damping and high thermomechanical noise associated with their low mass [46]. The need to address the

surface micromachined gyroscopes' issues has directly led to research in bulk-micromachined gyroscopes. Bulk-micromachined devices can provide large capacitance or piezoresistive readouts due to their large electrode areas. The issues in bulk micromachining such as high aspect ratio trench etching, wafer bonding, and vacuum packaging have been addressed and resolved in recent years with the advancement in micromachining tools and technology. Another major development in bulk micromachined gyroscopes has been the adoption of silicon on insulator (SOI) wafer-based fabrication. The thick, single crystalline silicon device layer of SOI wafers provides large mass and sensing area, dually improving gyroscopes' performance. Next in this section, a brief history of several main gyroscope architectures including frame, tuning fork, and shell types, is presented. Following that, existing multiple-axis approaches and commercialized gyroscopes are presented.

2.5.1 MICROMACHINED FRAME DESIGN

Micromachined vibratory gyroscopes using frame structures offer the possibility of measuring the in-plane rotation rate (*x*-*y* axis) as well as out-of-plane rotation rate (*z*-axis). In 1996, Clark and Howe (University of California at Berkeley) reported a frame structure surface micromachined *z*-axis gyroscopes [47]. Making use of Analog Devices BiMEMS process [48] they electrostatically tuned the sense mode and nulled the quadrature errors. In 2000, Mochida (Murata) and Song (Samsung) both utilized bulk micromachining to implement single crystal silicon frame structures capable of detect *x*-axis rotation rates [49, 50]. In 2002, Geiger (HSG-IMIT) explored *x*-axis frame gyroscopes utilizing surface micromachined polysilicon [51]. Examples of the frame structure gyroscopes are shown in Figure 2-6.

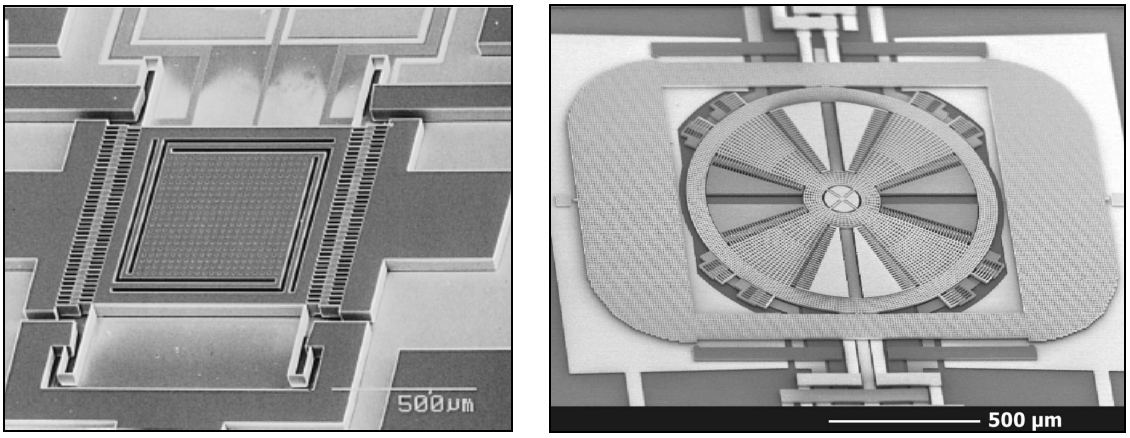

(a) (b)

Figure 2-6: Examples of frame gyroscopes: (a) Bulk-micromachined gyro with independent beams for the drive and sense modes [49], (b) Surface-micromachined gyro by HSG-IMIT with decoupled angular velocity detector [51].

2.5.2 MICROMACHINED TUNING FORK AND COUPLED-MASS DESIGNS

In terms of performance (sensitivity and resolution), the field of micromachined vibratory gyroscopes is led by devices based on tuning fork and coupled mass theory, due to their large mass and very large drive amplitude. In 1997, Lutz (R. Bosch) employed a dual-mass approach to measure *z*-axis rotation rate [52], using a fabrication process based on surface micromachining of 12µm thick polysilicon. In 1998, Kourepenis (Draper Labs) developed and reported a tuning fork gyroscopes (TFG) consisting of a silicon structure suspended above a glass substrate supporting metallized electrodes [53]. In 2002, BAE (Jet Propulsion Laboratory, JPL) utilized the coupled-mass approach along with a silicon base-plate and bulk micro-metal post [54]. A SEM view of this device is shown in Figure 2-7(a). They achieved a resolution of 6°/hr/√Hz, which was the highest reported resolution at that date. In 2004, Acer and Shkel proposed a novel 4-DOF micromachined gyroscope system utilizing dynamical amplification to achieve large oscillation amplitudes without resonance. They mechanically decoupled the drive direction

oscillations from the sense direction oscillations [55]. Figure 2-7(b) shows a SEM image of this 4-DOF microgyroscope.

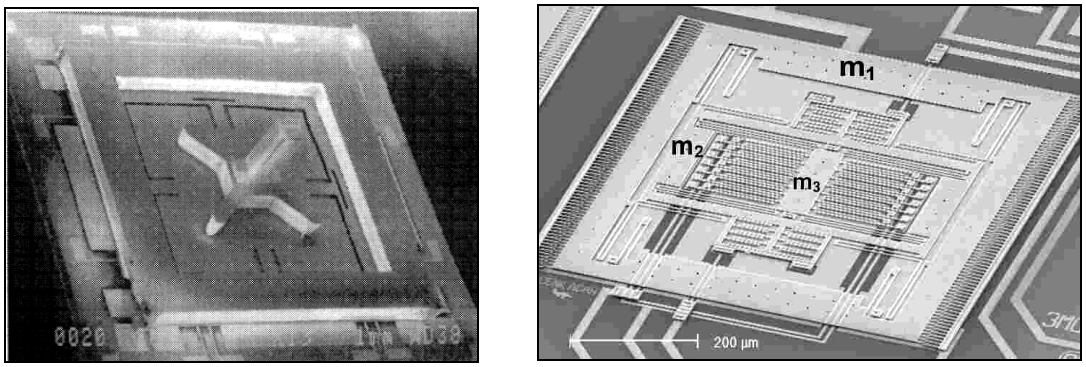

(a) (b)

Figure 2-7: Examples of coupled-mass gyroscopes: (a) JPL's microgyroscope [54], (b) 4-DOF microgyroscope with improved oscillation amplitude and decoupled drive and sense oscillations [55].

Later, the most advanced bulk micromachined gyroscope was the matched mode *z*-axis tuning fork design reported by the IMEMS group at Georgia Tech in 2006 [8]. The matched-mode tuning fork gyroscope (M^2-TFG) is fabricated on 50-µm thick SOI substrate, and exhibits an overall rate sensitivity of 24.2mV/º/sec and a measured bias instability of 0.96 º/hr. In 2007, R. Neul (Bosch) also used coupled-mass theory and surface micromachined thick epi-poly to enable measuring *z*-axis rotation rate [56]. They reported 0.12°/hr/√Hz resolution, the highest recorded resolution. SEM views of bulk-micromachined matched-mode tuning fork gyroscope [8] and surface-micromachimed thick epi-poly gyroscope [56] are shown in Figure 2-8.

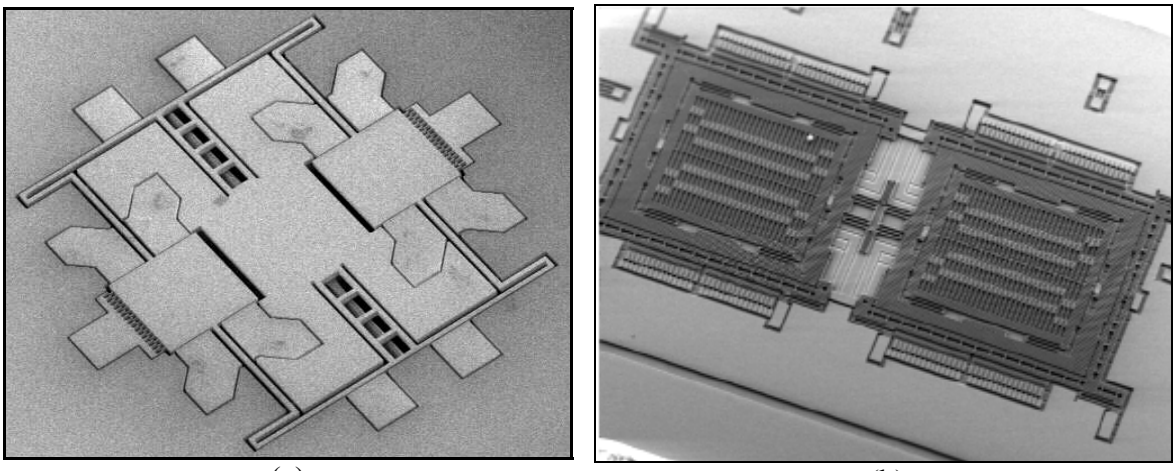

(a) (b)

Figure 2-8: Examples of tuning fork gyroscopes: (a) Bulk-micromachined matched-mode tuning fork gyroscope [8], (b) Surface-micromachined thick epi-poly gyroscope [56].

2.5.3 MICROMACHINED SHELL-TYPE DESIGN

Current shell-type micromachined vibrating gyroscopes have mostly used ring structures. The planar nature of rings makes them more compatible with micromachining techniques and materials. In 1990, Burdess and Kanani developed a solid state piezoelectric cylinder gyroscope [57]. The cylinder is set into mechanical vibration at its first inextensible mode through piezoelectric action. Voltages applied to electrodes on the surface of the cylinder are used to generate the necessary excitation. When a rate of turn is applied about an axis parallel to the central axis of the cylinder the nodes of this mode move by an amount proportional to the applied rate. This movement is detected by sensing electrodes on the surface of the cylinder. In 1994, Putty and Najafi (University of Michigan) explored the micromachined vibrating ring gyroscope that uses an electroformed nickel ring as gyroscope elements to measure the rotation rate around *z*-axis. Electrostatic driving and sensing was employed in this design, and the fine-tuning of vibration modes was made possible through a plurality of electrodes [42]. In 1997, Hopkins (British Aerospace

Systems and Equipment, BASE) developed a silicon vibrating structure gyroscope (Si-VSG) using a ring structure. This was driven and sensed electromagnetically to measure *z*-axis rotation rate [58]. In 1998, Burdess and Harris (University of Newcastle, UK) applied electromagnetic driving and sensing similar to Hopkins's method to surface micromachined ring gyroscopes [59]. In 1999, McNie's group (Defence Evaluation and Research Agency, UK) developed high aspect ratio ring gyroscopes fabricated in (100) SOI substrates. DRIE of a SOI substrate was used to form the ring as well as the drive and sense electrodes [60]. Later in the same year, Zarabadi (General Motors Research Labs) investigated a device that combined comb drive actuation with a ring as the resonant element. In this device, pairs of comb drives are arranged cyclically around the ring to provide the electrostatic actuation and sensing of the flexural modes of vibration [61]. In 2000, Ayazi and Najafi (University of Michigan) developed LPCVD polysilicon vibrating ring gyroscopes with electrostatic driving and sensing [62]. Examples of the shell-type gyroscopes are shown in Figure 2-9.

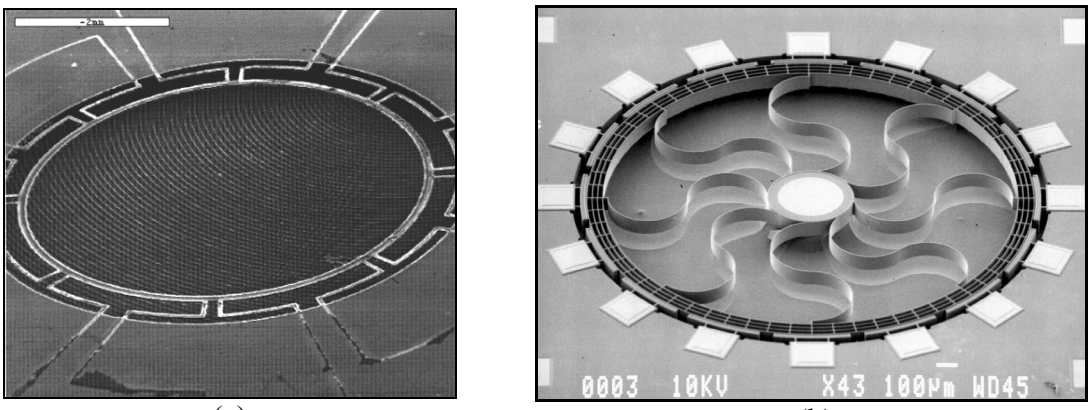

(a) (b)

Figure 2-9: Examples of shell-type gyroscopes: (a) Ring micro-gyro employing electromagnetic driving and sensing [58], (b) LPCVD polysilicon vibrating ring gyroscope with electrostatic driving and sensing employing bulk micromachining [62].

2.6 MULTI-AXIS MICROMACHINED GYROSCOPES

The vast majority of the macromachined and micromachined vibratory rate gyroscopes reported to date have been single axis devices. Dual axis operation has been investigated for coupled-mass and frame designs. In 1997, Juneau and Pisano (U.C. Berkeley) reported a dual axis gyroscope comprising a suspended polysilicon disk structure supported by a set of four compliant beams above a substrate, capable of measuring in-plane rotation (*x* and *y* axes). The primary rotational mode, about the polar axis of the disk, is driven using the comb drives. Sensing of the secondary modes, rotational modes excited in the presence of rotation about either in-plane axis, is achieved capacitively [63]. A very similar device by An and Song (Microsyst. Lab., Samsung Adv. Inst. of Technol., Yongin, South Korea) is reported in 1998, using a polysilicon disk, electrostatic comb drives, and capacitive sensing. The fabrication process was based on surface micromachining of 2μm thick polysilicon [64]. In 2004, Xie and Fedder (Carnegie Mellon University) developed and reported *x-z* axis frame gyroscopes based on DRIE postprocessing of CMOS wafers [65]. Besides dual axis gyroscopes, in 2001, Gallacher and Burdess (University of Newcastle UK) developed the principles of multi-axis vibrating ring gyroscopes and, in 2006, reported the frequency results of these devices [66, 67]. They introduce employing Coriolis coupling between in-plane and out-of plane flexural modes in a ring. Succeeding their introduction of multi-axis gyroscopes, there is a wide field open for the practical examination of these devices. Examples of multi-axis micromachined gyroscopes are shown in Figure 2-10.

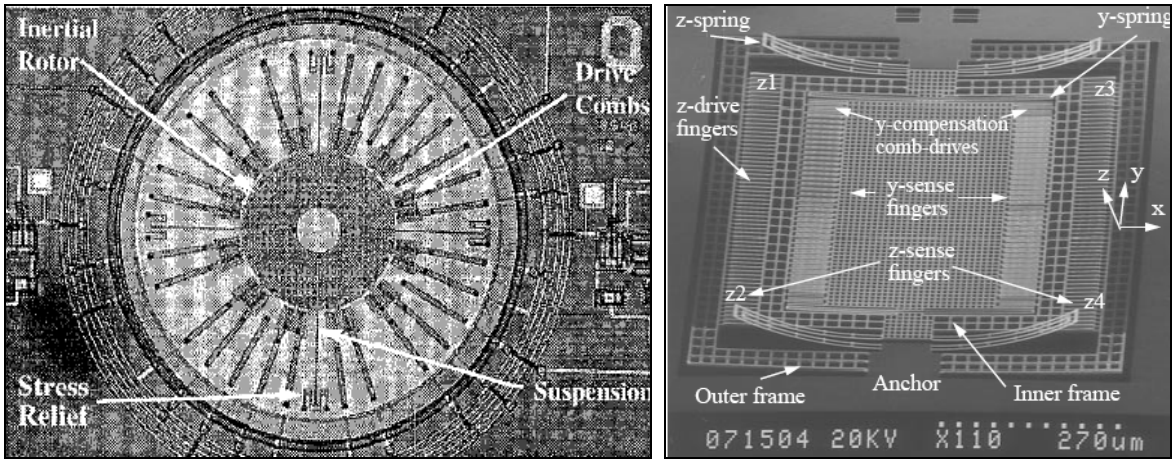

(a) (b)

Figure 2-10: Examples of dual-axis gyroscopes: (a) A suspended polysilicon disk structure measuring the rotation rate around *x* and *y* axis. [63], (b) A post CMOS processing *x*-*z* axis frame gyroscopes [65].

2.7 COMMERCIAL MICROMACHINED GYROSCOPES

The rise of several successful commercial MEMS gyroscopes was led by the automotive industry's rapid exploitation of such practical, miniature devices. The first of these was an integrated *z*-axis gyroscope announced in 2002 by Analog Devices Inc. (ADI), offering a very high resolution of 0.05 deg/sec/√Hz [16]. Later, Robert Bosch announced a *z*-axis angular rate sensor with analog output (SMG061) with 1.5 °/sec/√Hz resolution and >25Hz frequency bandwidth [68]. In 2006, Silicon Sensing introduced a high resolution gyroscope product (SiRRS01) to the market, with bias instability of 3 °/hr [69]. The SiRRS01 evolved from the vibrating structure gyroscope developed by BAE Systems, which had been in service since 1990. Afterward, Northrop Grumman Corporation introduced a MAG-16 MEMS gyroscope to measure the *z*-axis rotation rate as a low cost solution for a wide range of military and commercial applications. It

claimed a bias instability of 10 °/hr [70]. Later on, in 2007, InvenSense Inc. offered the first commercialized dual-axis integrated gyroscope (IDG-300) that supports the high volume, low price and small size requirements of consumer products [71]. The IDG-300 gyroscope uses two sensor elements, each with vibrating dual-mass bulk-machined silicon configurations, that together sense rotation about the *x* and *y* axes (in-plane sensing). These integrated dual-axis micro-gyroscopes offer vibration rejection and high cross-axis isolation. A summary list of commercialized gyroscopes is presented in Table 2-2.

Table 2-2: A Summary of commercial MEMS gyroscopes.

Incorporate.	**ADI**	**Bosch**	**Silicon Sensing**	**Northrop Grumman**	**InvenSense**
Spec. / Prod.	ADXRS614 *z*-axis	SMG061 *z*-axis	SiPRS01 *z*-axis	MAG-16MEMS *z*-axis	IDG-300 *x*/*y*-axis
Range (°/sec)	50	240	110	150	50
Sensitivity (mV/°/sec)	25	7	18.18	36	4
BW (Hz)	2000	30	50	350	140
Noise density (°/sec/√Hz)	0.04	1.5	0.35	0.03	0.014
Nonlinearity (% FS)	0.1	0.5	1	<1	<1
Size (mm^2)	6.85×6.85×3.8	NA	31.8×31.8×17.3	57.87×57.87×15	6×6×1.5

As shown in Table 2-2, most of available commercialized gyroscopes measure single-axis rotation rate. However, InvenSense offers MEMS gyroscopes that measure the rotation rate around *x*-axis and *y*-axis, with the smallest size and highest resolution of 0.014 °/sec/√Hz. The highest sensitivity belongs to Northrop Grumman's and ADI's products with a typical resolution of ~2 °/√hr. The ADI products offer the highest bandwidth. The commercialized gyroscopes from Silicon Sensing and Northrop

Grumman are too large to be applicable in most of consumer electronics. As a result, InvenSense and ADI offer compact gyroscopes, clearly targeting automotive and consumer electronic applications. To date, there is no three-axis gyroscope available in the market that simultaneously offers small form factor, low price, and high performance. This would be very attractive for incorporation into consumer electronics, particularly in more tactile-centric applications such as handheld devices and gaming.

CHAPTER 3

BAW GYROSCOPE DESIGN

3.1 OVERVIEW

This chapter focuses on the design and modeling of capacitive silicon disk gyroscopes operating in their elliptic degenerative modes. Capacitive BAW disk gyroscopes, operating in their MHz-frequency bulk acoustic modes, are designed to operate in their primary and secondary elliptic degenerative modes in (111) and (100) single crystal silicon, respectively. Finite element analysis is employed to model the resonating disks to study the effect of perforations on the frequency separation between the selected degenerative modes. A comprehensive study of degenerative elliptic modes is performed in which the normal modal model is derived using the Lagrange method. Based on this modal analysis, the angular gain is estimated for both primary and secondary elliptic modes. In addition, an electrostatic tuning method is developed to match the frequencies of the degenerative modes. Sensitivity and resolution for these gyroscopes are derived and analyzed, and the key limitations are discussed. Finally, thermoelastic damping is modeled for these devices. Theoretical values for Q_{TED} as well as the effect of perforations in the disk on Q_{TED} are further studied.

3.2 PRINCIPLE OF OPERATION

A schematic view of a Coriolis-based silicon BAW disk gyroscope [72] is shown in Figure 3-1. The BAW gyroscope consists of a center-supported silicon disk with

capacitive drive, sense and control electrodes. The locations of the electrodes are chosen depending on the mode of operation and the crystal orientation of the silicon. Electrodes are located at the anti-nodes of the resonant modes. This provides maximal transduction and also facilitates matched-mode operation.

The capacitive BAW disk gyroscope is supported by a small island of buried oxide layer (BOX), shown in Figure 3-1 as the center support. The symmetry of the structure guarantees that the support is self-aligned to the disk center during the BOX etch step. Boron-doped polysilicon traces attached to the center of the disk, to which they are also self-aligned, provide a DC bias voltage to the disk. In addition, to release these devices in SOI and facilitate the BOX etch, release holes are added to the disk (though not shown in Figure 3-1).

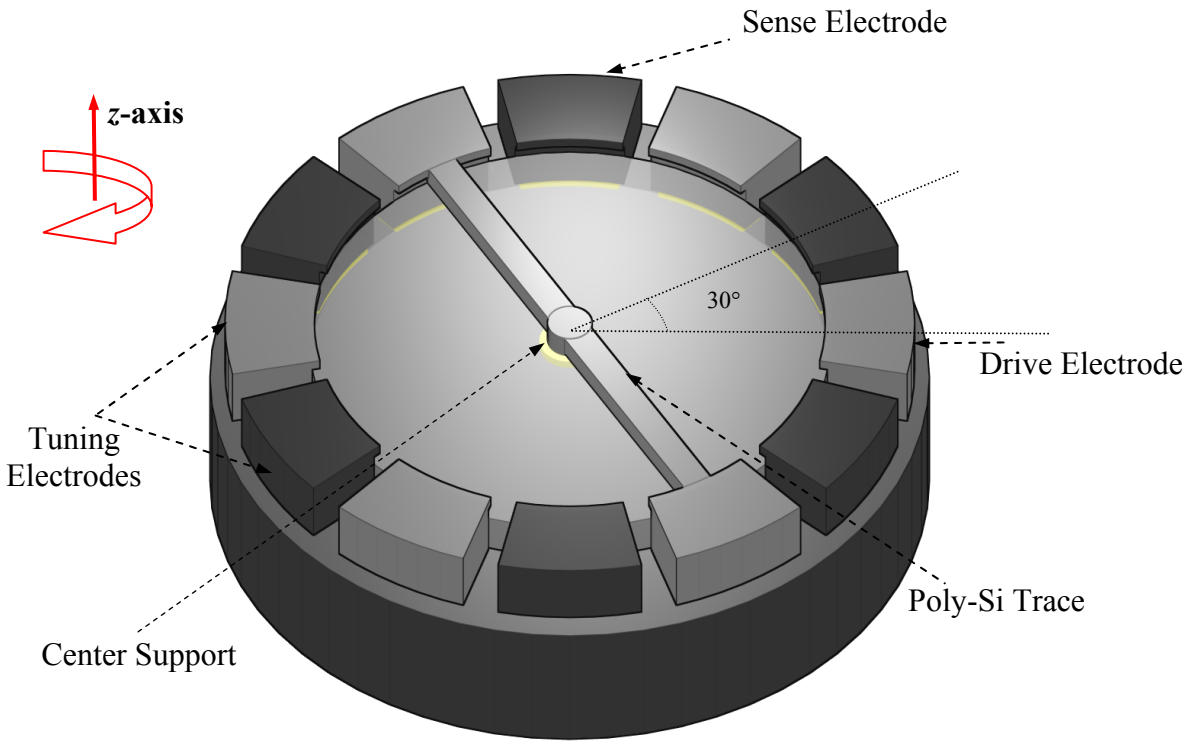

Figure 3-1: Schematic diagram of the capacitive BAW disk gyroscope in (100) silicon.

In order to excite BAW modes, large electrostatic forces are required, which in turn necessitate large capacitive coupling. High gap-aspect ratio along with very small capacitive gaps provide large capacitive coupling. These needs are met by implementing the devices on thick SOI substrates (in the range of 30 to 60μm) with sub-micron capacitive gaps (of typically 200nm).

To actuate the capacitive BAW disk gyroscope, an AC signal is applied to the drive electrode at the selected resonant frequency, along with the application of DC bias to the disk itself. While the disk is driven at its first degenerative elliptic mode, the gyroscope is rotated. Coriolis acceleration transfers energy between the two degenerative elliptic modes. As energy builds up in the second mode and this mode vibrates at the sense electrode, output current is generated. A custom-built interface circuit amplifies, demodulates and filters the sense current to yield rotation-induced Coriolis signal [74].

The principal features of the design are the axisymmetry of the disk along with the cyclic-symmetric arrangement of the release holes. These features allow important modes of vibration to exist in degenerate pairs [60]. To facilitate the mode matching process and consequently improve the performance, two degenerative modes with the same resonance frequency are used as the drive and sense modes [42]. However, perforations in the disk as well as fabrication errors inevitably introduce an appreciable amount of frequency separation. One or more electrodes, designated as “tuning electrodes,” can be used to electrostatically tune the two modes and reduce the frequency split between them. Quadrature errors can also be cancelled with the application of proper DC voltages to other electrodes.

In this dissertation, capacitive BAW disk gyroscopes are designed to operate in their degenerative elliptic modes in the frequency range of 2-10MHz in (100) and (111) single crystal silicon substrates. Selection of these modes is discussed in the following.

3.3 DESIGN OF (100) SCS GYROSCOPES

First, (100) SCS substrates are investigated because they are widely available and CMOS compatible. In (100) single crystal silicon, an anisotropic material, the primary elliptic vibration mode is accompanied by its degenerative mode at a 45° offset. ANSYS simulation results for an 800μm diameter (100) SCS solid disk indicate a frequency split of ~1MHz between two primary degenerative modes, as shown in Figure 3-2 (a). This makes them unsuitable for gyroscope applications. Figure 3-2 (b) shows ANSYS simulation results for secondary elliptic modes of the same device in (100) silicon. The secondary elliptic modes of a (100) silicon disk, which are 30º offset, have nearly identical frequencies ($\Delta f \leq 100$Hz). This implies that for (100) SCS, secondary elliptic modes should be employed to enable matched-mode operation.

Implementation of a solid disk requires a backside etch step, presenting the need for both topside and backside packaging. To eliminate the latter, perforations were added to the disk, enabling its release from the front side of SOI wafer. However, adding perforations to the disk introduces frequency shift between the modes. Finite element analysis was used to model the introduced frequency split as well as to guide the optimization of the release holes accordingly.

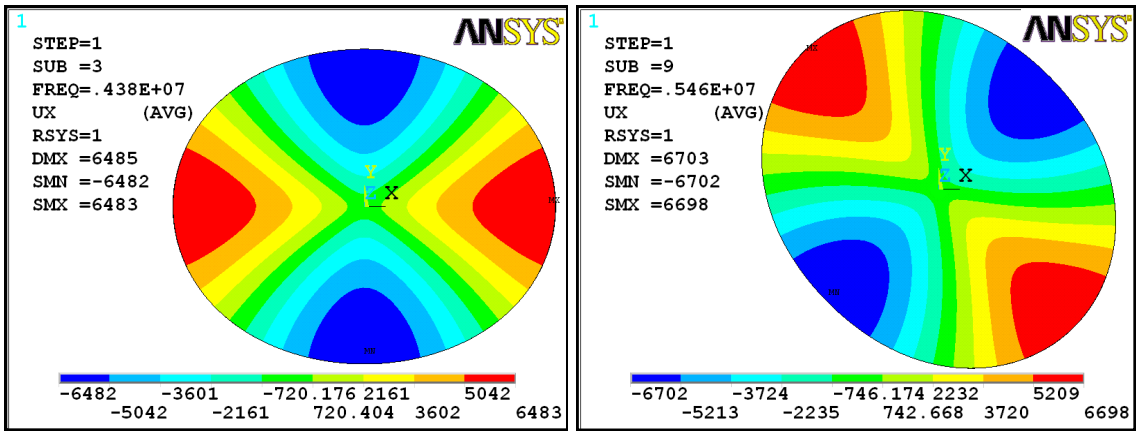

(a)

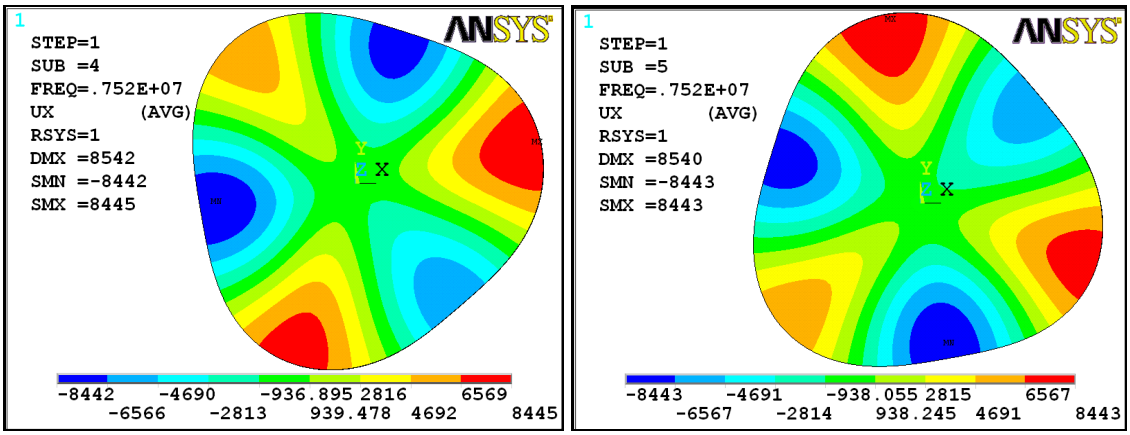

(b)

Figure 3-2: ANSYS simulation results of: (a) primary elliptic modes with Δf=1.08MHz; (b) secondary elliptic modes with Δf=70Hz in an 800μm diameter solid disk gyroscope in (100) silicon.

In order to minimize the effect of perforations on frequency split, some basic design rules were investigated and are discussed in the following. First, the orientations of the perforations need to be compatible with the anti-nodes and nodes of the vibration patterns. For example, to operate the disk in the secondary elliptic modes of (100) SCS, the perforations should be located at every 30° (or a fraction of 30°), to have the equal effects on both degenerative modes, resulting in minimizing the frequency split between two modes. Second, perforations tend to distort the mode shapes. This effect can be mitigated by choosing the shape, size, and configuration of the perforations appropriately.

A variety of configurations such as radial grooves, tangential grooves and holes with different sizes were modeled. According to ANSYS simulations, holes are preferable over grooves with respect to lessening mode shape distortion and frequency separation. Further optimizations addressed the holes' distributions and sizes. To do this, two major categories of equally-spaced rings of release holes were developed. The first category includes non-uniform sized holes along the radial direction of the disk. This approach placed the holes exactly at every 30° and 15°, coincident with the mode shapes' nodal lines. The second category is comprised of uniform small sized holes, located mostly at the fraction of 30° offset. Both structure types are symmetric about the *x* and *y* axis.

A variety of uniform hole sizes were designed and simulated in ANSYS to evaluate the frequency split between the modes. The results are shown in Figure 3-3.

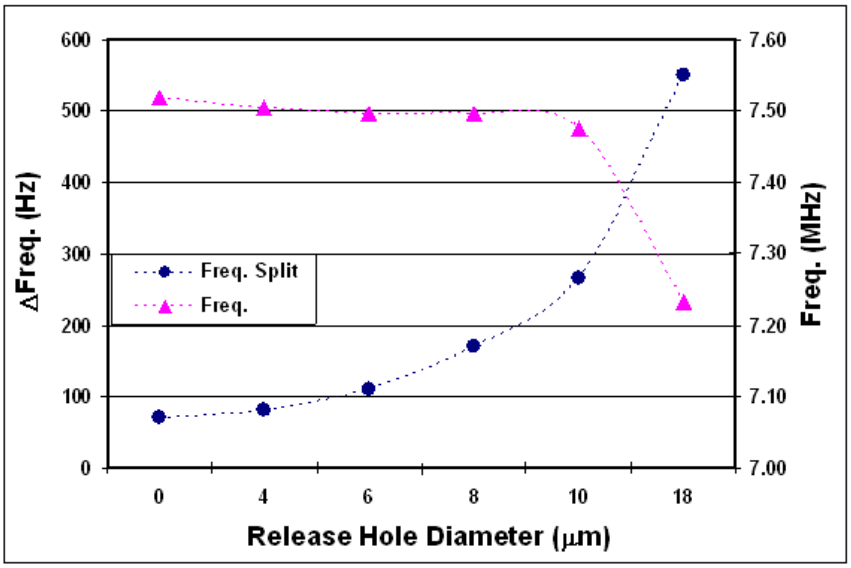

Figure 3-3: ANSYS simulation results of secondary elliptic modes in 800μm diameter disk gyroscopes in (100) silicon, showing the effect of release hole sizes on the frequency splits between two modes and the operating frequencies.

As expected, the disks with uniform small release holes exhibit very small frequency split (Δf<150Hz). This is because the frequency behavior of a disk with uniform small holes

closely mirrors that of the solid disk. ANSYS simulation results demonstrate frequency splits of 700Hz and 110Hz, respectively, for large non-uniformed holes and for 6μm diameter uniform holes, shown in Figure 3-4.

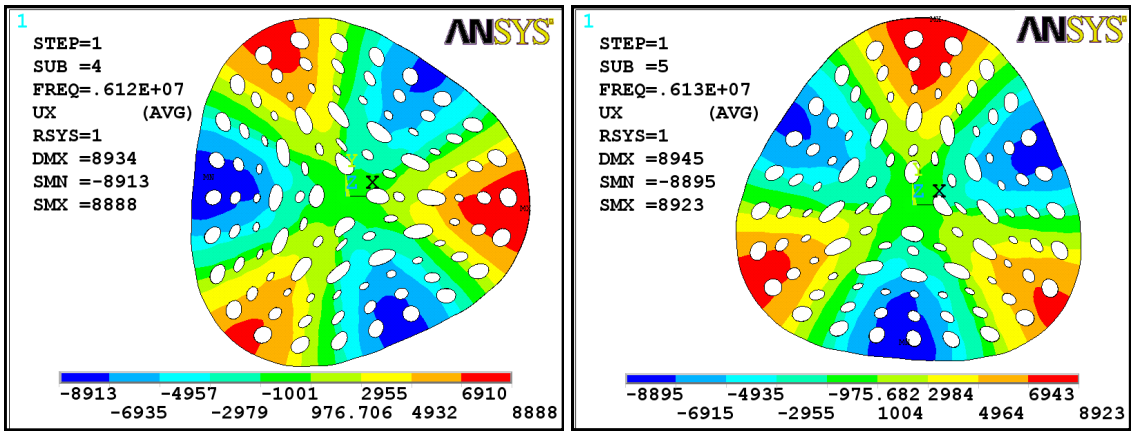

(a)

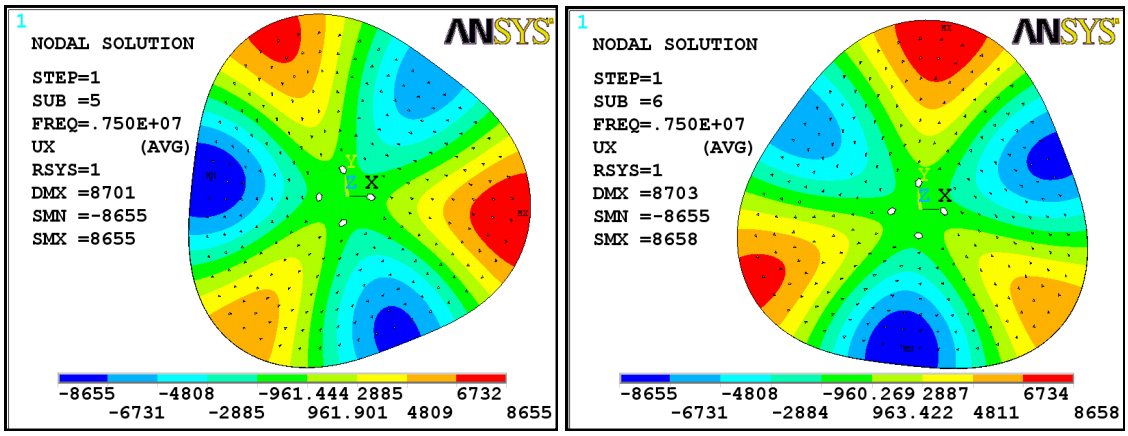

(b)

Figure 3-4: ANSYS simulation results of secondary elliptic modes in 800μm diameter disk gyroscopes including: (a) large non-uniform sized holes with Δf=700Hz; (b) 6μm diameter uniform sized holes with Δf=110Hz.

It is worth noting that the distance between the holes at the center of the disk needs to be large enough to ensure that the buried oxide center support survives the release etch. The center post diameter is designed to be at most one twentieth of the disk diameter, to minimize the losses through support [74-75] and to enhance the Q of the device. In all

ANSYS models, 50,000 elements were used to minimize the simulation errors in frequency split values.

In accordance with the' modes shapes in (100) SCS substrates, capacitive electrodes should be placed every 30º circumferentially around the disk to maximize the sense and drive transduction.

3.4 DESIGN OF (111) SCS GYROSCOPES

If an isotropic material (such as (111) SCS or polysilicon [76-77]) is used, the two primary elliptic degenerative modes, spatially 45º apart, have identical resonance frequencies (Δf=70Hz), Figure 3-5. This implies that BAW gyroscopes implemented in (111) SCS substrates should be operated in their primary elliptic modes instead of secondary elliptic modes [78]. It is worth noting that (111) SCS substrates can be assumed to have isotropic material properties only for the in-plane vibration motion.

Again, to eliminate the backside packaging requirement, perforations need to be added to the disk. The same perforation design method employed for (100) SCS disks is applied to (111) SCS disks. However, in (111) SCS substrates, release holes need to be placed and repeated symmetrically every 45º, instead of every 30º as required in (100) SCS substrates. ANSYS simulation results for primary elliptic modes in 800μm diameter (111) SCS perforated disks show frequency splits of 720Hz and 130Hz, respectively, for large non-uniform-size holes and for 6μm uniform holes, shown in Figure 3-5. In (111) silicon disk gyroscopes, the capacitive electrodes should be located at every 45º to maximize the sense and drive transduction area and subsequently enhance the sensitivity.

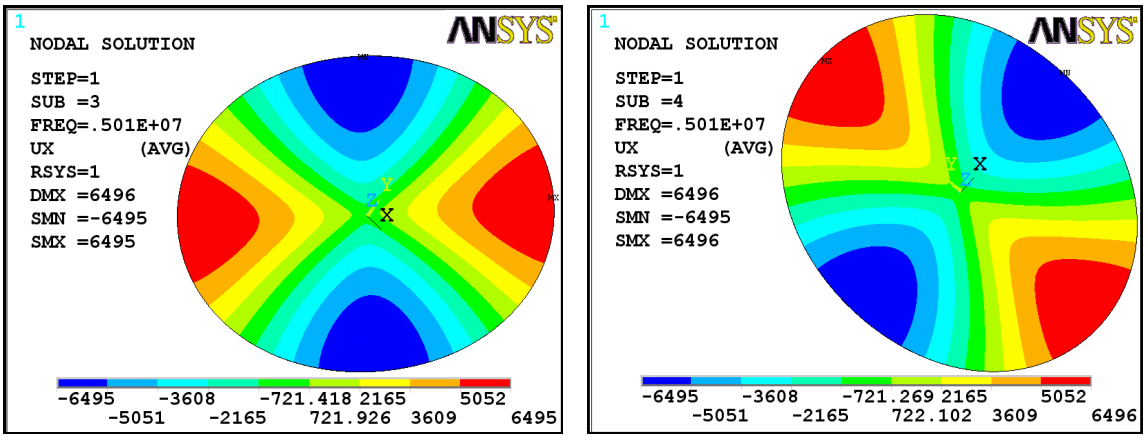

(a)

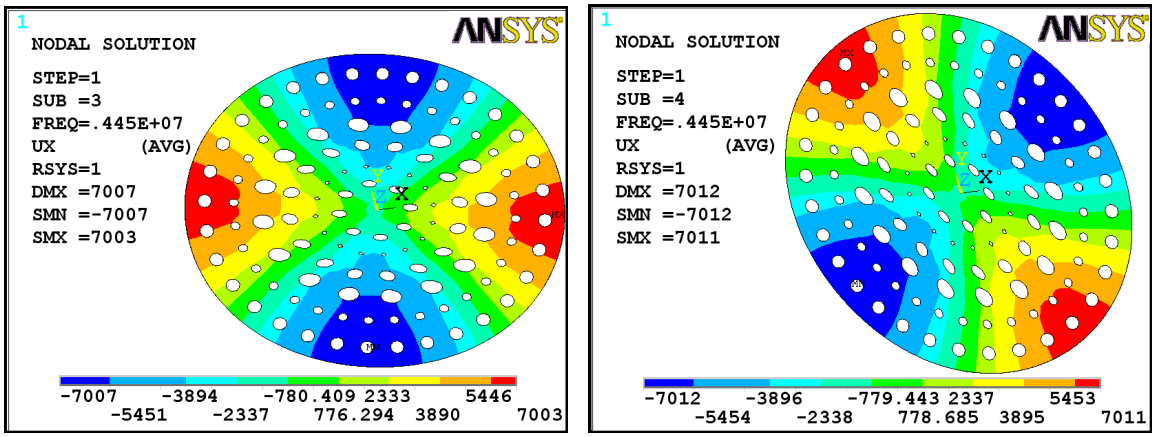

(b)

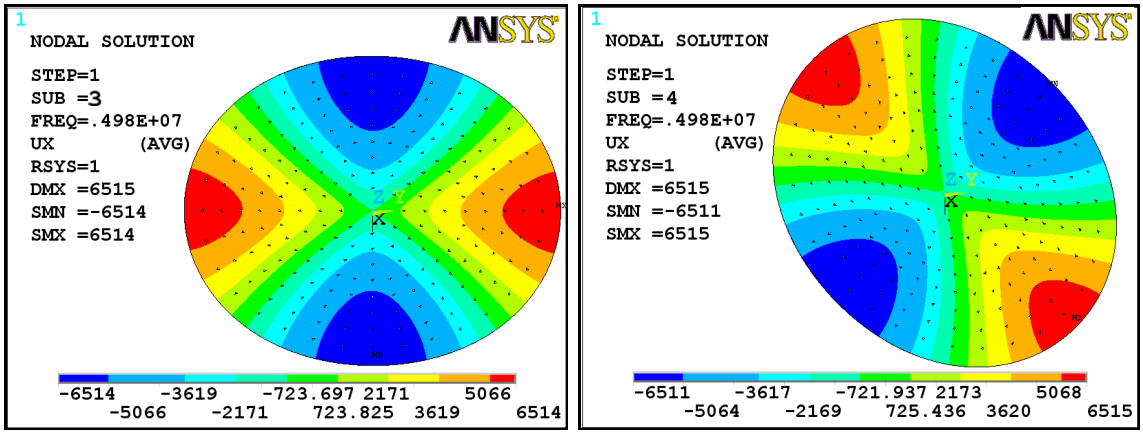

(c)

Figure 3-5: ANSYS simulation results of primary elliptic degenerative modes for: an 800μm diameter: (a) solid disk with Δf=70Hz, (b) large non-uniform sized holes with Δf=720Hz, (c) 6μm-diameter uniform sized holes with Δf=130Hz in (111) silicon substrate.

3.5 DERIVATION OF NORMAL BULK MODE EQUATIONS

Although some work has been done to investigate the in-plane extensional modes of disk structures [79], modal analysis for degenerative elliptic modes is not documented. In this section, the equations of motion for solid disks operating in their elliptic modes are derived, and the response to an applied rotation rate is calculated. To simplify the modal equations, solid disk structures, without any perforations, are assumed in the following analysis.

In general, displacement of a linear elastic body due to vibration can be written as a linear combination of its normal mode shape functions and its amplitudes [80]. For a disk gyroscope, we are interested in either primary or secondary elliptic modes in (111) SCS and (100) SCS substrates, respectively. The chosen elliptic mode actually consists of two degenerative modes, utilized as drive and sense modes. Accordingly, the vibration displacement of each point on the disk is a summation of both degenerative mode displacements as:

$$\begin{aligned} u_r &= q_1\phi_{r1} + q_2\phi_{r2} \\ u_\theta &= q_1\phi_{\theta 1} + q_2\phi_{\theta 2} \end{aligned} \tag{3-1}$$

where u_r and u_θ are the radial and circumferential components of the displacement vector in a vibrating disk and ϕ_r and ϕ_θ are the mode shape functions in the radial and circumferential directions, respectively. And, q_1, q_2 are the amplitudes of the two degenerative modes. Subscripts 1 and 2, respectively, represent the first degenerative mode (drive) and second degenerative mode (sense). The mode shape functions for a solid disk [79], operating in its bulk modes, are:

$$\begin{aligned} \phi_{r1} &= U_r \cos(m\theta) \qquad \phi_{\theta 1} = U_\theta \sin(m\theta) \\ \phi_{r2} &= -U_r \sin(m\theta) \qquad \phi_{\theta 2} = U_\theta \cos(m\theta) \end{aligned} \tag{3-2}$$

Where m is the mode order, equal to 2 for the primary elliptic modes and 3 for the secondary elliptic modes. The normalized displacements in the radial and circumferential directions, U_r and U_θ [81] are given in (3-3).

$$\begin{aligned} U_r &= \left[R\frac{d}{dr} J_m(\frac{k_m r}{R}) + \frac{m}{r} R\xi_m J_m(\frac{h_m r}{R}) \right] \\ U_\theta &= \left[-\frac{m}{r} R J_m(\frac{k_m r}{R}) - R\xi_m \frac{d}{dr} J_m(\frac{h_m r}{R}) \right] \end{aligned} \tag{3-3}$$

The normalized displacements are expressed in terms of Bessel functions of the first kind (J_m) as well as k_m and h_m, which are both dimensionless frequency parameters as follows:

$$k_m = \frac{R\omega_0}{\sqrt{E/\rho(1-\upsilon^2)}} \tag{3-4}$$

$$h_m = \frac{R\omega_0}{\sqrt{E/2\rho(1+\upsilon)}} \tag{3-5}$$

where R and ω_0 are the disk radius and natural frequency, respectively. The material properties of the device are defined by E, ρ, and υ which are Young's modulus, density and Poisson ratio, respectively. Besides the frequency parameters (k_m and h_m), ξ_m is the next parameter in (3-3) that needs to be addressed. ξ_m is the ratio of the constants in elastic waves as explained in detail in [79].

$$\xi_m = \frac{J_m(k_m)}{J_m(h_m)} \cdot \frac{2\dfrac{k_m J_{m-1}(k_m)}{J_m(k_m)} + {h_m}^2 - 2m(m+1)}{2m\left[\dfrac{h_m J_{m-1}(h_m)}{J_m(h_m)} - (m+1)\right]} \tag{3-6}$$

This depends on the Poisson ratio and the operating mode number (m) in the resonating structure. With k_m, h_m *and* ξ_m known, the normalized displacements (U_r and U_θ) can be calculated, completely defining the mode shape functions (ϕ_r and ϕ_θ).

Next, the expressions for the amplitude of the two modes (q_1, q_2) should be determined to fully quantify the displacements (u_r and u_θ). To accomplish this, the normal mode differential equations need to be solved. One of the well-known methods that can be employed is the Lagrange method, which is a purely scalar treatment for dynamic systems. In this method, the total differential of conservative energies is equated with the sum of any non-conservative forces (generalized forces), and these terms are expressed in generalized coordinates (q_i) [82]. As a result, the kinetic energy (T_i) and potential energy (U_i) along with the generalized forces (D_i) are derived for degenerative modes in BAW gyroscopes and employed in (3-7) to define the motion equations.

$$\frac{d}{dt}\frac{\partial T_i}{\partial \dot{q}_i} - \frac{\partial T_i}{\partial q_i} + \frac{\partial U_i}{\partial q_i} = D_i \tag{3-7}$$

3.5.1 KINETIC ENERGY

The kinetic energy can originate from both a vibration motion and a rigid body motion (rotational motion) of a resonating disk structure. If the effects of rotary inertia are neglected, the kinetic energy of an elemental section of a disk is determined by the

absolute velocity of its center. The velocity of an infinitesimal element of a disk corresponding to an applied rotation rate Ω_z is given by:

$$v = \dot{u} + u \times \Omega_z \tag{3-8}$$

where u is the total displacement of an infinitesimal element. And the kinetic energy of the disk with volume (V) follows as:

$$T = \frac{1}{2} \oint \rho |v|^2 \, dV \tag{3-9}$$

Substituting the radial and circumferential displacements and velocities into (3-8) and subsequently (3-9), the kinetic energy of the disk can be simplified and summarized as:

$$\begin{aligned} T = & \frac{1}{2} M_1 \dot{q}_1^{\,2} + \frac{1}{2} M_2 \dot{q}_2^{\,2} + \\ & \frac{1}{2} \Omega_z^{\,2} \left(M_1 q_1^{\,2} + M_2 q_2^{\,2} \right) + \Omega_z \gamma \left(q_1 \dot{q}_2 - q_2 \dot{q}_1 \right) \end{aligned} \tag{3-10}$$

where M_1 and M_2 are respectively the effective mass while the disk is vibrating at its drive and sense elliptic modes and they are expressed in (3-11) and (3-12) . And γ is the Coriolis coupling between the two modes as stated in (3-13).

$$M_1 = \oint \rho \left(\phi_{r1}^{\,2} + \phi_{\theta 1}^{\,2} \right) dV \tag{3-11}$$

$$M_2 = \oint \rho \left(\phi_{r2}^{\,2} + \phi_{\theta 2}^{\,2} \right) dV \tag{3-12}$$

$$\gamma = \oint \rho \left(\phi_{r1} \phi_{\theta 2} - \phi_{r2} \phi_{\theta 1} \right) dV \tag{3-13}$$

where ϕ_{r1}, ϕ_{r2}, $\phi_{\theta 1}$ and $\phi_{\theta 2}$ are the mode shape functions and can be determined from (3-2) for a disk operating in its BAW modes. The effective mass of a BAW disk gyroscope can be evaluated from M_1.

3.5.2 POTENTIAL ENERGY

The total potential energy in micromachined vibratory gyroscopes consists of a mechanical component (U_m) and an electrical component (U_e). The mechanical potential energy originates from the in-plane extensional motion of BAW modes, while the electrical potential energy comes from the applied electrostatic forces. The mechanical component of the potential energy can be expressed in terms of the stored strain energy as follows:

$$U_m = \frac{1}{2}\oint(\varepsilon_r\sigma_r + \varepsilon_\theta\sigma_\theta + \varepsilon_z\sigma_z + \gamma_{r\theta}\tau_{r\theta} + \gamma_{rz}\tau_{rz} + \gamma_{\theta z}\tau_{\theta z})dV \tag{3-14}$$

where σ and τ are the normal and shear stress and ε and γ are the normal and shear strain, respectively. Since elliptic degenerative modes only involve in-plane motion, normal and shear stresses in z direction were negligible. In addition, the effects of shear stress in the r and θ directions were not considered for simplicity. The mechanical potential energy equation can be simplified as:

$$U_m = \frac{1}{2}\oint(\varepsilon_r\sigma_r + \varepsilon_\theta\sigma_\theta)dV \tag{3-15}$$

According to Hooke's law, normal strains can be written in the form of normal stresses [83] in radial (ε_r) and circumferential (ε_θ) directions in (3-16) and (3-17). Substituting these into the mechanical potential energy equation yields (3-18).

$$\varepsilon_r = \frac{1}{E}(\sigma_r - \nu\sigma_\theta - \nu\sigma_z) \tag{3-16}$$

$$\varepsilon_\theta = \frac{1}{E}(\sigma_\theta - \nu\sigma_r - \nu\sigma_z) \tag{3-17}$$

$$U_m = \frac{1}{2E}\oint(\sigma_r{}^2 + \sigma_\theta{}^2 - 2\nu\sigma_r\sigma_\theta)dV \tag{3-18}$$

Also, normal stresses of BAW modes in radial and circumferential directions can be defined in terms of displacements (u_r, u_θ), Young's modulus (E) and Poisson ratio (ν) from [84].

$$\begin{aligned}\sigma_r &= \frac{E}{1-\nu^2}\left(\frac{\partial u_r}{\partial r} + \frac{\nu}{r}\left(u_r + \frac{\partial u_\theta}{\partial\theta}\right)\right)\\ \sigma_\theta &= \frac{E}{1-\nu^2}\left(\nu\frac{\partial u_r}{\partial r} + \frac{1}{r}\left(u_r + \frac{\partial u_\theta}{\partial\theta}\right)\right)\end{aligned} \tag{3-19}$$

Afterwards, normal stresses from (3-19) are substituted into (3-18) in terms of radial and circumferential displacements and subsequently displacements from (3-1) are replaced with mode shape functions and amplitudes. Finally, the mechanical potential energy is summarized in terms of amplitudes and mechanical stiffness:

$$U_m = \frac{1}{2}K_{m1}q_1{}^2 + \frac{1}{2}K_{m2}q_2{}^2 \tag{3-20}$$

where K_{m1} is the mechanical stiffness of the disk due to the vibration at the drive mode:

$$K_{m1} = \left(\frac{E}{(1-\nu^2)}\right)\oint\left(\left(\frac{\partial\phi_{r1}}{\partial r}\right)\left(\frac{\partial\phi_{r1}}{\partial r} + \frac{2\nu}{r}\left(\phi_{r1} + \frac{\partial\phi_{\theta1}}{\partial\theta}\right)\right) + \left(\frac{1}{r^2}\right)\left(\phi_{r1} + \frac{\partial\phi_{\theta1}}{\partial\theta}\right)^2\right)dV \tag{3-21}$$

K_{m2} can be defined the same as K_{m1} but with r_1 and θ_1 replaced by r_2 and θ_2, respectively.

The electrical component of potential energy originates from the application of the electrostatic forces between the disk and surrounding electrodes. The total electrical potential energy can be found by adding the electrostatic energies corresponding to drive, sense and tuning voltages, producing,

$$U_e = -\frac{1}{2}C_d(V_d)^2 - \frac{1}{2}C_s(V_s)^2 - \frac{1}{2}\sum_{i=1}^{5}C_d(V_{Tdi})^2 - \frac{1}{2}\sum_{i=1}^{5}C_s(V_{Tsi})^2 \quad (3\text{-}22)$$

where C_d and C_s represent the drive and sense capacitances and V_d and V_s denote the voltages at the drive and sense electrodes, respectively. Also, V_{Td} and V_{Ts} are the tuning voltages for the drive and sense, respectively. The voltages in (3-22), are related to device terminal voltages, as:

$$V_d = V_p - v_{d-ac} \quad (3\text{-}23)$$

$$V_s = V_p \quad (3\text{-}24)$$

$$V_{Td} = V_p - V_{T-drive} \quad (3\text{-}25)$$

$$V_{Ts} = V_p - V_{T-sense} \quad (3\text{-}26)$$

where V_p, $v_{d\text{-}ac}$, $V_{T\text{-}drive}$ *and* $V_{T\text{-}sense}$ are, respectively, the polarization voltage applied to the disk, the AC signal applied to vibrate the disk at the drive mode, and the DC voltages used to electrostatically tune the drive and sense modes. The general form of a capacitance between an electrode and a disk is expressed in (3-27) and the schematic is shown in Figure 3-6.

$$C = \int_{\theta_n - \frac{\Delta\theta_n}{2}}^{\theta_n + \frac{\Delta\theta_n}{2}} \frac{\varepsilon_0 hR}{d_0\left(1 - \frac{\Delta d}{d_0}\right)} d\theta \tag{3-27}$$

where h, R, d_0 and Δd are the disk thickness, disk radius, the initial gap between the electrode and the disk and the capacitive gap changes, respectively. Also, $\Delta\theta_n$ is the angle that each electrode spans and θ_n is the angle from the x-axis to the center of the nth electrode.

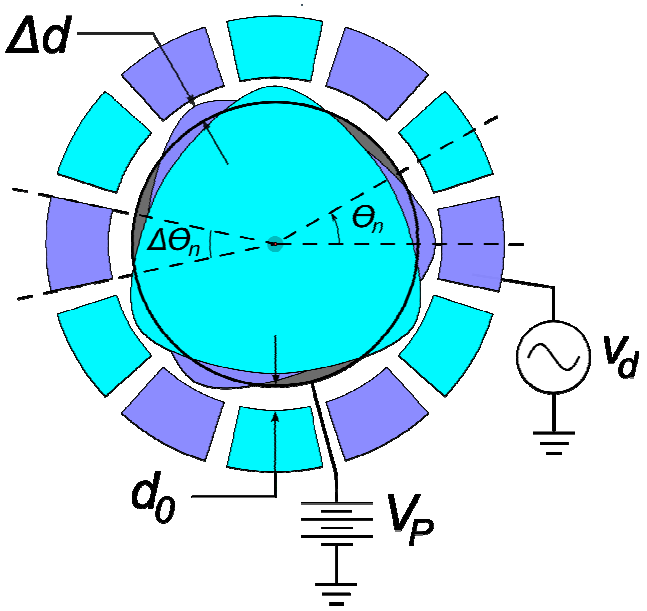

Figure 3-6: The schematic view of a capacitive disk gyroscope operating at its secondary elliptic modes.

Symmetrical electrodes around the disk result in equal capacitive area and initial capacitive gaps for drive, sense and tuning capacitances. However, the change in the capacitive gap (Δd) depends on the mode of vibration and the location of the electrode. In addition, the capacitive gap (d_0) is much smaller than the radius (R) of the disk gyroscope ($d_0 << R$), making any circumferential displacement very small compared to the radial

displacements. Thus, only the radial displacement is considered for the change in the capacitive gap as following:

$$\Delta d = u_r = q_{r1}\phi_{r1} + q_{r2}\phi_{r2} \tag{3-28}$$

Given that the drive electrode is located at the anti-node line of the drive mode and at the node line of the sense mode, this implies that ($\phi_{r1}>>\phi_{r2}$) at the drive electrodes and similarly ($\phi_{r2}>>\phi_{r1}$) at the sense electrodes. However, due to fabrication non-idealities, the maximum mode shapes displacement might be slightly misaligned with the center of an electrode, which can be aligned by cancelling the quadrature errors. Substituting the mode shape functions (ϕ_{r1} and ϕ_{r2}) into (3-28) and integrating over the electrode length, the total capacitances between the disk and the drive electrode vibrating at its elliptic modes can be expressed as:

$$C_d = \frac{\varepsilon_0 hR}{d_0}\left(\Delta\theta_n + \left(\frac{2U_r}{md_0}\sin(\frac{m\Delta\theta_n}{2})\right)q_1 + \frac{{U_r}^2}{2{d_0}^2}\left(\Delta\theta_n + \frac{1}{m}\sin(m\Delta\theta_n)\right){q_1}^2\right) \tag{3-29}$$

$$C_s = \frac{\varepsilon_0 hR}{d_0}\left(\Delta\theta + \left(\frac{2U_r}{md_0}\sin(\frac{m\Delta\theta_n}{2})\right)q_2 + \frac{{U_r}^2}{2{d_0}^2}\left(\Delta\theta_n + \frac{1}{m}\sin(m\Delta\theta_n)\right){q_2}^2\right) \tag{3-30}$$

The total capacitances at the drive and sense electrodes as well as voltages from (3-23) to (3-26) can be substituted into the potential energy expression in (3-22). This gives (3-31), expressing the total electrical stiffness of the disk in its first elliptic mode (the drive mode). For the second elliptic mode (the sense mode), the electrical stiffness is the same as K_{e1} in (3-31) but the drive voltages (V_d and V_{Tdi}) should be replaced with the sense voltages (V_s and V_{Tsi}).

$$K_{e1} = \frac{\varepsilon_0 h R U_r^{\,2}}{2 d_0^{\,3}} (V_d^{\,2} + \sum_{i=1}^{5} V_{Tdi}^{\,2}) \times \left(\Delta\theta_n + \frac{1}{m} \left(\sin\left(2m(\theta_n + \frac{\Delta\theta_n}{2} \right) - \sin\left(2m(\theta_n - \frac{\Delta\theta_n}{2} \right) \right) \right) \right) \tag{3-31}$$

3.5.3 VISCOUS DAMPING

In BAW gyroscopes, each degenerative mode is associated with its own damping forces, which are treated as non-conservative forces D_1 and D_2 in Lagrange's equations:

$$\begin{aligned} D_1 &= -C_1 \dot{q}_1 \\ D_2 &= -C_2 \dot{q}_2 \end{aligned} \tag{3-32}$$

where C_1 and C_2 are the damping coefficients. The damping forces are not generally aligned with normal vibration modes [80]. However, it is assumed that they are aligned with the electrode centers for simplicity.

3.5.4 EQUATIONS OF MOTIONS

Given the kinetic energy (T), potential energy ($U=U_m+U_e$) and the generalized forces (D) of the BAW gyroscope in terms of the generalized coordinates (q_i), the system of motion equations is derived using the Lagrange's method [85]. Thus, the coupled second-order differential equations used to model the disk gyroscope are expressed in (3-33) and can be solved for q_1 and q_2.

$$\begin{aligned} M_1 \ddot{q}_1 + C_1 \dot{q}_1 - 2\gamma\Omega_z \dot{q}_2 - \gamma\dot{\Omega}_z q_2 - M_1 \Omega_z^{\,2} q_1 + (K_{m1} - K_{e1}) q_1 &= F_1 \\ M_2 \ddot{q}_2 + C_2 \dot{q}_2 - 2\gamma\Omega_z \dot{q}_1 - \gamma\dot{\Omega}_z q_1 - M_2 \Omega_z^{\,2} q_2 + (K_{m2} - K_{e2}) q_2 &= F_2 \end{aligned} \tag{3-33}$$

M_1, M_2, γ, K_{m1} and K_{e1} are respectively defined in (3-11), (3-12), (3-13) and (3-21). C_1 and C_2 are the damping coefficient for the drive and sense modes, respectively. Also, F_1 originates from the electrical potential term and is derived and expressed as:

$$F_1 = \mp \frac{\varepsilon_0 hRU_r}{md_0^2}(V_d^2 + \sum_{i=1}^{5} V_{Tdi}^2)\left(\sin\left(m\theta_n + \frac{m\Delta\theta_n}{2}\right) - \sin\left(m\theta_n - \frac{m\Delta\theta_n}{2}\right)\right) \tag{3-34}$$

In addition, F_2 is the same as F_1 except that drive voltages (V_d and V_{Tdi}) should be replaced with the sense voltages (V_s and V_{Tsi}).

3.6 ANGULAR GAIN ESTIMATION

One of the critical parameters in the design of a Coriolis gyroscope is the angular gain. When rotation is applied to the sensor, the node lines of the vibration pattern lag behind the rotation of the sensor. The angular gain (A_g) is defined as the ratio of the change in the vibration pattern angle to the applied angle of rotation (Ω_z). The angular gain depends on the sensor structure as well as the type of resonant modes in operation. In order to calculate the angular gain, matched elliptic mode frequencies with zero damping are assumed. Also, the angular acceleration coupling is negligible compared to the Coriolis coupling. With these assumptions, the normal mode equations (3-33) are simplified to:

$$\begin{aligned} \ddot{q}_1 - \frac{2\gamma}{M}\Omega_z \dot{q}_2 + (\omega_0^2 - \Omega_z^2)q_1 = 0 \\ \ddot{q}_2 + \frac{2\gamma}{M}\Omega_z \dot{q}_1 + (\omega_0^2 - \Omega_z^2)q_2 = 0 \end{aligned} \tag{3-35}$$

If a constant rotation rate (Ω_z) is applied to the gyroscope, the drive and sense amplitudes (q_1, q_2) are obtained by solving (3-35):

$$q_1 = A\cos\left(\frac{\gamma}{M}\Omega_z t\right)\sin(\omega t) \tag{3-36}$$

$$q_2 = -A\sin\left(\frac{\gamma}{M}\Omega_z t\right)\sin(\omega t) \tag{3-37}$$

where A is a constant amplitude term and ω is defined as:

$$\omega = \sqrt{\omega_0^{\,2} - \Omega_z^{\,2}\left[1 - \left(\frac{\gamma}{M}\right)^2\right]} \tag{3-38}$$

where ω_0, Ω_z, γ and M are, respectively, the resonant frequency, an applied rotation rate around the z-axis, the Coriolis coupling in (3-13) and the effective mass in (3-11) .

The drive mode amplitude (q_1) is assumed to have the maximum amplitude (A) at 0°. This is because the electrode located at 0° is aligned with the anti-node of the drive mode. With the application of a constant rotation rate (Ω_z), the vibration pattern also rotates at a related constant rate. After a certain time (t), the drive mode transfers to the sense mode due to the mode's degenerative interrelation and the following is applied from (3-39):

$$\frac{\gamma}{M}\Omega_z t = \frac{\pi}{2} \tag{3-39}$$

At this time, the amplitude of the sense mode will reach its maximum value and the sensor has rotated through an angle of β.

$$\beta_{rotation-angle} = \Omega_z t = \frac{\pi M}{2\gamma} \tag{3-40}$$

While the sensor rotates through β, Coriolis force shifts the vibration pattern through an angle (θ) from the drive mode to its degenerative mode (sense mode). The degenerative mode of primary elliptic mode in (111) SCS is at 45° spatially apart. However, the secondary elliptic mode in (100) SCS has a vibration pattern of 30°. Taking the ratio of the vibration pattern angle (θ) to the angle of rotation in the sensor (β), the angular gains for a disk operating in its elliptic mode can be stated as:

$$A_g = \frac{\theta_1}{\beta_1} = \frac{\frac{\pi}{2m}}{\frac{\pi M}{2\gamma}} = \frac{\gamma}{mM} \tag{3-41}$$

where M and γ are respectively expressed in (3-11) and (3-13) and m is the mode number.

To evaluate the angular gain (A_g) for primary and secondary elliptic modes, the mode shape functions (3-2) are integrated over the disk volume to determine the Coriolis coupling coefficient (γ) and the effective mass (M). Given the disk radius (R) and the material properties (E, ν) of the disk as well as the resonance frequency of operation (ω_0), frequency parameters (k_m) and (h_m) are further estimated. Subsequently, the ratio of elastic wave constants ξ_m is estimated by solving the Bessel function of frequency parameters. The maximum normalized displacements U_r and U_θ are calculated, and the mode shape functions are determined in terms of (r,θ) and integrated over the disk volume. Finally, the angular gain values are calculated. All of the design parameters are summarized in Table 3-1 for a solid disk operating in either primary or secondary elliptic

modes. As can be seen, the estimated angular gain of a solid disk structure is ~1.9 times larger for primary elliptic modes than for secondary elliptic modes. The Matlab code used to estimate the design parameters are presented in Appendix B.

Table 3-1: The design parameters in BAW solid disk gyroscopes.

Material/mode	**(111) SCS Primary elliptic mode (m=2)**	**(100) SCS Secondary elliptic mode (m=3)**
Poisson's ratio (ν)	0.262	0.177
Young modulus (*E, GPa*)	168.9	148.43
Mass density (ρ, Kg/m^3)	2330	2330
Frequency parameter (k_m)	1.4243	2.2990
Frequency parameter (h_m)	2.3447	3.5836
Const. elastic waves ratio (ξ_m)	2.2330	1.1378
Frequency (MHz)	ANSYS 5.01	ANSYS 7.51
	Theoretical 5.00	Theoretical 7.42
Dimensionless maximum radial displacement (U_r) at r=R	1.5105	0.9430
Dimensionless maximum circumferential displacement (U_θ) at r=R	0.4621	0.0705
Effective mass *(M, Kg)*	2.0676e-8	1.4694e-008
Coriolis coupling coeff. (γ, *Kg*)	1.8954e-8	1.0203e-008
Angular gain (A_g)	***0.4584***	***0.2314***

It is worth noting that our derivation is based on employing an isotropic material, but (100) SCS is anisotropic. To facilitate estimating the design parameters for a (100) SCS disk operating in its secondary modes, equivalent isotropic material properties should be approximated. As reported in [79], (100) SCS disk can be treated as an isotropic disk with the material properties in the direction of anti-node lines of the mode shape. Using this assumption in [79], they achieved less than 0.1% difference in the resonance frequency between the theoretical and numerical simulation. In [79], they modeled for primary elliptic modes, in which each mode's anti-node lines are crystallographically

equivalent. The same method can be employed for a (100) SCS disk operating in its secondary elliptic modes. However, in each of those modes the anti-node lines are not in the same crystallographical line, one aligned with <110> and two aligned with <1 3.75 0> directions. As a result, the material properties for three anti-node lines were calculated using [86] and averaged together (arithmetic mean) to estimate equivalent isotropic material properties. This assumption was verified, in ANSYS simulation results and theoretical calculations, against an anisotropic ANSYS simulation. The frequency responses of a disk operating in its secondary elliptic modes were modeled using an anisotropic material properties for (100) SCS and an equivalent isotropic material properties. The difference between the frequencies of the two models was observed to be ~1% for both degenerative modes and the frequency separations between the two degenerative modes were identical. Accordingly, in our calculations, the equivalent isotropic material properties (with E of 143.43 and υ of 0.177) are assumed for all design parameters in (100) SCS disks operating in its secondary elliptic modes.

3.7 FREQUENCY TUNING METHOD

Electrostatic tuning is a well-established technique for matching the resonant frequencies in capacitive-based micromachined gyroscopes. This is vital to lessening the effects of non-idealities and reaching the superior performance delivered by matched-mode operation. Developing a frequency tuning procedure for BAW gyroscopes requires analysis of the effect of electrostatic forces on the resonance frequencies of the degenerative modes. In this study, a tuning scheme is provided only for secondary elliptic

degenerative modes in (100) SCS. A similar method can be applied for tuning of primary elliptic degenerative modes in (111) SCS.

To electrostatically tune and match two modes, three approaches can be employed. First is tuning only the drive mode and matching it with the frequency of the sense mode [10]. Second is tuning the sense mode and matching it with the frequency of the drive mode. Third is tuning of both drive and sense modes simultaneously. The last approach lowers the required tuning voltages significantly, and this is the focus of this work.

Assume that a BAW disk gyroscope is driven in its secondary elliptic modes by an electrode located on the *x*-axis and the response is sensed at an electrode located on the *y*-axis, shown in Figure 3-7.

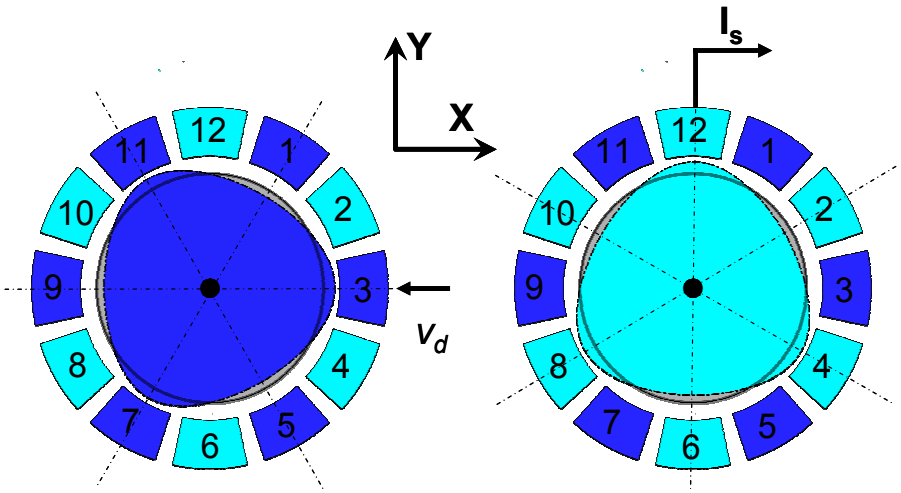

(a) Drive mode (b) Sense mode

Figure 3-7: The schematic view of secondary elliptic modes (a) drive mode excited at *x*-axis with antinode lines located at electrodes 1, 3, 5, 7, 9 at kπ/3 with k=0,1…12, (b) sense mode detected at *y*-axis with antinode lines located at electrodes 2, 4, 6, 8, 10 at kπ/6 with k=0,1…12. It is worth noting that electrodes 3 and 12 are used to drive and sense the modes. Electrode 9 is also employed for monitoring the drive output signal.

Assume that the drive mode has a lower initial frequency than the sense mode ($f_{0\text{drive}}<f_{0\text{sense}}$). Consequently, the frequency of the drive mode should be increased while

the sense mode's frequency needs to be decreased. It is well-known that the frequency is related to the electrical stiffness from [87] as following:

$$f_0 = \frac{1}{2\pi}\sqrt{\frac{K_m - K_e}{M}} \tag{3-42}$$

where K_e, K_m and M are the mechanical stiffness, electrical stiffness and the effective mass of resonant structure, respectively. The latter two's invariance, for a given device, makes K_e the sole dynamic determinant of f_0. In order to reach matched mode, K_e for both drive and sense modes should be adjusted appropriately.

The general expression for the electrical stiffness of a disk operating in its elliptic modes is presented in (3-31). Setting m equal to 3 (for secondary elliptic mode) and θ_n to the appropriate values for the antinode lines of the drive and sense modes, the electrical stiffnesses K_{e1} for the drive mode and K_{e2} for the sense mode, are simplified as:

$$K_{e1} = \frac{\varepsilon_0 hR}{d_0}\left(\frac{{U_r}^2}{{d_0}^2}\left(\frac{\Delta\theta_n}{2} - \frac{\sin(m\Delta\theta_n)}{2m}\right)\right)\left(V_p - V_{T-drive}\right)^2 \tag{3-43}$$

$$K_{e2} = \frac{\varepsilon_0 hR}{d_0}\left(\frac{{U_r}^2}{{d_0}^2}\left(\frac{\Delta\theta_n}{2} - \frac{\sin(m\Delta\theta_n)}{2m}\right)\right)\left(V_p - V_{T-sense}\right)^2 \tag{3-44}$$

As one can observe, for a specific device dimension, the electrical stiffness depends solely on the tuning voltages. In particular, the electrical stiffness of a mode is independent of the direction of the tuning electrode, as long as it is located at an antinode of the mode. Since the resonant frequency is inversely proportional to the electrical stiffness, the stated goals of raising the drive frequency while lowering the sense frequency are achieved by choosing $V_{T\text{-}drive}>0$ and $V_{T\text{-}sense}<0$. The cases in which the

untuned drive frequency is higher than the sense frequency, analogously, are accommodated by choosing $V_{T\text{-}drive}<0$ and $V_{T\text{-}sense}>0$.

Furthermore, the electrical stiffness of either the drive or sense mode from (3-43) or (3-44) can be substituted into (3-42). The derivative of the frequency with respect to the applied tuning voltages can then be derived and expressed as follows:

$$\frac{\partial f_{tuning}}{\partial V} = \frac{-1}{(2\pi)^2 M f_0}\left[\frac{\varepsilon_0 h R {U_r}^2}{{d_0}^3}\left(\frac{\Delta\theta_n}{2} - \frac{\sin(m\Delta\theta_n)}{2m}\right)\left(V_p - V\right)\right] \tag{3-45}$$

where h, R, $\Delta\theta_n$, U_r and d_0 are, respectively the disk thickness, disk radius, electrode angular span, maximum normalized displacement, and the capacitive gap. Also, M, f_0 and m are the effective mass, the operating frequency and the mode number, respectively. This equation can be further simplified by replacing the effective mass (M) and the ($R\Delta\theta_n$) as an electrode length (L_e), thus

$$\frac{\partial f_{tuning}}{\partial V_{tuning}} = \frac{\varepsilon_0 {U_r}^2 L_e}{4\rho f R^2 C_{effec-mass}(\pi d_0)^3} V_{tuning} \tag{3-46}$$

Where $C_{effec\text{-}mass}$ is the effective mass coefficient that can be determined by taking the ratio of the effective mass (M) from (3-11), which is normalized to the maximum normalized displacement (U_r *at* $r=R$), to the total mass of the disk. Also, from (3-46), the frequency tuning is linearly proportional to the electrode length, the square of the maximum normalized displacement and the tuning voltages; however it is inversely proportional to the square of the disk radius, mass effective coefficient, the operating frequency and the cubed of capacitive gaps. This implies that the frequency tuning is heavily dependent on the capacitive gap and is not affected by the disk thickness. As a result, sub-micron capacitive gaps should be employed in BAW gyroscopes to expedite

frequency tuning and limit tuning voltages. In addition, maximal electrode length lowers the tuning voltages further.

3.8 SENSITIVITY ANALYSIS

Coriolis-induced sense mode vibrations are detected through change in the capacitance at the sense electrodes to determine the sensitivity of a micromachined vibratory gyroscope. A sinusoidal electrostatic force is applied to the assigned drive electrode to vibrate the disk in its first degenerative elliptic mode (the drive mode). The vibration energy is stored in this mode and the disk continues to vibrate indefinitely, provided that there is no damping or rotation. When rotation is applied, the Coriolis acceleration transfers the stored vibration energy between the two degenerative modes until all the energy is transferred to the second mode (sense mode). Consequently the Coriolis induced sense mode vibration change the capacitive gap at the sense electrode, which can be measured as devices' rotation response. Next, a number of rotation rates are applied and the responses are measured. The Scale factor is generally evaluated as the slope of the straight line that can be fitted to a plot of output signal versus input rotation rate.

In this study, we consider an ideal device with matched mode frequencies and symmetric damping. As the angular acceleration coupling is insignificant in comparison with Coriolis coupling, and as centrifugal stiffness is very small compared to mechanical and electrical stiffness, they are both assumed to be neglected in (3-33). Consequently, the drive and sense mode second-order differential equations are simplified to:

$$\ddot{q}_1 + \frac{\omega_0}{Q}\dot{q}_1 + {\omega_0}^2 q_1 = \frac{F_1}{M_1}$$
$$\ddot{q}_2 + \frac{\omega_0}{Q}\dot{q}_2 + 2mA_g\Omega_z\dot{q}_1 + {\omega_0}^2 q_2 = 0 \quad (3\text{-}47)$$

A sinusoidal drive signal is applied to the single drive electrode while the polarization voltage is applied to the center of the disk through the poly trace. This electrostatic force between the disk and the drive electrode vibrates the disk in its elliptic mode. Consequently, the drive mode amplitude (q_1) can be written as:

$$q_1 = A_1 \sin(\omega_0 t) \quad (3\text{-}48)$$

where A_1 and ω_0 are, respectively, the amplitude constant and the natural frequency of the disk at the driven elliptic mode.

Substituting the drive mode amplitude (q_1) and applying the first and second derivatives of q_1 into (3-47), the electrostatic drive force can be expressed as:

$$F_d = \frac{{\omega_0}^2 M}{Q} A_1 \cos(\omega_0 t) \quad (3\text{-}49)$$

For a gyroscope operating in matched mode, the response of the sense mode to rotation occurs at the same frequency and phase as the drive mode. Thus, the amplitude of the sense mode response (q_2) can be expressed as:

$$q_2 = A_2 \sin(\omega_0 t) \quad (3\text{-}50)$$

Leveraging the previous definition of angular gain, the sense mode equations in (3-47) can be written in terms of the angular gain for primary and secondary elliptic modes as:

$$\ddot{q}_2 + \frac{\omega_0}{Q}\dot{q}_2 + 4\mathrm{A}_g\Omega_z\dot{q}_1 + {\omega_0}^2 q_2 = 0 \tag{3-51}$$

$$\ddot{q}_2 + \frac{\omega_0}{Q}\dot{q}_2 + 6\mathrm{A}_g\Omega_z\dot{q}_1 + {\omega_0}^2 q_2 = 0 \tag{3-52}$$

The sense to drive mode amplitude ratios for primary and secondary elliptic modes are taken, using q_1 and q_2 and their derivatives in (3-51) and (3-52), as:

$$\frac{A_2}{A_1} = \frac{q_2}{q_1} = -\frac{4\mathrm{A}_g\Omega_z Q}{\omega_0} \tag{3-53}$$

$$\frac{A_2}{A_1} = \frac{q_2}{q_1} = -\frac{6\mathrm{A}_g\Omega_z Q}{\omega_0} \tag{3-54}$$

Accordingly, the sense mode amplitude is linearly proportional to the matched-mode quality factor (Q), angular gain (A_g) and the drive mode amplitude (q_1), and it is also inversely proportional to the operating resonance frequency (ω_0). Therefore, as high frequency gyroscopes raise ω_0, a high matched-mode quality factor is required to preserve the sense mode amplitude and consequently the device's sensitivity.

To determine the sensitivity of a BAW gyroscope, the total capacitance change at the sense electrode due to an applied rotation rate should be evaluated. The total capacitance at the sense electrode, using Taylor series, can be stated in (3-55). In which the only linear part of capacitance change has been considered. If it is desired, the higher term from Taylor series can be replaced and subsequently the non-linear term of capacitance changes could be evaluated.

$$C = \int_{\theta_n - \frac{\Delta\theta_n}{2}}^{\theta_n + \frac{\Delta\theta_n}{2}} \frac{\varepsilon_0 hR}{d_0}\left(1 + \frac{u_{r=R}}{d_0}\right)d\theta = \frac{\varepsilon_0 hR}{d_0}\int_{\theta_n - \frac{\Delta\theta_n}{2}}^{\theta_n + \frac{\Delta\theta_n}{2}}\left(1 - \frac{q_2\phi_{r2}}{d_0}\right)d\theta \tag{3-55}$$

After integration and simplification of (3-55) , the sense capacitance (C_s) can be written in terms of an initial capacitance (C_{s0}) and the change in capacitance (δC_s) due to the vibrational motion.

$$C_s = C_{s0} + \delta C_s \tag{3-56}$$

$$C_{s0} = \frac{\varepsilon_0 hR}{d_0} \tag{3-57}$$

$$\delta C_s = \frac{2\varepsilon_0 hRq_2 U_{r=R}}{md_0^{\,2}}\sin(m\theta)\sin(m\frac{\Delta\theta}{2}) \tag{3-58}$$

It is worth noting that $\sin(m\theta)$ is equal to 1 for both primary and secondary elliptic modes due to the multiplication of the mode number (m) by the vibration pattern angle (θ). Also, the sense mode amplitude (q_2) can be substituted from (3-53) and (3-54) into (3-58), giving the sensitivity for primary and secondary elliptic modes as:

$$\frac{\delta C_s}{\Omega_z} = \frac{8\varepsilon_0 hRq_1 A_g QU_{r=R}}{\omega md_{0^2}}\sin(m\frac{\Delta\theta}{2}) \tag{3-59}$$

$$\frac{\delta C_s}{\Omega_z} = \frac{12\varepsilon_0 hRq_1 A_g QU_{r=R}}{\omega md_{0^2}}\sin(m\frac{\Delta\theta}{2}) \tag{3-60}$$

As it can be observed, the sensitivity is linearly proportional to the angular gain. As calculated, A_g in (111) silicon BAW disk gyroscopes operating in the primary mode is ~ 1.9× larger than the identical device in (100) silicon operating in the secondary elliptic

mode. Thus, higher sensitivity can be achieved for devices implemented in (111) SCS. However, (100) silicon substrates have advantages in terms of CMOS compatibility and substrate availability compared to (111) silicon substrates.

In any case, the change of the sense capacitance due to the applied rotation is very small and it needs to be amplified properly to be readable. Therefore, each sense electrode is accompanied by a low noise trans-impedance amplifier (TIA) and two cascaded voltage amplifiers. The fully amplified signal is a cross-product of two signals (carrier and Coriolis), and can thus be treated as an amplitude-modulated (AM) signal. It is then demodulated to extract the rotation rate (Coriolis signal) by mixing the carrier signal from the drive loop with the AM output. Finally, a low-pass filter is used to separate the Coriolis signal from the mixer output [73]. Figure 3-8 shows the configuration for detecting the rotation response from the output signal at the sense electrode.

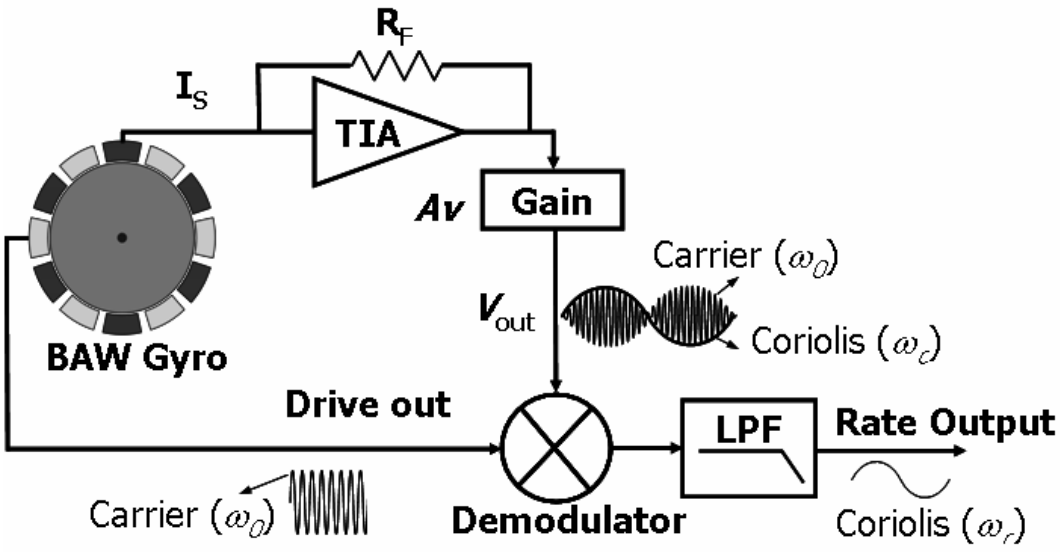

Figure 3-8: Readout circuitry used for measuring the rotation rate in capacitive BAW disk gyroscopes.

Utilizing the above circuit, the high-frequency BAW gyroscope sensitivity in terms of output voltage is discussed here. The output voltage due to an applied *z*-axis rotation rate can be derived using the chain rule:

$$\frac{v_{out}}{\Omega_z} = \frac{\delta C_s}{\Omega_z} \times \frac{v_{out}}{\delta C} \tag{3-61}$$

The capacitance change due to the rotation rate is given in (3-59) and (3-60), and the fully-amplified output voltage may also be stated as:

$$v_{out} = I_s R_f A_v \tag{3-62}$$

Where R_f and A_v are the gain of the TIA and the total gain of the cascaded voltage amplifiers, respectively. In addition, the output current at the sense electrode can be expressed as the total change of the charge over time:

$$I_s = \frac{dQ}{dt} = \frac{d}{dt}(C_{s\,pad} + C_{s0} + \delta C_s)V_p = \delta C_s V_p \omega_0 \tag{3-63}$$

The sense current I_s is substituted into (3-62), which is then substituted into the second term in (3-61). Finally, the sensitivity of the disk gyroscope in terms of output voltage is summarized as following for either primary or secondary elliptic modes.

$$\frac{v_{out}}{\Omega_z} = V_p R_f A_v \frac{4\varepsilon_0 h R q_1 A_g Q U_{r=R}}{{d_0}^2} \sin(m\frac{\Delta\theta}{2}) \tag{3-64}$$

It is worth nothing that utilizing the above sense amplifier configuration makes the sensitivity of BAW disk gyroscopes independent of the resonance frequency. To improve the sensitivity of BAW gyroscopes, high matched-mode Q as well as larger sense capacitance and smaller capacitive gaps are desired.

3.8 RESOLUTION ANALYSIS

Resolution, defined as the minimum detectable rotation rate, is a major performance parameter in a gyroscope [9]. The total resolution has two principal components: the Brownian noise, originating from the mechanical motion of the resonating structure, and the electronic noise, originating from the interface circuitry.

$$\Omega_{\min}(Total) = \sqrt{\Omega_{\min}(Brownian)^2 + \Omega_{\min}(Electronic)^2} \tag{3-65}$$

Brownian motion of the structure, which is the result of molecular collisions with the surrounding medium, represents the mechanical noise component (mechanical noise equivalent, MNEΩ). By equating the displacement caused by Brownian motion [32, 88] to the displacement induced by Coriolis acceleration (3-53) and (3-54), the mechanical resolution of BAW gyroscopes in a matched-mode operation can be derived as:

$$\Omega_{\min}(\text{Brownian}) = \frac{1}{2mA_g q_1}\sqrt{\frac{4k_B T_0}{\omega_0 MQ}} \tag{3-66}$$

Where q_1 is the drive amplitude; ω_0, M, and Q are the natural frequency, effective mass and effective quality factor at the sense mode, respectively; k_B is the Boltzmann constant, and T_0 is the absolute temperature.

The effective mass for disk gyroscopes operating in their BAW modes can be calculated by the integral for the kinetic energy in (3-11) and normalizing the result to the dimensionless maximum displacement at the disk edge [79, 89]. This is evaluated and reported later in this section.

Furthermore, the electronic noise (electronic noise equivalent, ENEΩ) arising from the interface circuitry should be considered. In order to do this, it is assumed that the output

noise (I_{noise}) has a white spectrum near the resonant frequency. Then, the electronic noise of the interface circuitry for either the primary or secondary elliptic modes at matched-mode operation can be stated in below:

$$\Omega_{\min}(electronic) = \frac{d_0{}^2 I_{noise}\sqrt{BW}}{4V_p q_{drive} Q A_g \left(\varepsilon_0 hRU_{r=R}\sin\left(\frac{m\Delta\theta}{2}\right)\right)} \tag{3-67}$$

where I_{noise} is the interface circuitry noise, referred to the input. As can be observed in (3-67), the electronic noise is linearly proportional to input-referred noise and is inversely proportional to the sense capacitance, the matched mode Q, angular gain and polarization voltage. This indicates that very large sense capacitance, very large $Q_{\text{matched-mode}}$, and ultra low input-referred noise can significantly lower the electrical noise in these gyroscopes.

3.9 PERFORMANCE DISCUSSION

In order to fully realize the potential of BAW gyroscopes as attractive replacements to current gyroscopes, the overall performance of these devices should be precisely understood. Toward this end, the design and performance parameters for a typical BAW gyroscope are evaluated using the derived analytical and summarized in Table 3-2.

As shown in Table 3-2, the sensitivity of a device implemented in (100) SCS is ~4.5 times smaller than the similar device implemented in (111) SCS. This is mainly due to the higher angular gain A_g of (111) devices compared to (100) devices (~1.9×). It can also be partially attributed to the ~1.5times higher frequencies of secondary elliptic modes than the primary elliptic modes. In addition, the maximum displacement ($U_{r=R}$) in (111) SCS is ~1.6times larger than in (100) SCS. Using the sensing mechanism (Fig. 6)

makes the amplified sensitivity independent of the resonance frequency. This results in amplified sensitivity in a (100) SCS device to be only 3× smaller than a (111) SCS device.

Table 3-2: Analytical estimation of performance parameters in BAW disk gyroscopes.

Material/mode	**(111) SCS Secondary elliptic mode (*m=2*)**	**(100) SCS Secondary elliptic mode (*m=3*)**
Disk diameter (μm)	800	800
Disk thickness (μm)	40	40
Electrode length (Le) (μm)	175	175
Capacitive gap (nm)	200	200
Drive amplitude (nm)	20	20
Effective quality factor (Q)	100,000	100,000
Operating frequency (MHz)	5.01	7.52
The maximum normalized displacement at r=R (U_R)	1.5105	0.9430
Effective mass coefficient	0.4413	0.3137
Angular gain (A_g)	0.4584	0.2314
Polarization voltage (V)	10	10
I_{noise} (pA/√Hz)	2.5	2.5
Frequency bandwidth (Hz)	25	38
Sensitivity (aF/°/sec)	4.76	1.06
MNEΩ (°/sec/√Hz)	0.00077	0.00099
ENEΩ (°/sec/√Hz)	0.0017	0.0053
Total noise (°/sec/√Hz)	0.0018	0.0054

Although (111) SCS gyroscopes can offer higher A_g and $U_{r=R}$, we are not accounting for factors that will improve the sensitivity of (100) SCS devices. For instance, in Table II, it is assumed the same electrode length for both devices in (100) and (111) SCS substrates. However, the electrodes for (111) SCS need to be repeated every 22.5° instead of 30° in

(100) SCS, implying that the electrodes are 1.4× smaller in length in (111) SCS than (100) SCS. In addition, all the design performance parameters calculated here are based on using a single sense electrode. If a fully differential architecture is employed, the sensitivity would be increased significantly. For a (111) SCS device operating in its primary elliptic modes, the performance can be improved by 4×; however this can be improved by 6× in a (100) SCS device operating in its secondary elliptic modes. This is due to available number of anti-node lines for each elliptic mode. Considering the above, the sensitivity and the resolution of (100) SCS BAW gyroscopes can be improved by an additional 3×, offering similar performance to BAW gyroscopes in (111) SCS.

Furthermore, total resolution relies on both Brownian noise and electronic noise evenly. The mechanical noise floor in BAW gyroscopes is improved by increasing the resonant frequency by 2 to 3 orders of magnitude (to 2-8 MHz) and by utilizing stiff bulk acoustic modes which substantially increase and thermally stabilize the Q. As a result, Brownian noise is not a constraint on the resolution in high frequency BAW gyroscopes, as shown in Table 3-2, and electronic noise tends to be what limits the sensors. The electronic noise depends linearly on electronic input-referred noise (I_{noise}) and inversely on the gap aspect ratio (AR) and the matched-mode Q. The electronic noise can be improved by

1) developing a high gap aspect-ratio (AR>200) process,
2) designing a high matched-mode quality factor (Q>100,000) structure, and
3) utilizing an ultra low noise amplifier (I_n<1pA/√Hz).

The above parameters can play a significant role in lowering the electronic noise and subsequently improving the resolutions in BAW gyroscopes. The performance parameters are measured in Chapter 5 and compared with the analytical values.

3.10 THERMOELASTIC DAMPING

Thermoelastic damping (TED) is a dominant loss mechanism in flexural-based gyroscopes, introducing highly temperature-dependent performance deterioration that circumscribes these sensitive devices' thermal stability [90-92]. Thus, designing micromachined gyroscopes such that their *Q*s are not immediately affected by TED is always desirable. To do this, the effect of thermoelastic damping (TED) is studied for solid and perforated disk structures operating at their primary and secondary elliptic modes as well as breathing modes.

3.10.1 THERMOELASTICITY THEORY

As a starting point, it is noted that the total *Q* of a resonating structure [93] generally can be expressed as:

$$Q = \left[\frac{1}{Q_{Air}} + \frac{1}{Q_{TED}} + \frac{1}{Q_{Support}} + \frac{1}{Q_{Other}} \right]^{-1} \tag{3-68}$$

Where Q_{Air}^{-1}, Q_{TED}^{-1}, $Q_{Support}^{-1}$ and Q_{other}^{-1} are, respectively, defined as air damping losses, thermoelastic damping losses, the losses through support and "other" losses not included in the preceding terms. The latter might originate from, for example, surface roughness or intrinsic material energy dissipation. As one can expect, each of the *Qs* on the right hand side of (3-63) has less impact upon the overall *Q* when it is larger. This implies that

the total Q would be less dominated by Q_{TED} if the Q_{TED} value was very large compared to the rest of the Qs.

To determine the Q_{TED} for a disk operating in BAW modes, the coupled deformation and temperature PDEs were estimated and solved for their eigenvalues [94]. Consequently, for each resonant mode, Q_{TED} was evaluated as the ratio of the imaginary part to the real part of the corresponding eigenvalue. The general coupled deformation and temperature partial deferential equations are stated in (3-69):

$$\begin{aligned} &\rho\frac{\partial^2\vec{u}}{\partial t^2}-\mu\nabla^2\vec{u}-(\mu+\lambda)\nabla(\nabla\vec{u})+\frac{\alpha E}{(1-2\nu)}(\nabla T)=0 \\ &k\nabla^2 T-c\rho\frac{\partial T}{\partial t}-\frac{\alpha E T_{init}}{(1-2\nu)}\nabla\frac{\partial\vec{u}}{\partial T}=0 \end{aligned} \tag{3-69}$$

Then, the coupled deformation and temperature PDEs are normalized and simplified in (3-71) from [95]:

$$\begin{aligned} &\frac{\partial^2\bar{u}}{\partial\tau^2}-\frac{\partial^2\bar{u}}{\partial\phi^2}-\eta\frac{\partial\bar{T}}{\partial\phi}=0 \\ &\frac{\partial^2\bar{T}}{\partial\phi^2}-\frac{\partial\bar{T}}{\partial\tau}+\eta\frac{\partial}{\partial\phi}\frac{\partial\bar{u}}{\partial\tau}=0 \end{aligned} \tag{3-70}$$

where η, $\bar{u}$, $\bar{T}$, τ and ϕ are, respectively, the thermoelastic coefficient, the dimensionless displacement, dimensionless temperature, normalized time and normalized coordinates. These terms are defined as:

$$\bar{u} = \frac{u}{u_0}, \bar{T} = \frac{T}{T_0} \tag{3-71}$$

where u and T are the displacement and temperature vectors as a function of position and time. Also, u_0 *and* T_0 are related to each other as the coupling coefficient term:

$$\frac{u_0}{T_0} = \frac{\kappa}{\mu\sqrt{cT_{init}}} \tag{3-72}$$

in which κ, c, T_{init} and μ are respectively the thermal conductivity, the specific heat capacity, the room temperature and the Lame coefficient. The Lame coefficient can be expressed in terms of Young's modulus (E) and Poisson ratio (υ) as $E/2(1+\upsilon)$. The scale factors for the normalized position and time coordinates can be stated as:

$$\phi = xk \quad \text{where} \quad k = \frac{c}{\kappa}\sqrt{\rho\mu} \tag{3-73}$$

$$\tau = t\omega_0 \quad \text{where} \quad \omega_0 = \frac{c\mu}{\kappa} \tag{3-74}$$

where ρ and ω_0 are respectively the mass density and the natural angular frequency. The same scale factor is used for y and z position directions. And finally the thermoelastic coefficient (η) is defined as below [95]:

$$\eta = \frac{-\alpha E}{(1-2\nu)}\sqrt{\frac{T_{init}}{c\rho\mu}} \tag{3-75}$$

where α is the thermal expansion coefficient and the other terms are as previously defined. Afterwards, the dimensionless displacement in any direction ($\bar{u}$) can be written in terms of dimensionless position (ϕ, φ, ψ) and dimensionless time (τ).

At this point, it can be assumed that both $\bar{u}$ and $\overline{T}$ are separable in terms of time and position:

$$\begin{aligned} \overline{u}(\phi,\varphi,\psi,\tau) &= \overline{u}(\phi,\varphi,\psi) f(\tau) \\ \overline{T}(\phi,\varphi,\psi,\tau) &= \overline{T}(\phi,\varphi,\psi) f(\tau) \end{aligned} \tag{3-76}$$

where $f(\tau) = e^{\lambda\tau}$ in which λ is the eignvalue.

The goal is to develop a system of thermoelastic equations and solve for eignvalues (λ) of each resonant mode. Given the real and imaginary part of eignvalues, the Q_{TED} can be determined from (3-77).

$$Q_{TED} = \frac{\mathrm{Im}\{\lambda\}}{-2\,\mathrm{Re}\{\lambda\}} \tag{3-77}$$

Since exact, closed-form solutions to thermoelastic equations are only available for simple geometries (*i.e.* flexural beams) [96, 97], finite element analysis (3D multiphysics mode in COMSOL) is used to model Q_{TED} in disk gyroscopes operating in their bulk acoustic modes.

3.10.2 FINITE ELEMENT MODELING

The scaled thermoelastic equations were solved in COMSOL multiphysics, yielding both eigenvalues and eigenvectors. The general form of COMSOL eigenvalue solver is as following:

$$-\nabla.(c_1\nabla u + \alpha_1 u - \gamma_1) + au + \beta\nabla u = d_a \lambda u \tag{3-78}$$

Where c_1, α_1, γ_1, a, β and d_a are all 7×7 matrices of coefficients and λ is the eigenvalue to be solved for; u is the displacement matrix that contains the eigenvectors for displacement, velocity and temperature of each node in the model geometry. c_1 solely depends on the elastic terms, *i.e.* Young's modulus (E) and Poission ratio (υ). And a and d_a are matrices with constant values. These matrices along with their values for BAW disk structures are defined in detail in Appendix A. On the other hand, the thermoelastic coefficients appeared in the α_1 and β matrices. These are defined in terms of η as expressed in (3-75) and these matrices are also detailed in Appendix A. Given the material properties of BAW gyroscopes, these matrices components can be evaluated and entered into the COMSOL multiphysics. Then (3-78) can be solved for their eignvalues of the chosen modes.

It is worth noting that the real part (damping) of the complex eigenvalues is much smaller than the imaginary part (resonant frequency), due to the smaller effect of damping compared to elastic oscillation in a low-loss material like SCS. Thus, as a matter of practical implementation, the imaginary part is swapped with the real part in the COMSOL formulation to make finding the eigenvalues easier [95].

These equations are first solved for disk structures resonating in their primary and secondary elliptic modes. The steady-state temperature distributions and Q_{TED} for primary and secondary elliptic modes in an 800μm diameter solid disk structure are shown in Figure 3-9.

As one can observe, the Q_{TED} in these modes for an 800μm diameter disk is very large and it has the value in the range of low hundreds of millions. This implies that in a solid disk operating in its primary and secondary elliptic modes, the Q_{TED}s can respectively contribute only ~0.027ppm and 0.006ppm on the total Q.

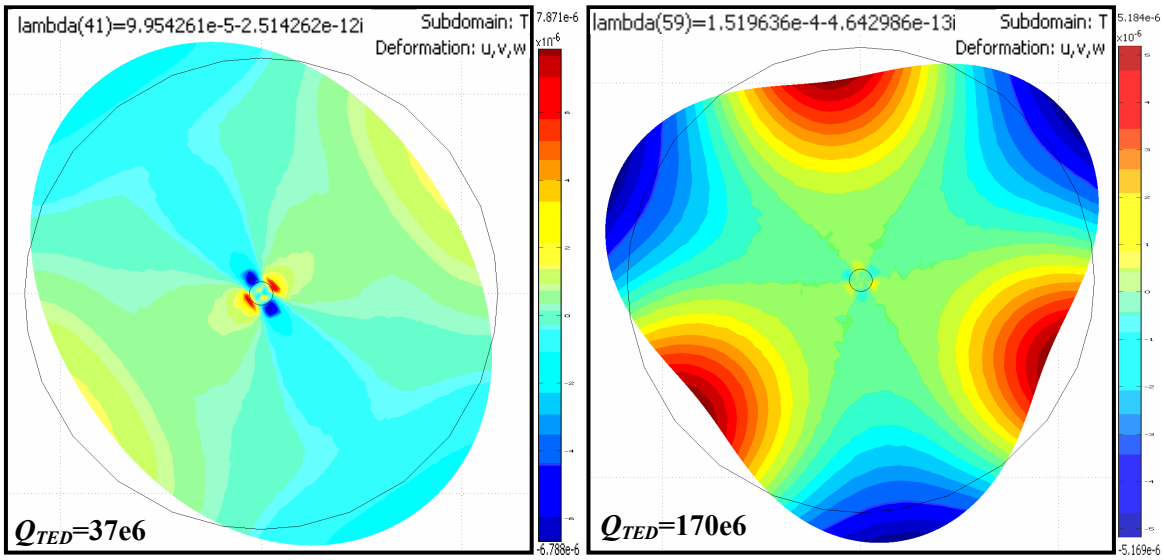

(a) (b)

Figure 3-9: Steady-state vibration-induced temperature distribution in an 800μm diameter solid disk for (a) primary elliptic mode and (b) secondary elliptic mode, simulated in COMSOL.

Furthermore, thermoelastic losses are modeled for a variety of disk geometries. Figure 3-10 shows that decreasing the disk diameter lowers Q_{TED} in BAW modes. This clearly indicates that the total Q becomes more reliant on the Q_{TED} when the disk dimensions are reduced, driving the resonant frequencies higher. Interestingly, the rate of the decrease in

Q_{TED} for primary elliptic mode is less than the Q_{TED} for secondary elliptic modes. This may be simply due to the higher frequency operation of secondary elliptic modes.

In addition, the effect of varying the disk thickness is investigated. The thickness was set to a variety of diameters, ranging from 0.1× the disk diameter (called the full-thickness case) to 0.1× the disk radius (known as the half-thickness case). The thicknesses investigated were confined to this range to ensure that the BAW modes were not distorted due to improper aspect ratios. Due to the in-plane motion of elliptic modes, it was expected that TED would not vary with thickness. As shown in Figure 3-11, the Q_{TED} in solid disks operating at their secondary elliptic is the same for both full and half thickness cases. However, in disks with diameters larger than 100 μm, simulations showed that Q_{TED} for primary elliptic modes decreases significantly when the thickness is halved, Figure 3-11.

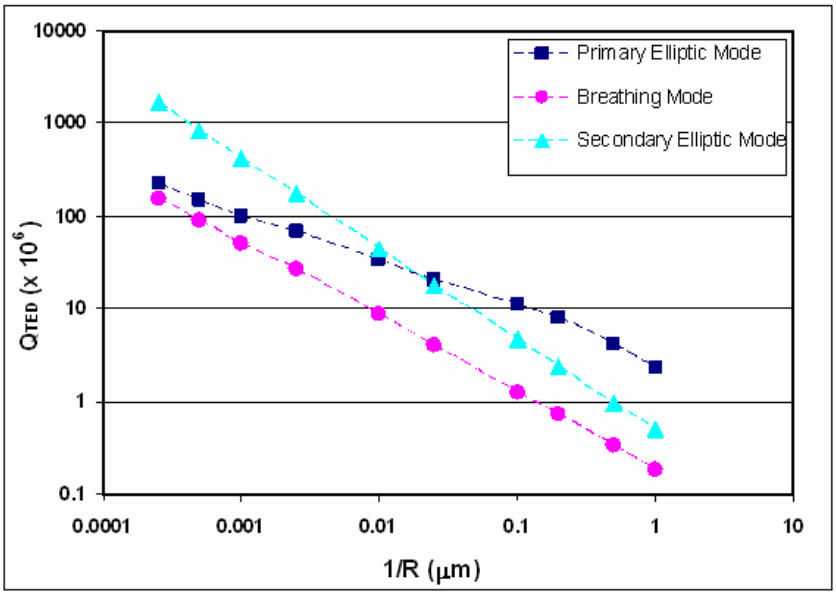

Figure 3-10: The estimated Q_{TED} for solid disk structures in the range of 500kHz to 2GHz for primary and secondary elliptic modes as well as breathing mode, simulated in COMSOL.

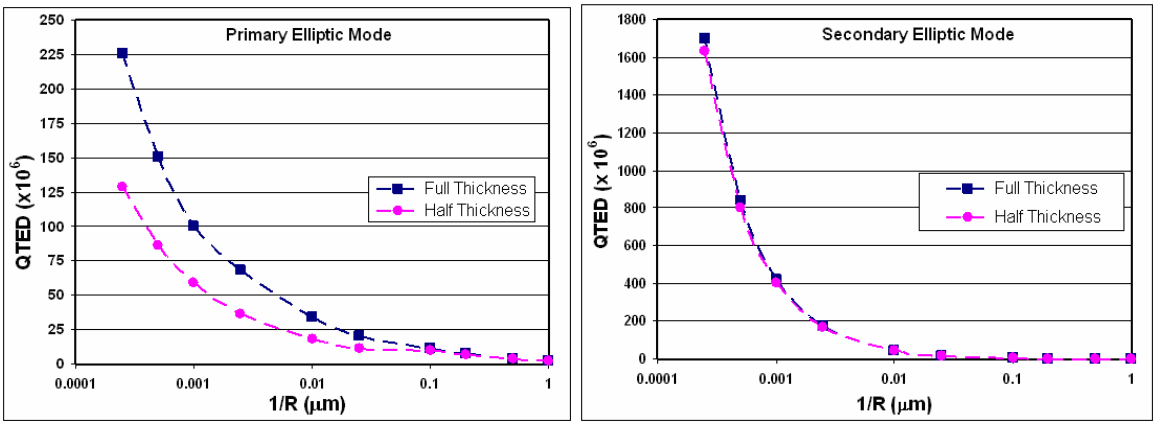

Figure 3-11: The effect of disk thickness on Q_{TED} in solid disks operating at their primary and secondary elliptic modes.

Next, symmetrical release holes are added to the disk, as dictated by fabrication needs (Chapter 4). Including perforations in the disk introduces localized dynamic strain concentrations, which induce temperature gradients and result in additional TED losses. In order to study the effect of release hole sizes on Q_{TED}, 800μm diameter disks with a variety of holes sizes were modeled in COMSOL. In each model, the perforation sizes are uniform across the disk and equally spaced. As shown in Figure 3-12, Q_{TED} drops substantially for perforated disks with large release holes. This establishes that optimization of Q_{TED} for perforated disks favors very small release holes (<8μm). Also, according to the simulation results, beyond a certain release hole size, the rate of decrease in Q_{TED} becomes less pronounced, perhaps because the operating frequency also begins to decrease. The lower operating frequency can neutralize the effect of sharp stress distributions on Q_{TED} in these devices. Also, it was observed that for disks without any perforations, the Q_{TED} of secondary elliptic mode is ~4.5× larger than the primary elliptic mode. However, when perforations are introduced, the Q_{TED} of the secondary elliptic mode reduces to that of the primary elliptic modes. Furthermore, due to the common

axisymmetry between the breathing mode and the release holes pattern, the Q_{TED} in this mode is much higher than elliptic modes with perforations present. Although breathing modes are not suitable for disk gyroscopes, they could be utilized for disk resonators.

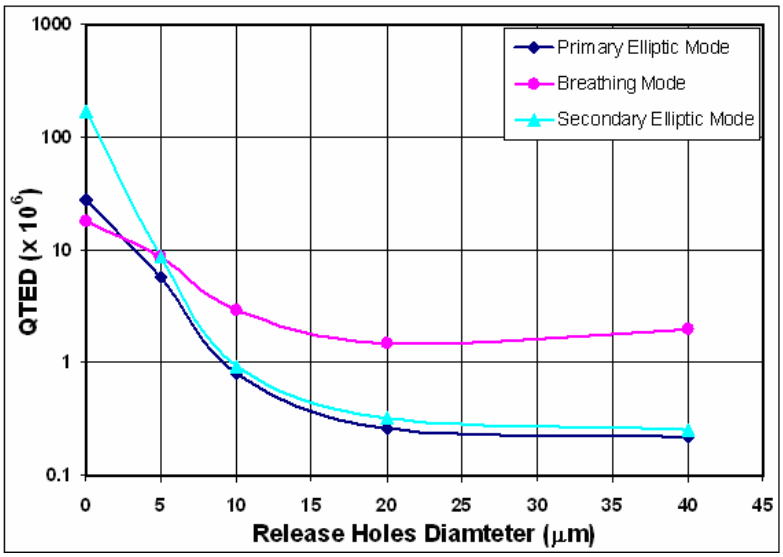

Figure 3-12: The effect of release holes' sizes in Q_{TED} for primary and secondary elliptic modes as well as breathing mode in 800μm diameter disks, simulated in COMSOL.

The steady-state temperature distributions and Q_{TED} for primary and secondary elliptic modes in 800μm diameter disks with differing release holes designs are shown in Figure 3-13. As it can be observed, the Q_{TED} in disks with 5μm holes is ~50times larger than the Q_{TED} in disks with non-uniform holes.

Additionally, Q_{TED} in both solid and perforated disks are modeled over a temperature range of -5°C to 55°C in COMSOL. Figure 3-14 shows that the thermoelastic damping mechanism is stronger at elevated temperature. In both solid and perforated 800μm diameter disk structures, Q_{TED} was found to drop by ~27% over the 60°C temperature range. It is worth noting that the variation of the thermophysical properties of single crystal silicon with temperature is included in this model, taken from the data in [98, 99].

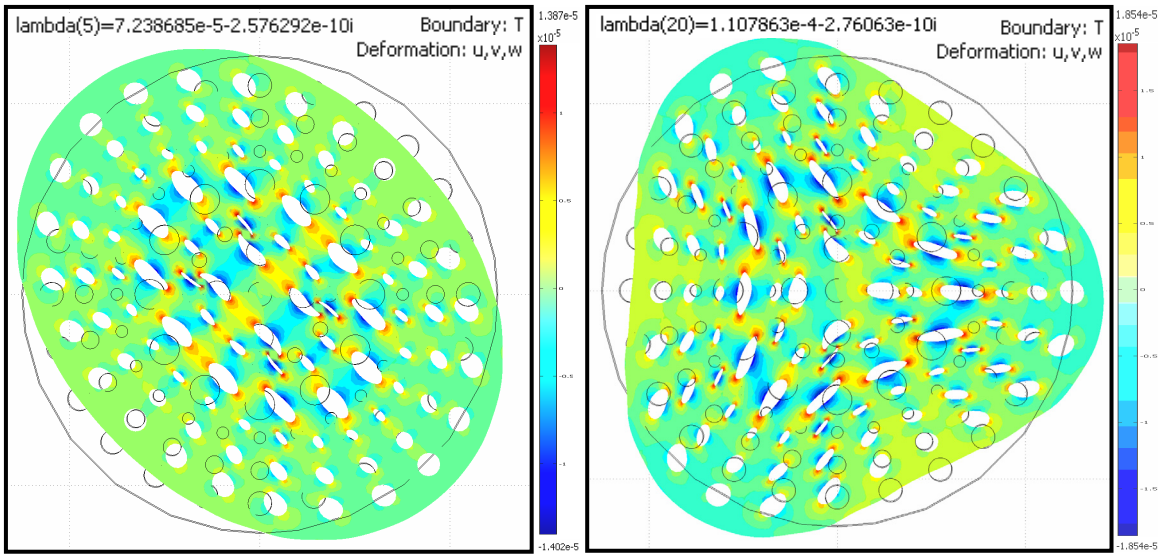

(a)

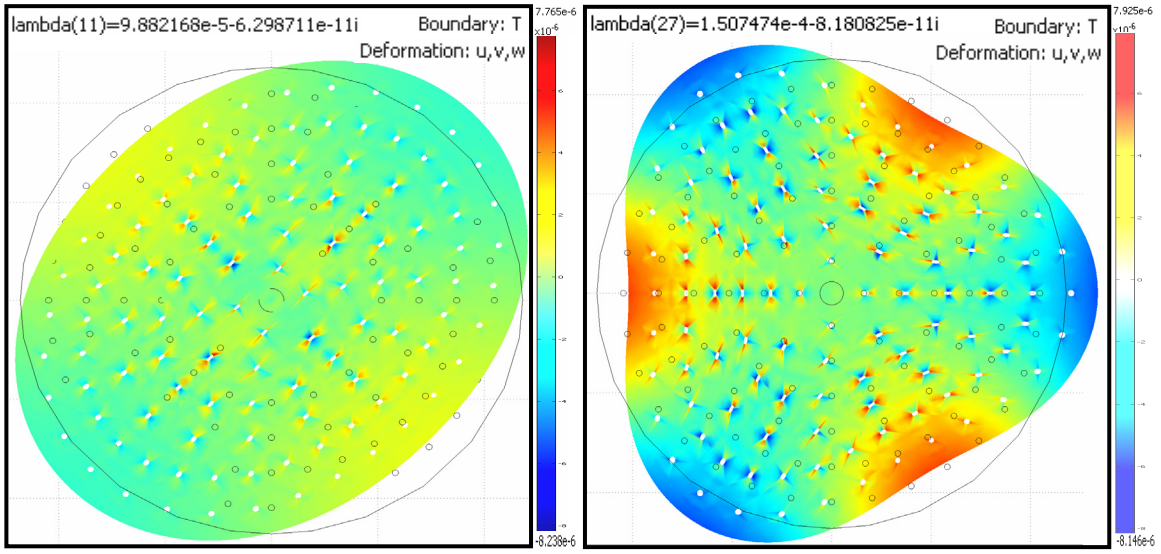

(b)

Figure 3-13: Steady-state vibration-induced temperature distribution in 800µm diameter disks with (a) non-uniform holes, (b) uniform 10µm holes operating in primary and secondary elliptic modes, simulated in COMSOL.

In order to identify the effect of Q_{TED} on the total Q in these devices, the measured total Q can be characterized over the same temperature range of 60°C, which is discussed in Chapter 5. If the percentage of the measured total Q reduction for this temperature range

is smaller than the Q_{TED} reduction, this demonstrates that the Q in these devices is not mainly limited to Q_{TED}.

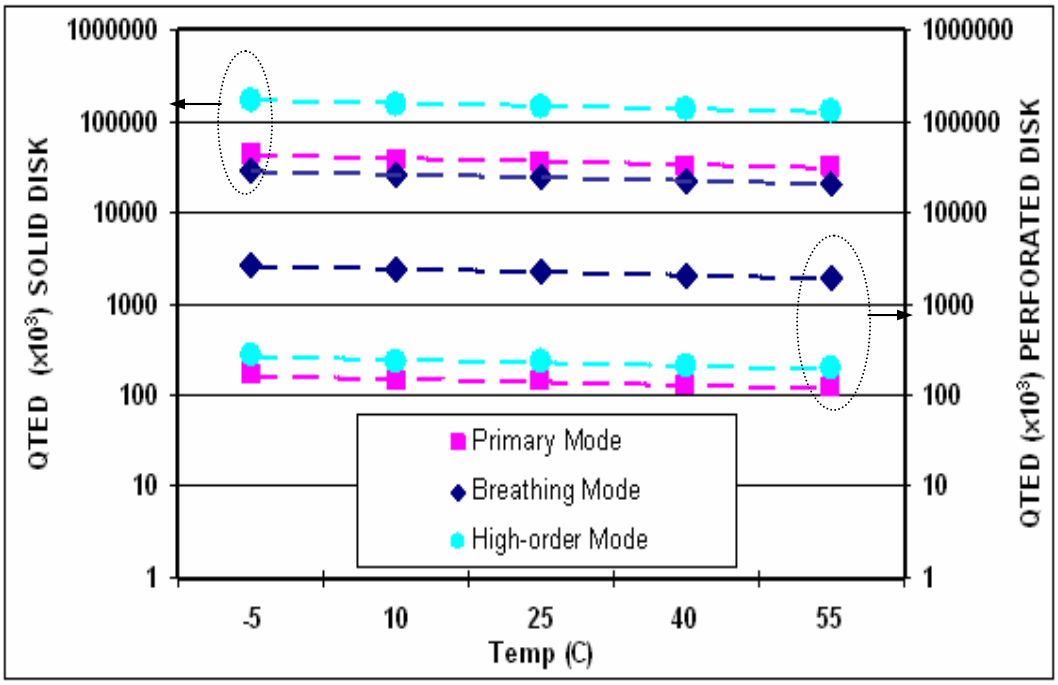

Figure 3-14: The temperature characterization of Q_{TED} over a temperature range of -5°C to 55°C in 800μm diameter solid disk, showing that Q_{TED} is dropped 27% over the 60°C temperature range.

The conclusions drawn in this section can serve as guidelines for future disk designs where the temperature dependence of a Q_{TED}-dominated resonance is to be avoided. For solid disks, the ultra-high Q_{TED} suggests that TED may never be a concern. However, for perforated disks, thermoelastic multiphysics simulation identifies that size of release holes effects on the Q_{TED} and lower Q_{TED} observed for larger release holes. As a result, Q_{TED} is very large for small perforated disk gyroscopes operating in their elliptic modes, and thus TED is not a dominating loss mechanism in these devices.

CHAPTER 4

MICRO-FABRICATION PROCESS

4.1 FABRICATION FEATURES

4.1.1 MATERIAL SELECTION

It is well-known that single crystal silicon (SCS) is inherently a low mechanical loss material compared to piezoelectrics or metals. In resonating structures, this can offer very high quality factor (Q), which is always desired in vibratory gyroscopes to enhance scale factor and resolution. As discussed in Chapter 3, due to MHz frequency of BAW modes high matched-mode Q is a key to achieve high scale factor in BAW gyroscopes. Also, a high Q can assist the high frequency in BAW gyroscopes to reduce the noise floor without the need for large excitation amplitude, which lowers the operating voltages significantly.

Capacitive coupling can be used as a transduction mechanism to excite silicon structures. To excite the disk in its stiffness BAW modes large electrostatic forces are required, which in turn necessitates large capacitive coupling. High gap-aspect ratio and very small capacitive gaps can provide large capacitive coupling.

4.1.2 HIGH ASPECT RATIO AND NARROW CAPACITIVE GAP

Scale factor and resolution in BAW gyroscopes are linearly proportional to the gap aspect ratio, as derived in Chapter 3. This implies that a high gap aspect ratio can considerably improve the performance parameters in these devices. Also, high gap-aspect ratio is

needed to provide large enough electrostatic forces to drive the disk at MHz frequencies in its stiff BAW modes.

One well-known approach to high gap-aspect ratio is etching high aspect-ratio trenches, using bulk micromachining techniques [100]. However, silicon etching equipment, such as the STS ICP, can only achieve trench aspect ratios of ~30/1 [101]. It is always better to have a higher gap-aspect ratio and not limited by the fabrication equipments. To meet this demand, a high-aspect ratio poly- and single crystalline silicon process (HARPSS) was developed by Farrokh Ayazi [102] and later modified by Siavash Pourkamali [103]. In this process, a thin sacrificial LPCVD oxide (SACOX) is deposited inside silicon trenches. The trenches are refilled with LPCVD polysilicon to form the electrodes, and the SACOX is etched later to form a capacitive gap. This process enables a gap-aspect ratio limited only by silicon oxide to silicon etch selectivity (~150/1). In this dissertation, the revised HARPSS process is utilized and further optimized for center-supported BAW disk gyroscopes in thick silicon on insulator (SOI) substrates [104]. A gap aspect ratio of 200/1, ~7× higher than conventional etching equipment, is targeted for the BAW gyroscopes in this work.

Besides high gap aspect ratios, very small capacitive gaps, in the range of a few hundred nanometers, are required to provide large electrostatic forces in BAW gyroscopes. If a small enough capacitive gap is not provided, the disk's resonant modes may still be excited, but only with very large operating voltages (V_p>50V). Also, using very small capacitive gaps provides for very small vibration amplitudes (in the range of a few tenth of nm). This further lowers operating voltages (V_p<5V) and simultaneously improves the shock tolerance of these devices.

On the other hand, matched-mode operation is always desired in micromachined gyroscopes to enhance the performance parameters. In capacitive gyroscopes, electrostatic tuning is a well-established method for achieving this. In this method, DC voltages adjust the electrical stiffness, and consequently the resonant frequency, of each mode, until the two modes' frequencies match. For BAW gyroscopes, the electrical stiffness for both drive and sense mode were derived and expressed in Chapter 3. The electrical stiffness of each degenerative mode for a specific device design depends solely on the applied DC voltages. However, the optimization of the device design parameters can assist by lowering the required DC tuning voltages. Toward this end, the relationship between the frequency and tuning voltages, derived in Chapter 3, is simplified and presented here.

$$\left.\frac{\partial f}{\partial V}\right)_{tuning} = \frac{\varepsilon_0 {U_r}^2 L_e}{4 f_0 \rho R^2 C_{effec-mass} (\pi d_0)^3} V_{tuning} \tag{4-1}$$

Where L_e, R and d_0 are respectively electrode length, disk radius and the capacitive gaps and are the design parameters. And the constants ε_0, U_r, $C_{effec\text{-}mass}$ are respectively the dielectric constant, normalized maximum displacement and the effective mass coefficient, all detailed in Chapter 3. Also, V_{tuning} and f_0 are respectively the tuning voltage and the operating frequency.

As can be observed in (4-1), frequency tuning is linearly proportional to the tuning voltage, the electrode length and the square of the normalized maximum displacement. However, it is inversely proportional to the operating frequency, the square of the disk radius and the cube of the capacitive gap. This implies that very large tuning voltages would be required if the small gaps are not provided for tuning electrodes. Furthermore, it

is evident from (4-1) that the tuning voltages not affected by the disk thickness. This clearly indicates that a fabrication process offering a high gap aspect ratio but not also offering small gaps would not be sufficient for BAW gyroscopes' tuning needs. As a result, these devices are designed to be implemented on thick SOI substrates (30-60μm) with small capacitive gap of typically ~200nm. It would be preferable to further reduce the capacitive gaps, but contemporary fabrication limits circumscribe the achievable gap aspect ratio.

4.1.3 CENTER SUPPORT

The total quality factor in a resonating structure can be determined from [105] as stated in:

$$Q = \left[\frac{1}{Q_{Air}} + \frac{1}{Q_{TED}} + \frac{1}{Q_{Support}} + \frac{1}{Q_{Surface}} + \frac{1}{Q_{Intrinsic}} + \frac{1}{Q_{Other}} \right]^{-1} \tag{4-2}$$

As it was discussed in Chapter 3, disk gyroscopes operating in their BAW modes are not mainly limited by thermoelastic damping. In addition, the air damping is less significant in these devices than in low frequency gyroscopes, due to the high resonant frequencies of BAW modes. This implies that the quality factor of these devices should be mainly dependent on their support losses rather, than on TED or air damping, as is the case for low-frequency gyroscopes.

As a result, it is desirable to have minimum support loss to achieve very high quality factor. Support losses depend on the support size, the support material and the location of the support [75]. With smaller support size, less energy is dissipated through the support region while the disk is vibrating. Also, it is preferable to have higher-strength material

for the disk than for the support material ($E_{disk} > E_{support}$). This serves to confine more energy in the resonating structure, transferring less into the support in each vibration cycle. Furthermore, the support should be placed at vibration nodes to minimize the energy coupled into the support. In a disk structure vibrating at its elliptic modes, there are 6 node lines for each degenerative mode. However, the vibration node lines of each degenerative mode coincide with antinode lines of the other degenerative mode. This means that placing support at one mode's node line would cripple the other degenerative mode, drastically lowering the Q of that mode. On the other hand, the centre of the disk is always a node point while the disk operates at any elliptic modes. Since both degenerative modes need to be utilized in BAW gyroscopes, the support clearly must be placed at the center of the disk. It is worth noting that the center support diameter should be small enough in relation to the disk diameter to act as a point. Larger center supports add additional symmetrical losses on both degenerative modes.

To meet all the above requirements for low loss support, the BAW disk gyroscope is supported at the center by a very small island of the buried oxide layer (BOX) in the SOI substrate. The symmetry of the perforated disk guarantees that the support is self-aligned to center of the disk structure by the BOX etch step. The center post diameter is designed to be at most one twentieth of the disk diameter to minimize any losses through support [75, 104]. Also, doped polysilicon traces attached to the center of the disk, to which they are self-aligned, provide DC bias voltage to the disk along with mechanical support from the top side.

4.1.4 PERFORATIONS

Perforations, as designed in Chapter 3, are added to the disk to eliminate the need for backside etching and further backside packaging. All release holes need to be self-aligned with the resonating structures to avoid any asymmetry issues, which can introduce some frequency separation and non-symmetric losses. This is achieved using a thick silicon oxide mask (initial oxide) to define the resonating disk structure and the perforations as well as the center for poly trace connection in the disk, simultaneously. The silicon oxide mask has a high selectivity to silicon. This is necessary to withstand not only the etching of release holes in the silicon substrate but also the etching of the polysilicon inside the trenches and release holes. In addition, it is critical to ensure that the distribution of perforations allows releasing the disk conformally. Finally, the distance between the release holes at the center of the disk needs be large enough to ensure the buried oxide at the center of the disk survives the release etch.

4.2 FABRICATION PROCESS

The BAW gyroscopes were fabricated in thick SOI wafers (30-50μm thick) using a modified HARPSS process [73]. A process flow is shown in Figure 4-1. The process starts with growth of a 2μm thick silicon oxide on the silicon substrate (wet oxidation at 1000°C). This thick silicon oxide was patterned to define the resonating perforated disk structures and act as a mask for proceeding steps. The location of the center support region is also determined by this step, ensuring that it is self-aligned with the disk. Then, deep trenches are etched through the SOI device layer at the release hole locations and around the disk, the latter isolating the resonating structure. It is worth noting that the

Bosch process is employed to etch the trenches in SOI substrate and that extensive characterization and modification of the recipe parameters was necessary to optimize the trench profiles for smooth sidewalls and straight profiles with minimum scalloping and footing, as detailed in the next section.

Next, a thin layer of sacrificial LPCVD silicon oxide (SACOX) is grown (dry-oxidation at 950°C or LPCVD oxide at 825°C) and boron doped (at 1050°C, 1hour). This layer will form the capacitive gaps later. After this, the trenches are refilled with LPCVD polysilicon (at 588°C and 250mTorr with 100SCCM SiH_4) and boron doped (resistivity <0.1ohm-cm), creating the electrodes inside the trenches. The LPCVD polysilicon is then etched from the surface, uncovering the SACOX. The SACOX is patterned and removed from the surface everywhere except around the disk edge and perforation edges. The remaining SACOX protects the edges of the resonating structure during poly etching inside the trenches, which is the next step. Then, the second LPCVD polysilicon layer is deposited, boron doped, and annealed (at 1050°C, 2hours). Polysilicon is patterned on the surface to define the pads as well as the poly traces, which are self-aligned to the center of the disk. A Bosch process is employed and characterized to etch polysilicon inside the trenches as well as parts of the silicon substrate to define the electrodes and isolate each electrode and its pad from the rest. At the same step, polysilicon and silicon are removed inside the release holes. Finally, the device is released in hydrofluoric acid (HF). A small island of buried oxide layer (BOX) within the SOI substrate is to be left by this step to act as a center support, calling for careful timing of HF release. In addition, the symmetry of the structure guarantees that the support is self-aligned to the center of the disk structure during the BOX etch step. The polysilicon trace on the surface is required to provide DC

bias to the disk. Also, each poly electrode partially extends out on the disk structure to provide an out-of-plane shock stop for the device. The described process is compatible with Analog Device's SOIMEMS process [106, 107] and can be integrated with CMOS electronics by adding some pre- and post-CMOS fabrication steps.

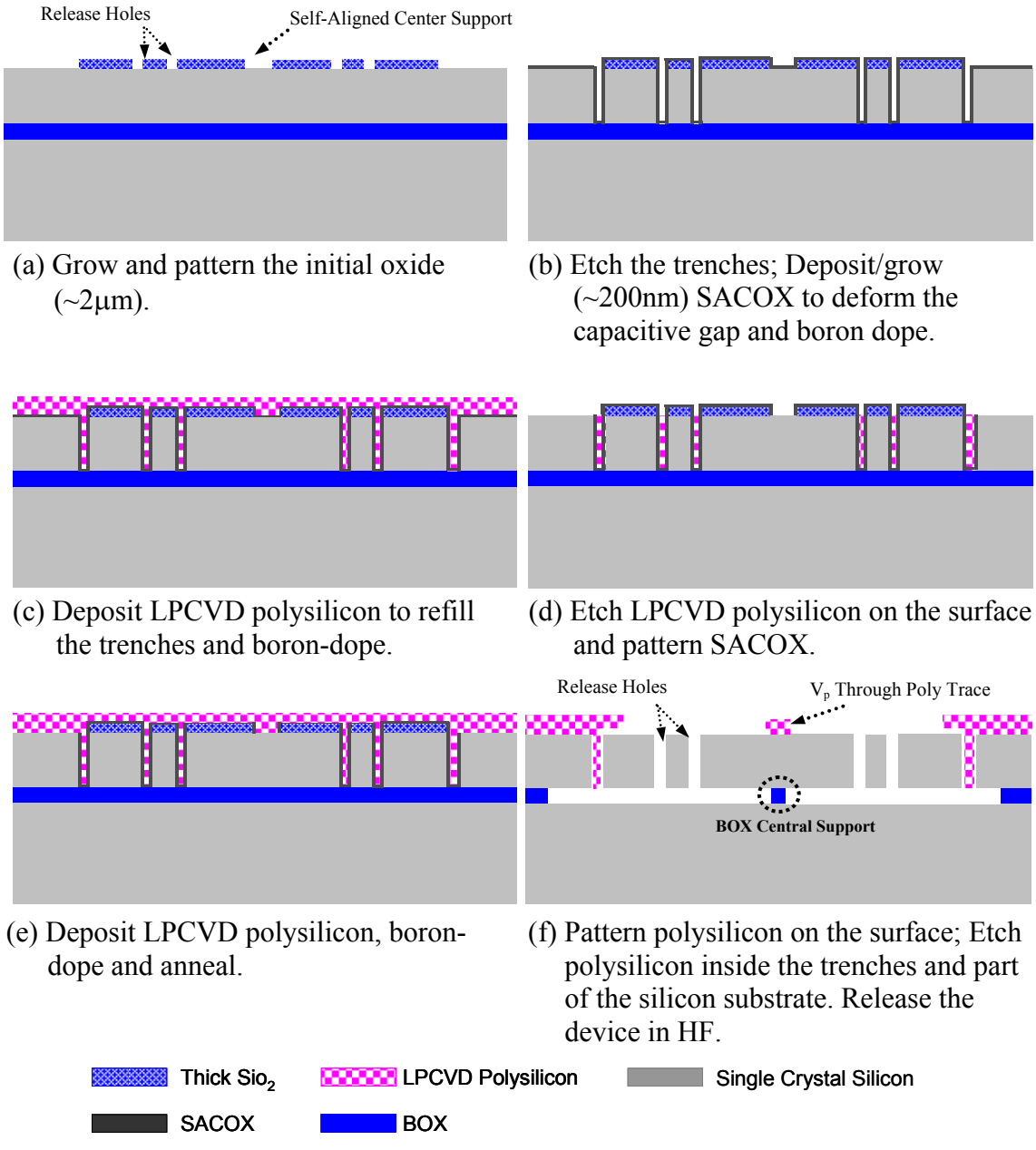

(a) Grow and pattern the initial oxide (~2μm).

(b) Etch the trenches; Deposit/grow (~200nm) SACOX to deform the capacitive gap and boron dope.

(c) Deposit LPCVD polysilicon to refill the trenches and boron-dope.

(d) Etch LPCVD polysilicon on the surface and pattern SACOX.

(e) Deposit LPCVD polysilicon, boron-dope and anneal.

(f) Pattern polysilicon on the surface; Etch polysilicon inside the trenches and part of the silicon substrate. Release the device in HF.

Figure 4-1: The process flow of center-supported silicon BAW disk gyroscopes on SOI wafer.

4.3 FABRICATION PROCESS PARAMETERS

In the aforementioned HARPSS fabrication process, silicon oxide etching, trench etching in SOI substrates and poly etching inside the trenches are the main fabrication steps. A summary of fabrication parameters for these steps are discussed in this section.

4.3.1 SILICON OXIDE ETCHING PARAMETERS

Silicon oxide etching was carried out in the Plasma-Therm-ICP tool in MiRC Cleanroom. The Plasma-Therm ICP offers higher selectivity and better anisotropic profile for oxide etching in comparison to Plasma-Therm RIE. Also, the etch rate is ~3times faster in Plasma-Therm ICP. The appropriate recipe parameters for oxide etching are summarized in Table 4-1. It must be noted that the process parameters were frequently calibrated to obtain the desired oxide profile and sidewall roughness.

Table 4-1: Process parameters for silicon oxide etching in Plasma-Therm ICP.

Parameters	**Values**
Gases	C_4F_6: 20sccm
	CF_4: 40sccm
	O_2: 3sccm
	Ar: 15sccm
Pressure	5mTorr
Power	RF: 300W ICP: 250W
Etch rate	~1100Å/min (Thermal oxide)

Positive photoresist (SC-1827 or SPR220) is used as a mask. The mask selectivity is a function of the process parameters which was found to be ~ 2/1 for this recipe. A SEM view of patterned 2μm thick silicon oxide is shown in Figure 4-2 using the parameters in Table 4-1. As it can be observed, the profile is still tapered and this can be further improved by using an advanced Trion-ICP tools. This provides better anisotropic silicon oxide profile with a faster each rate.

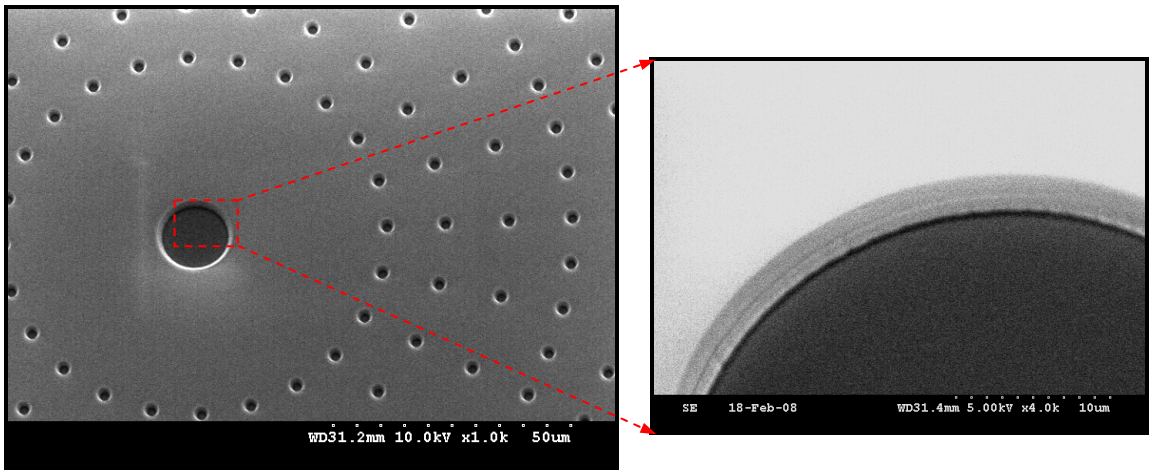

Figure 4-2: A SEM view of a silicon oxide etching profile.

4.3.2 SILICON ETCHING PARAMETERS

Trench etching is the most important fabrication step in the revised HARPSS process flow. A Bosch process is utilized and modified to etch the trenches in SOI substrates. The trench profile should be as straight as possible with the minimum bow and scalloping. This is needed to eliminate a large void when the trenches are refilled with LPCVD polysilicon. Also, re-entrance trench profile (*i.e.*, wider at the bottom) creates issues with the poly etching inside the trenches at the bottom. As it was explained, the trenches are etched in the device layer on SOI substrate in which the buried oxide acts as a stopping layer. Due to the existence of oxide at the bottom of the trenches, footing would be an issue at the bottom of trenches. To avoid this, a low frequency module (380 kHz) should be employed. STS-ICP is the only available tool in MIRC Cleanroom that can offer low frequency module for silicon etching using Bosch process. Numerous trench etching characterizations were performed and the trench profiles were monitored under Hitachi SEM. After each characterization, the recipe parameters were modified to improve the trench profiles. The recipe modification steps continue to achieve the desired trench

profiles. Table 4-2 summarizes the process parameter for etching silicon in SOI substrates as a starting point. It is worth noting that the process parameters are frequently calibrated to obtain the desired trench profile and sidewall roughness. This recipe offers the selectivity of (75/1) for (Positive-Resist/Si) and the selectivity of (150/1) for (Sio_2/Si) in the STS-ICP available in MIRC clreanroom.

Table 4-2: Process parameters for silicon etching in STS-ICP (starting point).

Parameter	**Etching Cycle**	**Passivation Cycle**
C_4F_8 Flow Rate	0 sccm	100 sccm
SF_6 Flow Rate	130 sccm	0 sccm
O_2 Flow Rate	13 sccm	0 sccm
Pressure	10-15mTorr	
Generator Power (13.56MHz source)	600W	600W
Platen Power (380kHz source)	16W	0W
Cycle Time	5s	4s

A SEM view of a trench profile with ~0.15µm bow from each side is shown in Figure 4-3. The trench opening of 6µm is characterized for 50µm deep on a test silicon wafer.

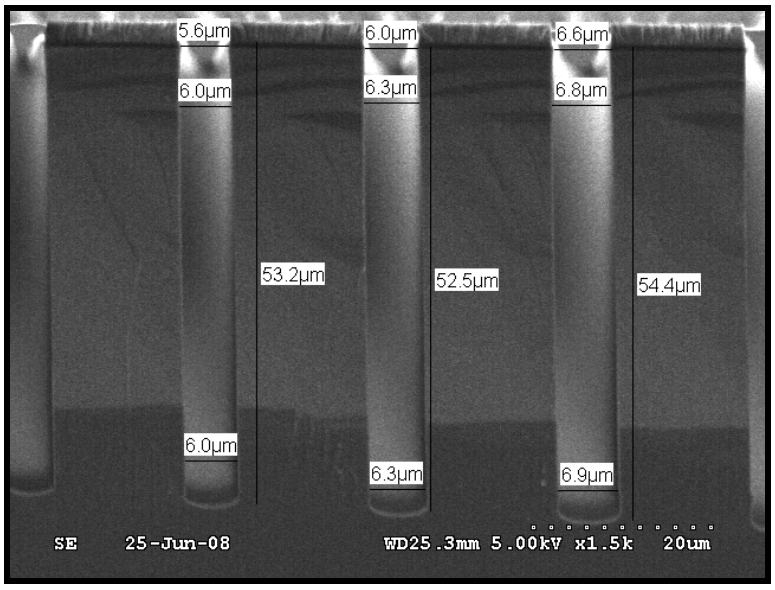

Figure 4-3: A SEM view of a straight trench profile with ~0.15µm bow from each side.

4.3.3 POLYSILICON ETCHING PARAMETERS

The next important step is poly etching inside the trenches using Bosch process. Polysilicon were etched inside the trenches using the modified Bosch recipe which can be achieved by further optimization of recipe parameters expressed in Table 4-2. It must be noted that higher platen power (20-22W) and larger etch/passivition cycle time (6.5/5) can be employed to ensure that the poly is completely etched all the way to the bottom of the trenches. This step should be characterized on SOI substrates rather than test wafers to monitor that the trenches are free from poly debris in the vicinity of SACOX on the trench sides and buried oxide at the bottom of the trenches. It must be noted that the existence of any poly debris/residues inside the trenches creates the electrical short between the electrodes or between the disk and the electrodes. If it is necessary, the dies can be wet-oxidized (0.2-0.3μm thick silicon oxide) to eliminate the existence of any poly debris inside the high-aspect ratio trenches.

CHAPTER 5

CHARACTERIZATION RESULTS

5.1 OVERVIEW

This chapter presents the characterization results of fabricated capacitive bulk acoustic wave (BAW) disk gyroscopes in (111) and in (100) single crystal silicon (SCS). First, measurement results of disk gyroscopes in (111) SCS substrates are presented and discussed. Next, disk structures with non-uniform and uniform sized perforations are experimentally characterized in (100) SCS substrates. The frequency responses and performance parameters were measured for these devices, both in vacuum and in air. The *Q*s and scale factors of these prototype gyroscopes were characterized over a temperature range of 60°C, showing these devices' high thermal stability. Also, these results demonstrate that these devices do not require the vacuum environment that low frequency, flexural-based gyroscopes do. This simplifies the wafer-level encapsulation of these devices, resulting in better long-term reliability and reduced cost. In addition, very large bandwidth, in the range 30-400Hz, was achieved for these devices in matched-mode operation in vacuum and air, making them to be suitable for the relatively fast response time needs of consumer electronics applications. Furthermore, utilizing uniform small sized holes enables matched-mode operation without requiring the application of electrostatic tuning voltages, reducing the complexity of the interface circuit and simplifying the system level architecture.

5.2 EXPERIMENTAL SETUP AND PROCEDURE

A number of (111) and (100) single crystal silicon disk gyroscopes were fabricated and their performance parameters (*i.e.* scale factor and bias drift) were characterized. The experimental setup used for the measurement is illustrated in Figure 5-1.

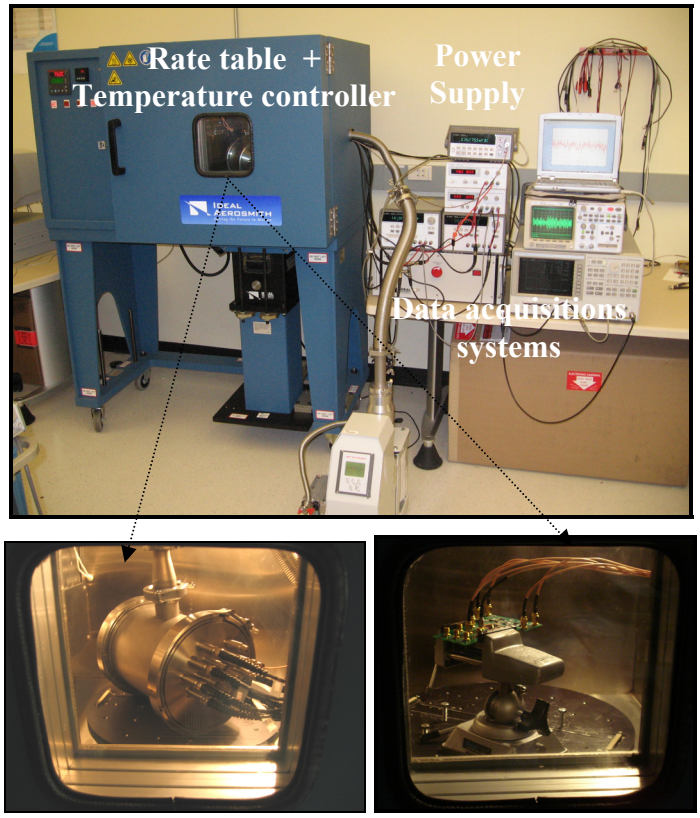

(a) Operation in vacuum (b) Operation in air

Figure 5-1: The measurement set-up used for BAW gyroscopes.

The MEMS gyroscope chip was mounted on a printed circuit board (PCB) including a drive loop and sense amplifiers [73], shown in Figure 5-2. All coupled drive, sense and tuning electrodes as well as polarization voltage (V_p) pads are connected to the board by wirebonding.

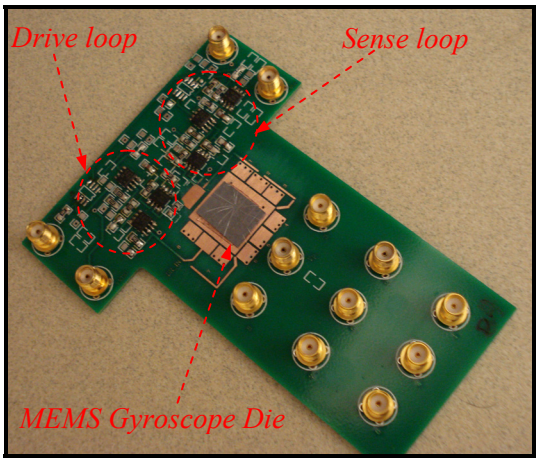

Figure 5-2: The PCB used for mounting the MEMS die and the discrete drive and sense loops.

The entire board was placed inside a vacuum chamber and coaxial cables were used to connect a network analyzer (Agilent 4395A) to the device in a two-port configuration. A sinusoidal drive signal, generated by the network analyzer, was applied to the drive electrode. Accompanying that, an independently set DC polarization voltage was applied to the disk through poly traces, and the rest of tuning electrodes were grounded. The output signal from the sense electrode was interfaced with the sense amplifiers on the PCB and the output returned to the network analyzer. The network analyzer compiled a frequency response curve, and from the *Q*s of these devices and the frequency split between the two degenerative modes was subsequently identified. Then, proper DC voltages were applied to the tuning electrodes to electrostatically tune and match the modes. Meanwhile, quadrature errors were cancelled by the application of appropriate DC voltages to the assigned electrodes. Next, a known rotation rate was applied to the whole system using a rate table (Ideal Aerosmith, 1291BR controller). The output rate signal (Coriolis signal) was extracted from the carrier signal using the sense loop, and recorded with an oscilloscope (Agilent DSO6014A). The output voltages were measured

for a number of applied rotation rates to determine the scale factor of these devices. After measuring the scale factor and matched-mode Q, the next most critical gyroscope performance parameters are scale factor stability and bias drift. These are directly affected by the stability of the mechanical quality factor. This stability can be evaluated over a constant pressure and temperature for a long term run. The zero rate output (ZRO) is sampled using digital multi-meter (Agilent 34401A, 6-1/2 digit multimeter) and an Allen variance method is employed to measure the bias drift from the collected zero rate output (ZRO) data.

5.3 RESULTS OF (111) SCS GYROSCOPES

A SEM view of a fabricated 800μm diameter (111) SCS disk gyroscope on a 35μm thick SOI wafer is shown in Figure 5-3. To operate the disk in its primary elliptic modes in (111) silicon, an isotropic material [76, 77], the release holes as well as the electrodes are placed and repeated symmetrically at every 45°. The poly traces provide the polarization voltage to the disk. The thickness of the disk is equal to the SOI device layer thickness (35μm), while the capacitive gap between the electrodes and the disk is 180nm. Also, each polysilicon electrode partially extends over the disk to provide an out of plane shock stop.

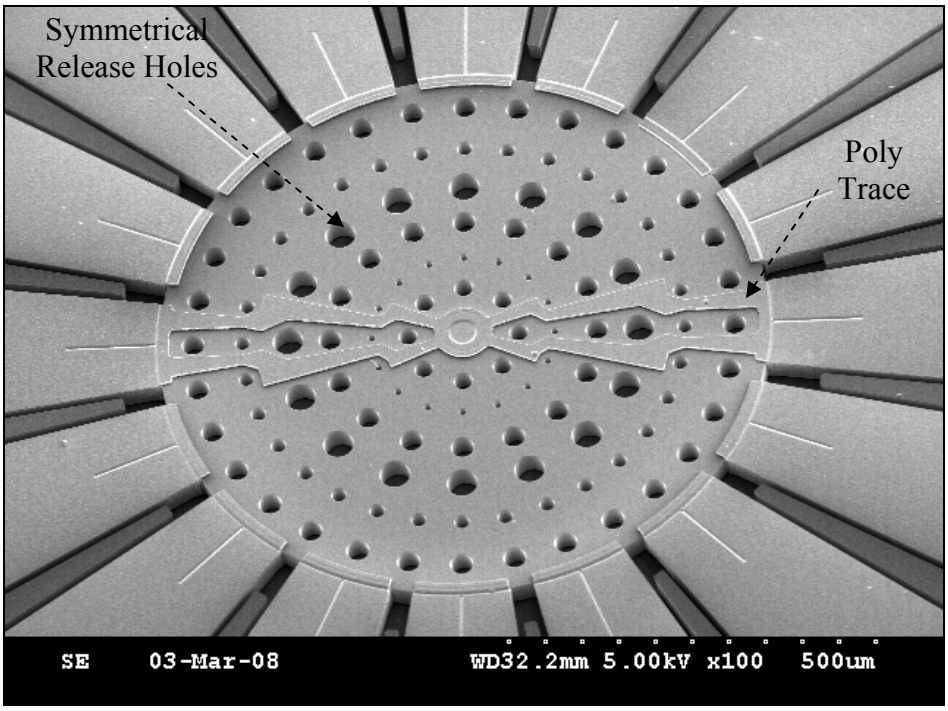

Figure 5-3: SEM views of an 800μm diameter (111) silicon disk gyroscope with 180nm capacitive gap in a 35μm thick disk.

The frequency response of the primary elliptic modes for an 800μm diameter (111) silicon disk gyroscope with the application of V_p=3V is shown in Figure 5-4 (a). The two primary elliptic degenerative modes of the fabricated device were observed at 4.23MHz with a frequency split of 700Hz, which is in good agreement with ANSYS simulation results. As a result, assuming isotropic material properties for (111) SCS disks operating in their in-plane elliptic modes is verified with measured results. In 1mTorr vacuum, the measured *Q*s were 186,000 and 180,000 at the sense and drive modes, Figure 5-4 (b). The corresponding *Q* values in 1Torr vacuum were also high (179,000 and 172,000) for this device.

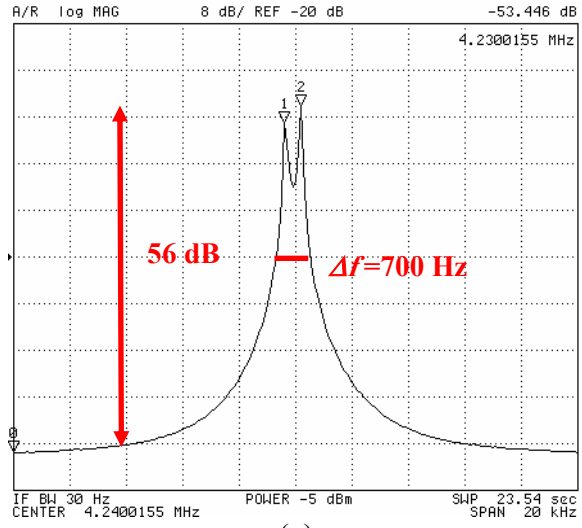

(a)

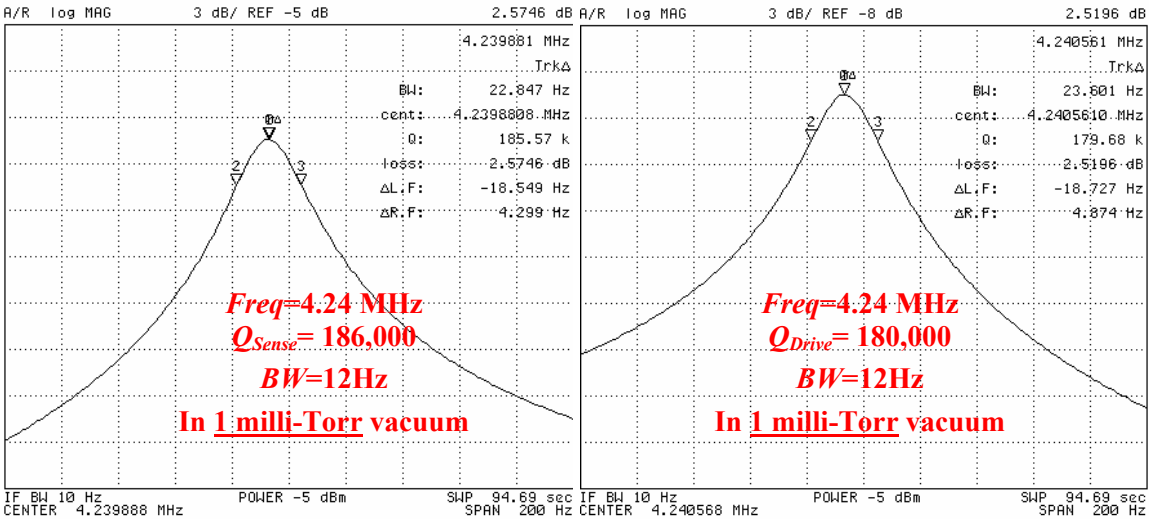

(b)

Figure 5-4: Frequency response of primary elliptic degenerative modes of an 800µm diameter (111) silicon disk gyroscope at 4.24MHz in 1mTorr vacuum with V_p=3V and Δf= 700Hz, showing the Q of 186,000 at sense mode in 1mTorr vacuum.

The large measured frequency split of 700Hz between the two modes was lowered to 450Hz with the application of very small electrostatic tuning voltages (V_T<10V), Figure 5-5.

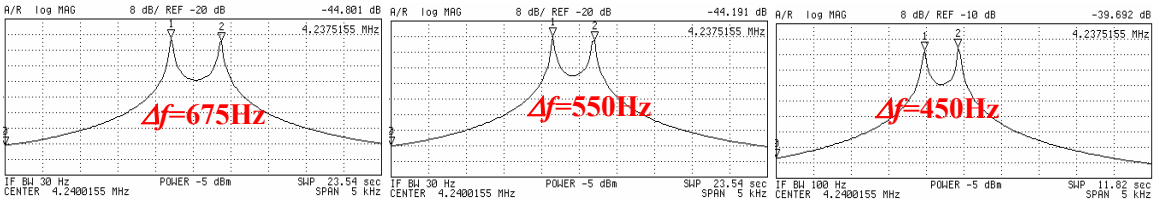

(a) (b) (c)

Figure 5-5: Collection of plots showing electrostatic frequency tuning of an 800µm diameter BAW disk gyroscope in (111) SCS: (a) V_P=5V, $V_{T\text{-}drive}$=5V, $V_{T\text{-}sense}$=5V, (b) V_P=5V, $V_{T\text{-}drive}$=5V, $V_{T\text{-}sense}$=6V and (c) V_P=5V, $V_{T\text{-}drive}$=-3V, $V_{T\text{-}sense}$=8.5V.

Further tuning was not possible because the device developed an electrical short at the tuning electrode due to the application of large tuning voltages.

The frequency separation between two modes can be addressed not only by electrostatic tuning but also by optimizing the design and fabrication process. This facilitates the mode matching procedure, most importantly requiring smaller tuning voltages. Even without optimization, it is expected that the lower frequency separation can be achieved by lowering the operating frequency. As a result, a 1200µm diameter (111) SCS disk gyroscope operating at ~3MHz is characterized.

The SEM view of a fabricated 1200µm diameter (111) gyroscope on 35µm thick SOI is shown in Figure 5-6. The close-up view of an electrode area shows the gap-aspect ratio of ~200.

The frequency response of the primary elliptic modes for the 1200µm diameter disk gyroscope in (111) SCS is observed at 2.92MHz. The primary elliptic modes of this device were observed to be less than 100Hz apart without applying any tuning voltage, as shown in Figure 5-7. The $Q_{\text{effective-sense}}$ of this device was 66,000 and 58,000, in 1mTorr and 1Torr vacuum, respectively.

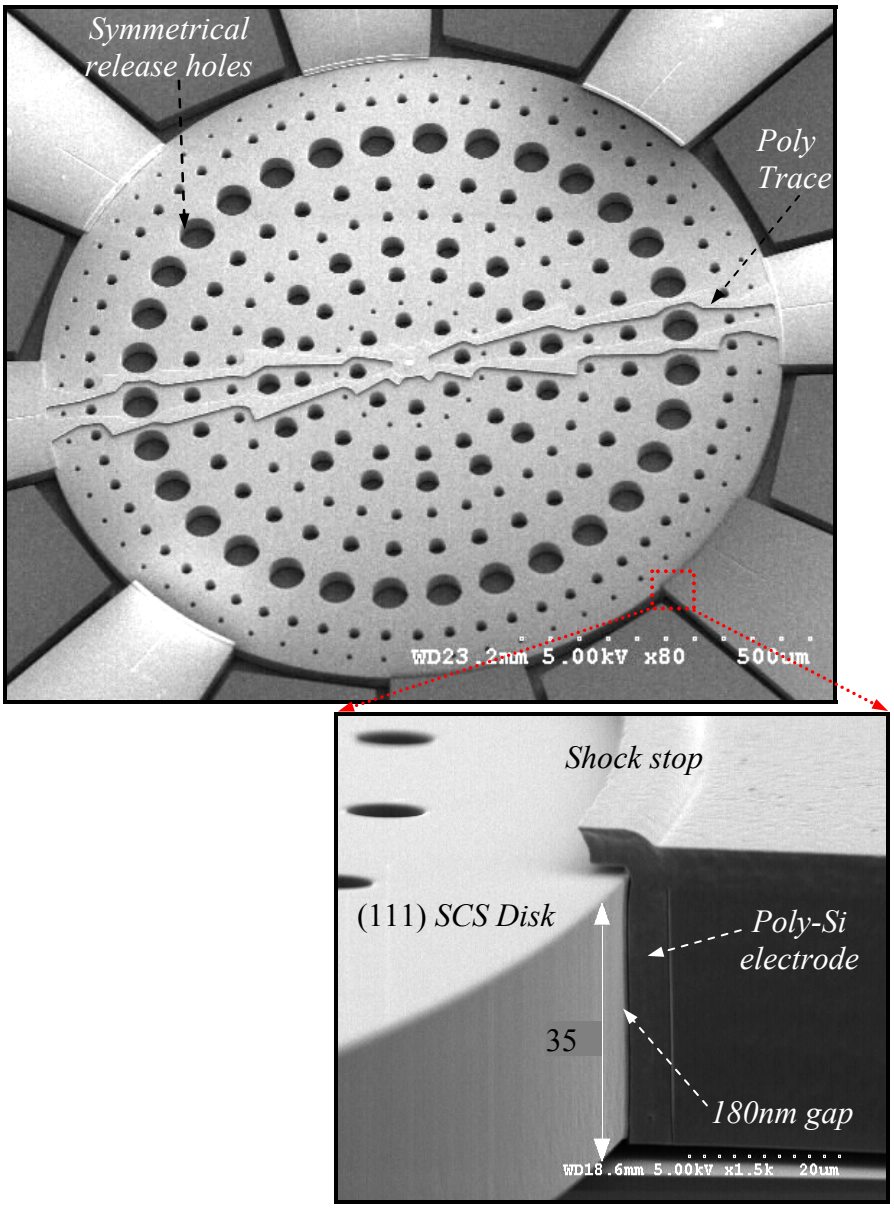

Figure 5-6: SEM views of a 1200μm diameter (111) silicon disk gyroscope and the close up view of an electrode area showing 180nm capacitive gap in a 35μm thick disk.

A number of rotation rates around the *z*-axis were applied to a 1200μm diameter disk gyroscope and the device's response was measured, shown in Figure 5-8. The measured rate sensitivity was 320μV/°/sec with $Q_{\text{effective-sense}}$ of 66,000 and V_P=10V. The signal conditioning circuitry used in this experiment was based on discrete electronic components.

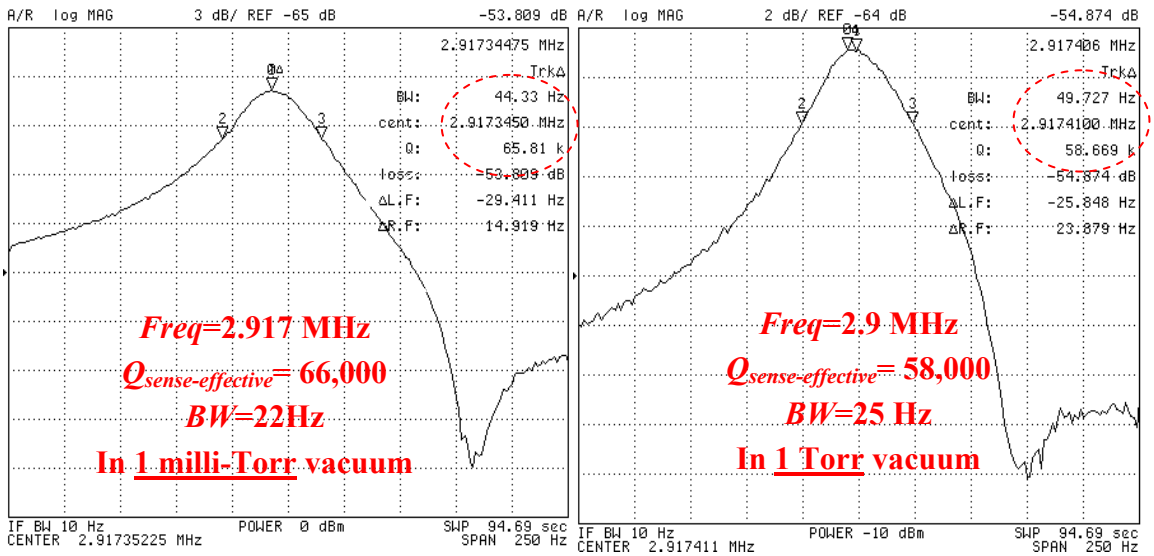

(a) (b)

Figure 5-7: Frequency response of primary elliptic modes in a 1200μm diameter (111) silicon disk gyroscope at 2.9MHz in: (a) 1mTorr vacuum with V_p=5V; (b) 1Torr with V_p=7V.

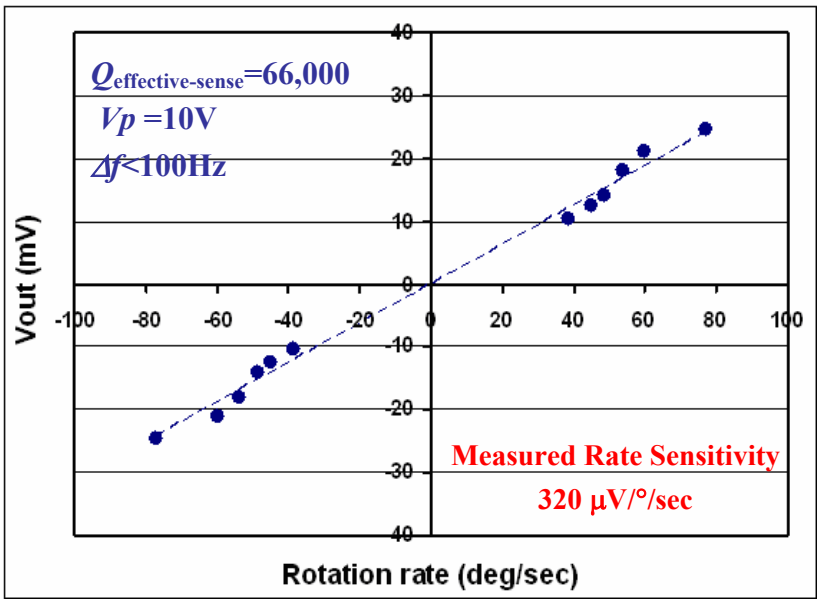

Figure 5-8: The measured rate sensitivity results around *z*-axis from a 1200μm diameter (111) SCS disk gyroscope with discrete electronics, showing the rate sensitivity of 320μV/°/sec at V_p=10V.

Next, scale factor stability and bias drift, the most critical performance parameters, were characterized in these gyroscopes. The scale factor stability is directly affected by the

stability of $Q_{effective\text{-}sense}$ over time. It was observed that the measured $Q_{effective\text{-}sense}$ remained constant over a period of 24 hours at a fixed temperature (room temperature) and pressure. The zero rate output (ZRO) of the device was logged over this period. An Allan variance analysis [33] was performed on the collected data to characterize long-term stability. The root Allan variance plot for the 1200μm diameter (111) SCS disk gyroscope is shown in Figure 5-9 and inset shows a time-slice of the ZRO data. From this graph, the angle random walk (ARW) is determined by the t=1s value of the plot with a -1/2 slope. The measured ARW of the device is 0.28 °/√hr, implying the output referred total equivalent noise of 16.8 °/hr/√Hz. The minimum of the Allan variance plot gives the value of bias drift, which is measured for this sensor to be 17°/hr. If desired, quadrature error can be further minimized by applying DC voltages to the other electrodes, which would improve both sensitivity and bias stability in these devices.

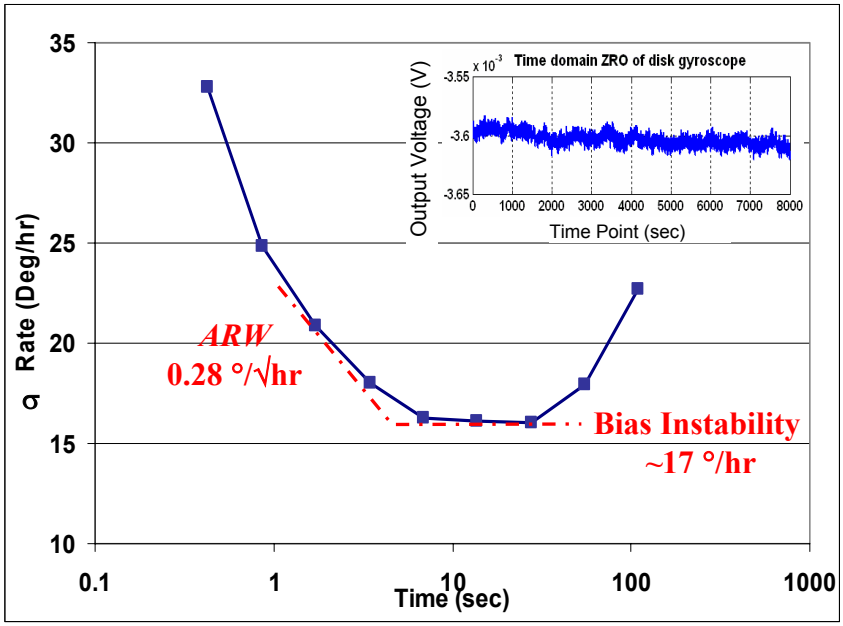

Figure 5-9: Root Allan variance plot of a 1200μm diameter (111) SCS disk gyroscope at zero rate output (ZRO). The inset shows the time domain plot of the ZRO of disk gyroscope.

5.4 RESULTS OF (100) SCS GYROSCOPES

A number of disk gyroscopes with nonuniform release holes were fabricated and characterized on a variety of thick (100) SOI substrates (30μm-60μm). Among them, the measurement results of 40μm-thick disk gyroscopes are presented in this section. A SEM view of a fabricated 800μm diameter (100) disk gyroscope with nonuniform perforations on 40μm-thick SOI is shown in Figure 5-10.

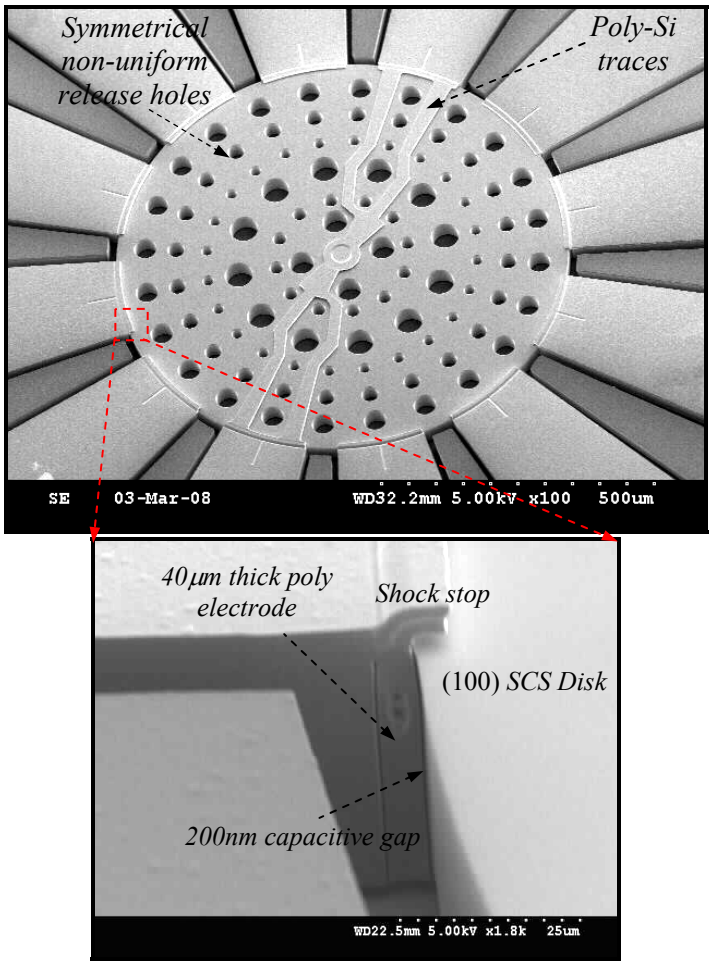

Figure 5-10: SEM view of an 800μm diameter (100) Si disk gyroscope with 200nm capacitive gap and 40μm thick disk.

As discussed in Chapter 3, anisotropic behavior of (100) SCS leads to release holes and electrodes being placed and repeated symmetrically every 30°. The close-up view of the

electrode shows a capacitive (electrode-disk) gap of 200nm, giving a gap aspect ratio of 200 in the 40μm thick device layer. In addition, the poly electrode is extended 10μm over the top of the disk to form a shock stop. Boron-doped polysilicon traces are connected to the center of the disk to provide DC bias to the disk.

5.4.1 Frequency Characterization and Mode Matching

The secondary elliptic modes of this device were observed at 5.94 MHz with a frequency split of 450Hz (Figure 5-11), which is in good agreement with ANSYS simulation results, presented in chapter 3.

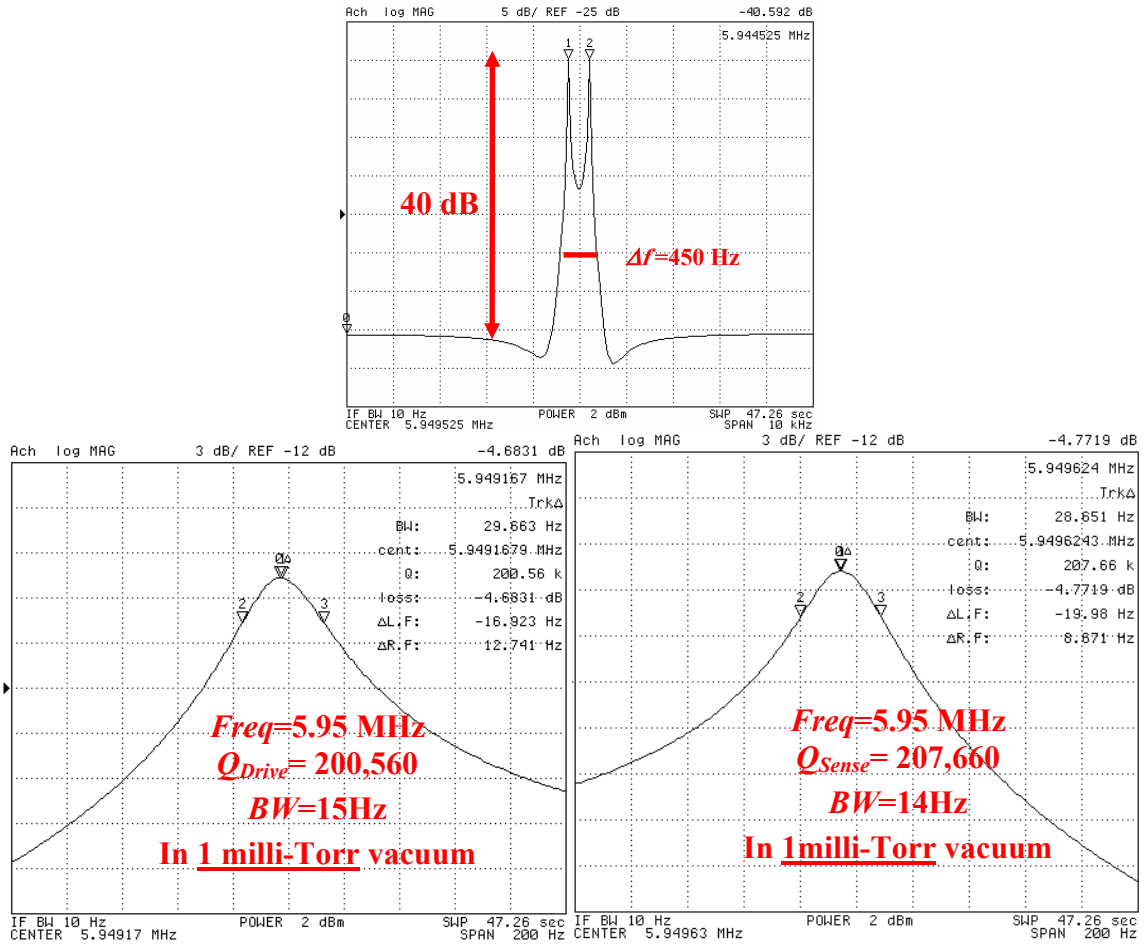

Figure 5-11: The frequency response of the secondary elliptic modes of an 800μm diameter (100) SCS disk gyroscope with nonuniform perforations, showing the resonance frequency of 5.94MHz with Δf=450Hz in 1mTorr vacuum with V_p of 6V.

The Qs were measured and recorded to be 200,560 and 207,660 for drive and sense modes, respectively, in 1mTorr vacuum (Figure 5-11). The corresponding Q values in 1Torr vacuum were still very high and were recorded to be 185,280 and 192,060 for drive and sense, respectively.

A very small frequency split of ~75ppm compared to the center operating frequency (5.95MHz) is measured for this device, however still further frequency tuning and matching is required to improve the device performance. To accomplish this, the frequency split between the modes is electrostatically tuned and matched, employing the tuning method discussed in Chapter 3 of this thesis. Given that the frequency of the drive mode is lower than the sense mode's frequency (f_{drive}=5.9492 < f_{sense}=5.9496MHz), the tuning voltages of $V_{T\text{-drive}}$>0 and $V_{T\text{-sense}}$<0 is applied to the tuning electrodes. The frequency responses of the modes after the application of optimal tuning voltages are recorded and shown in Figure 5-12. Even with the two modes' frequencies being matched, the quadrature error still needs to be cancelled. This was done by the

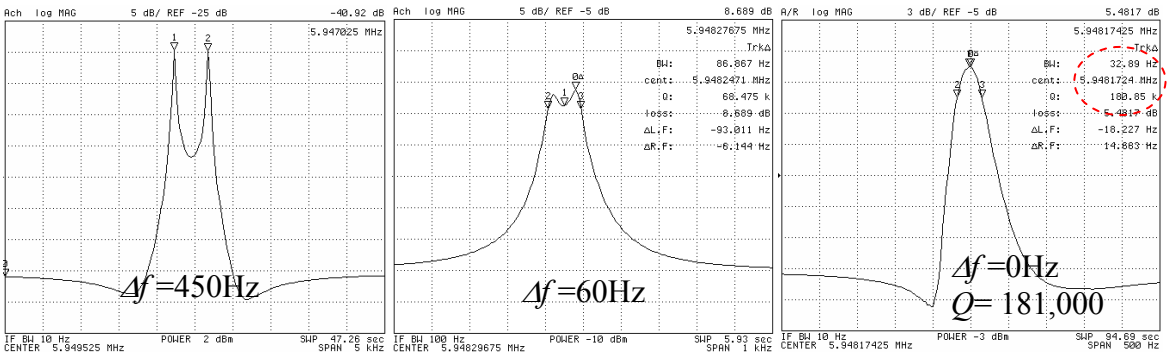

(a) V_p=6V, $V_{T\text{-drive}}$=6V, $V_{T\text{-sense}}$=6 V

(b) V_p=9V, $V_{T\text{-drive}}$=9V, $V_{T\text{-sense}}$= -16 V

(c) V_p=13.2V, $V_{T\text{-drive}}$=9 V, $V_{T\text{-sense}}$= -25 V

Figure 5-12: Collection of plots showing electrostatic frequency tuning and matched-mode of an 800μm diameter BAW disk gyroscope in (100) SCS.

application of the appropriate electrostatic forces to align the antinode lines of modes with the electrodes centers.

A matched-mode Q of 235,810 was recorded after minimizing the quadrature error as shown in Figure 5-13.

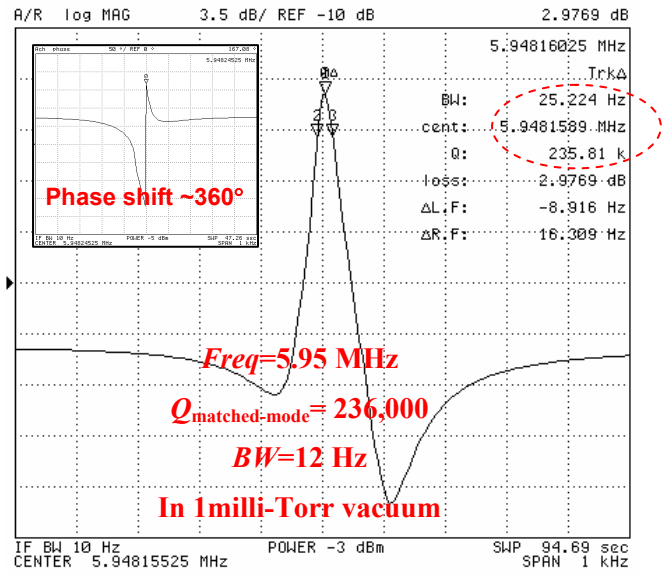

Figure 5-13: The matched-mode operation of an 800µm diameter (100) SCS disk gyroscope with the application of V_p=13.2V, $V_{T\text{-}drive}$=9V, $V_{T\text{-}sense}$=-26V, $V_{quadrature}$=±14V after minimizing the quadrature errors.

5.4.2 PERFORMANCE CHARACTERIZATION

The performance parameters such as scale factor and bias drift are measured and discussed in this section. The zero rate output (ZRO) of 800µm diameter disk gyroscope at matched mode is measured and shown in Figure 5-14. The bottom trace is the ZRO at the sense electrode and the top trace shows the output of the drive mode. An output of 1.32V peak-to-peak was measured at the drive electrode, which translates into 5.2nm drive amplitude. Also, a phase shift of ~90° is measured between the drive and sense modes after quadrature cancellation.

Subsequently, rotation around the *z*-axis is applied to this device and the demodulated output sinusoidal signal is measured. Figure 5-14 shows the demodulated response of the device to the applied 50°/sec *z*-axis rotation rate at matched-mode. The scale factor is measured from only *one sense electrode* both for split-mode and matched-mode operation, and the results are shown in Figure 5-15.

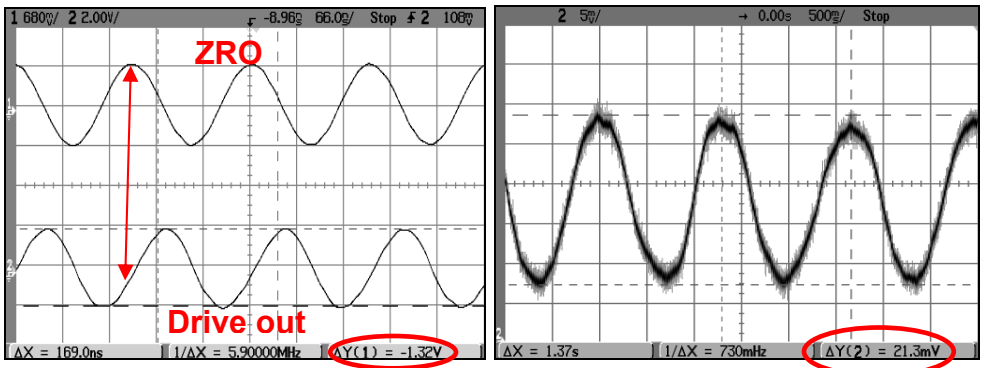

(a) (b)

Figure 5-14: (a) Zero rate output of an 800µm diameter (100) SCS disk gyroscope at matched-mode (b) Rotation response of the prototype gyroscope to the applied 50°/sec *z*-axis rotation rate at matched-mode.

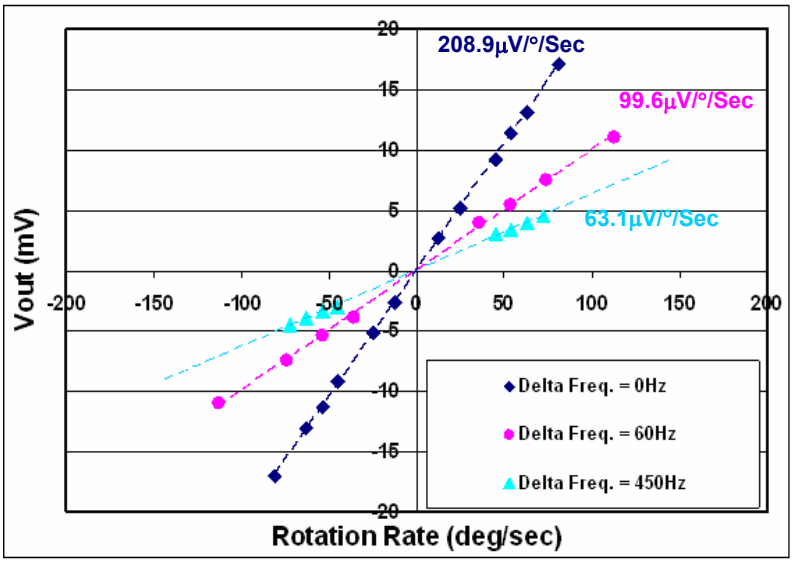

Figure 5-15: The measured rate sensitivity results from one sense electrode of the 800µm diameter disk gyroscope at split modes with Δf=450Hz and Δf=60Hz and at matched-mode operation before quadrature cancellation with V_p=13.2V with discrete electronics.

Before applying any tuning voltages, a rate sensitivity of 63.1 μV/°/sec was measured from the sense mode with Δf=450 at V_p=6V. Then, the two modes were electrostatically tuned to Δf=60 Hz with the application of V_p=9V and a rate sensitivity of 99.6 μV/°/sec was then measured. Finally, the two modes were completely matched and the rate sensitivity before quadrature cancellation was measured to be 208.9 μV/°/sec at V_p=13.2V with $Q_{matched\text{-}mode}$ of 180,850 in 1mTorr vacuum.

Later, the quadrature error was minimized and the matched mode Q was improved to 235,810. A measured sensitivity of 268 μV/°/sec was achieved with discrete electronics and a V_p of 13.2V with $Q_{matched\text{-}mode}$ of 235,000 in 1mTorr vacuum, as shown in Figure 5-16. It is worth noting that the scale factor of these devices can be improved by ~5× if other sense electrodes located around the disk are coupled with the assigned sense electrode.

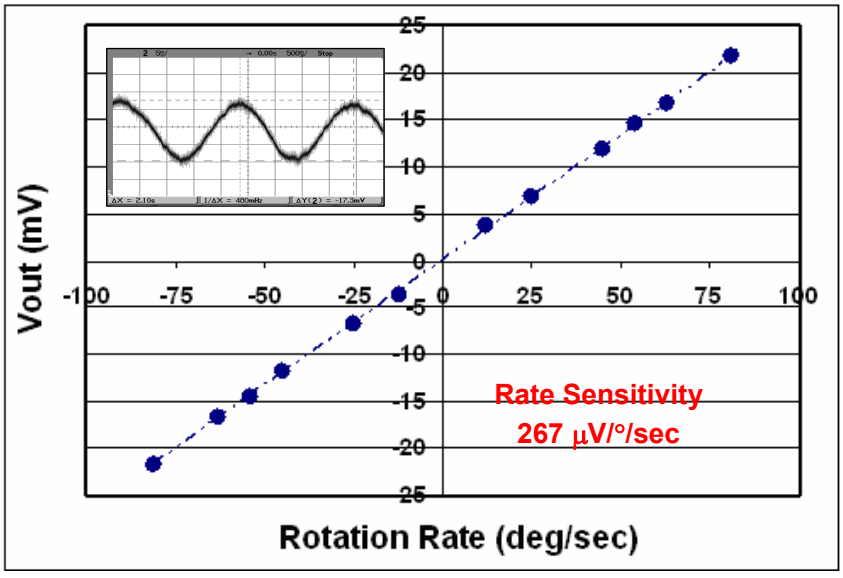

Figure 5-16: The measured rate sensitivity results from one sense electrode of the 800μm diameter disk gyroscope at matched-mode operation after quadrature cancellation with V_p=13.2V and Q=236,000 with discrete electronics.

Next, the zero rate output (ZRO) of the prototype device was sampled and an Allan variance analysis was performed to characterize the long-term stability of the matched-mode device interfaced with the discrete electronics. The root Allan variance plot of the prototype disk gyroscope at matched-mode after balancing is shown in Figure 5-17. Allan variance plot obtained without applying any pre-whitening or filtering is shown in Figure 5-17. From this graph, the estimated angle random walk (ARW) is determined by the t=1s value of the plot with a -1/2 slope [108, 109]. The measured ARW of the device is 1.28 °/√hr, implying the output referred total equivalent noise density of 76.8 °/hr/√Hz. The minimum of the Allan variance plot gives the value of bias drift [109], which is measured for this sensor to be 77°/hr at the mode-matched operation.

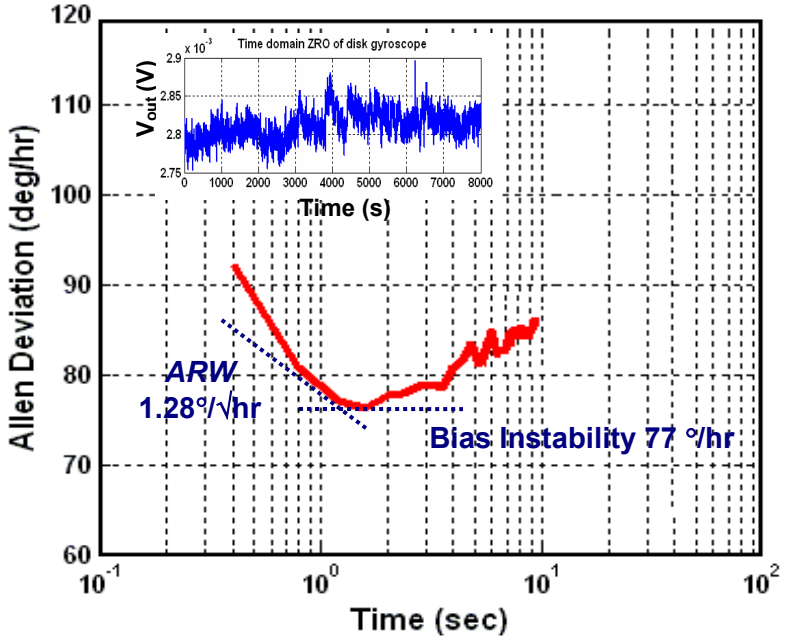

Figure 5-17: Root Allan variance plot of an 800µm diameter disk gyroscope with nonuniform perforations at zero rate output (ZRO) in 1mTorr vacuum. The inset shows the time domain plot of the ZRO of this prototype device.

5.4.3 PRESSURE CHARACTERIZATION

The frequency response of degenerative elliptic modes for the same 800μm diameter disk gyroscope with nonuniform perforations was characterized at multiple vacuum pressures. The frequency of both drive and sense modes changed only ~0.001% over the pressure range of 0.8mTorr to 40Torr and the frequency separation between two modes remained constant at 450Hz from 0.8mTorr to 25mTorr, shown in Figure 5-18 (a). In addition, the *Q*s of the same prototype device were characterized over the same pressure range, as shown in Figure 5-18 (b). The *Q*s dropped less than 7% (from 200,000 to 186,000) over the pressure range 0.8mTorr to 1Torr at the operating frequency of 5.94MHz, showing the high stability of high *Q*s in these modes over this vacuum pressure range. Without a need for mTorr vacuum level, wafer-level packaging will be simplified.

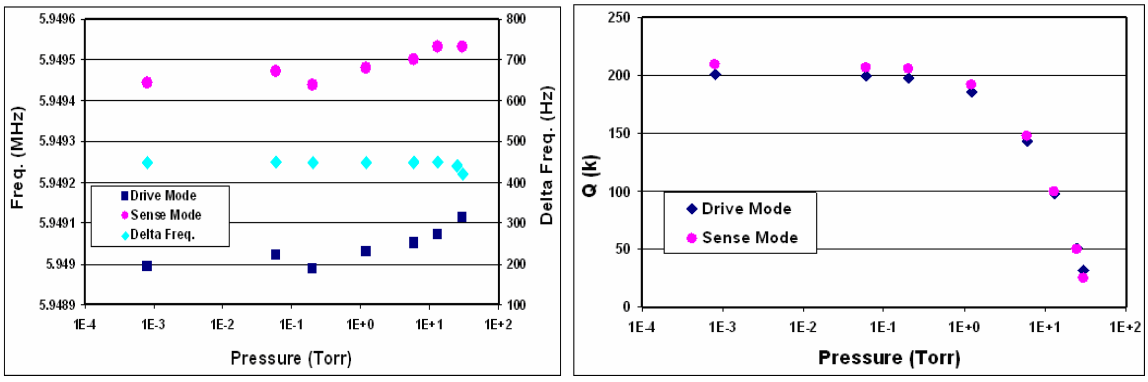

(a) (b)

Figure 5-18: (a) The frequency response of the drive and sense modes and (b) Measured *Q* over the vacuum pressure range from 0.8mTorr to 40Torr in an 800μm diameter disk with nonuniform perforations.

5.4.4 TEMPERATURE CHARACTERIZATION

The temperature-induced frequency drift of an identical gyroscope, were measured using a temperature control chamber (Ideal Aerosmith, 1291BR controller). As shown in Figure

5-19, the measured frequency drift for both drive and sense modes has a linear trend with a slope of -26ppm/°C over the temperature range of -5°C to 55°C both in 0.1mTorr and 2Torr vacuum. The frequency drift is mainly due to the temperature dependence of the Young's modulus of silicon [79, 110]. This causes both degenerative modes to track each other as temperature changes, and do so with the same slope. This implies the stability of the frequency separation between two modes over a temperature range of 60°C. Furthermore, the *Q*s of both sense and drive modes were characterized over a temperature range from -5°C to 55°C. Figure 5-20 demonstrates that the *Q*s of this prototype device decreased ~4% in 1mTorr vacuum and 4.6% in 2Torr vacuum over the 60°C temperature range. The measured results demonstrates much smaller decrease in total *Q* compared to the simulated Q_{TED} at elevated temperatures, indicating that the *Q*s in BAW gyroscopes are not mainly limited by TED. The reduction of *Q* at elevated temperature in these devices (<5% over ΔT=60°C) can originate from expansion of support size at higher temperature as well as lower Q_{TED} at higher temperature.

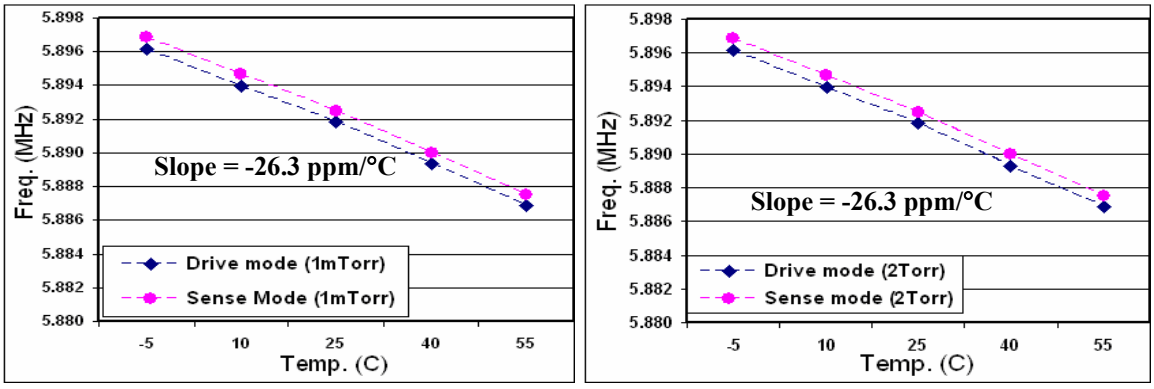

(a) (b)

Figure 5-19: Measured temperature-induced frequency drift of secondary elliptic modes in an 800μm diameter (100) SCS disk with nonuniform holes: (a) in 1mTorr and (b) in 2Torr vacuum.

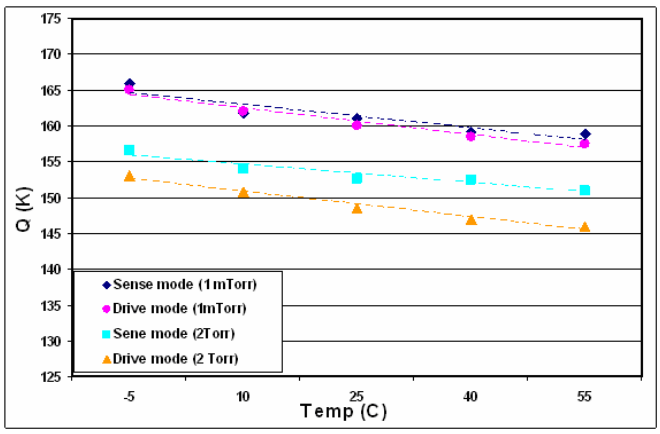

Figure 5-20: The temperature characterization of *Q*s in an 800µm diameter disk operating at their secondary elliptic modes over a temperature range of -5°C to 55°C.

5.5 Results of (100) SCS Gyroscopes with 8µm Perforations

The design of the perforations in the gyroscope disks, as discussed in Chapter 3, was optimized to significantly reduce the frequency split between two modes. Accordingly, a number of disk structures, incorporating uniform release holes with diameters between 6µm and 10µm, were fabricated and tested. The measurement results of devices with uniform 8µm diameter holes are presented in this section.

A SEM view of a fabricated 800µm diameter (100) disk gyroscope including uniform 8µm diameter holes on 40µm thick SOI is shown in Figure 5-21. In this modified design, boron-doped polysilicon traces still provide DC bias to the disk, but the poly traces' configuration was modified to prevent overlap with the release holes. Also, the capacitive gap of 180nm between the electrode and the disk in 40µm thick device was implemented, attaining a gap aspect ratio of 220.

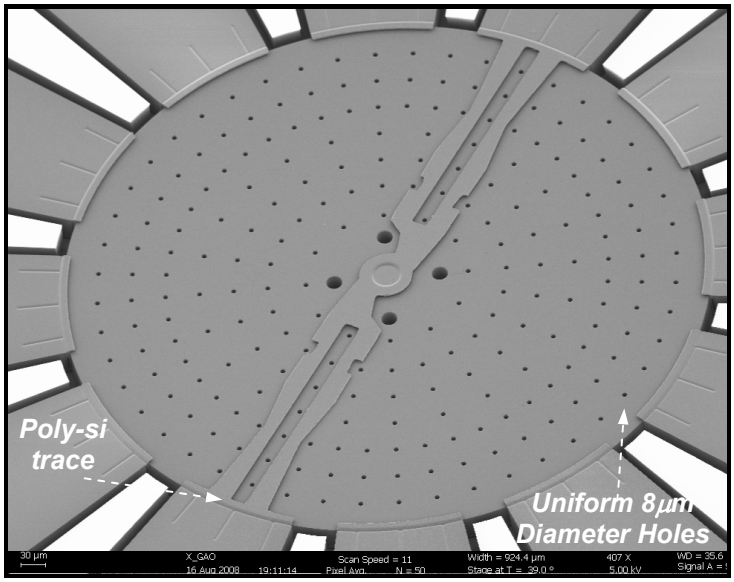

Figure 5-21: SEM view of an 800μm diameter disk gyroscope including uniform 8μm diameter holes in (100) SCS substrate with the capacitive gap of 180nm in 40μm thick silicon disk.

As one can observe, the release holes at the center of the disk are larger (18μm in diameter) and located at every 90°. This is to ensure the existence of a 30μm diameter buried oxide support at the center.

5.5.1 FREQUENCY CHARACTERIZATION

The frequency response of this prototype disk gyroscope was measured and shown in Figure 5-22. As expected, the two modes exhibited a narrowed frequency split of <120Hz. The secondary elliptic modes were observed to be matched at 7.27MHz in both 1mTorr vacuum and air. The matched-mode *Q*s of 82,736 and 13,239 were measured, respectively, in 1 mTorr vacuum and air at V_p=12V.

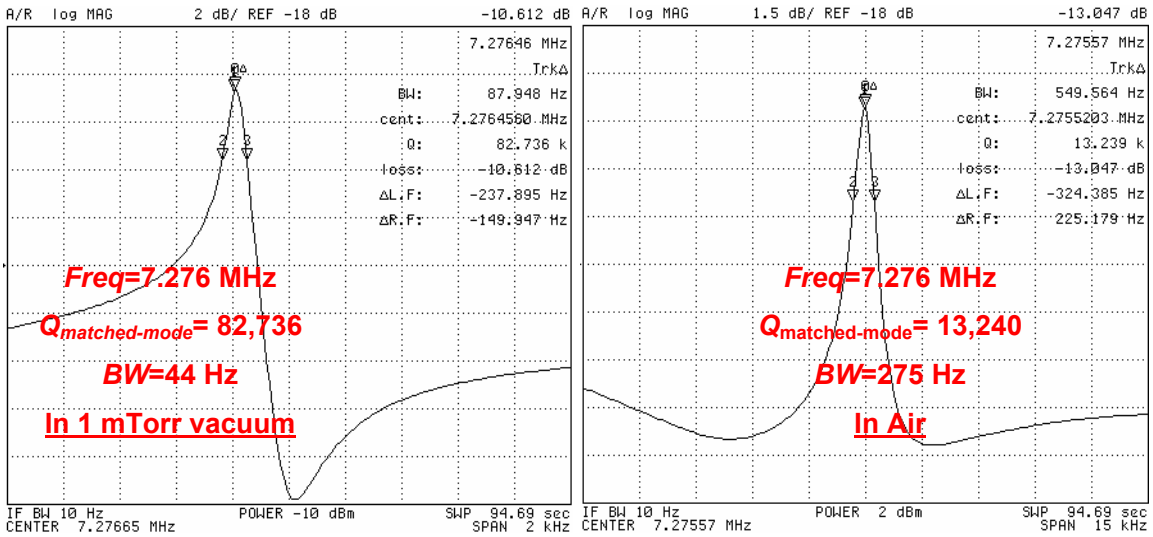

Figure 5-22: The frequency response of the secondary elliptic modes of an 800µm diameter (100) SCS disk gyroscope including uniform 8µm diameter holes, showing the matched-mode Q of 82,736 and 13,239 in 1mTorr vacuum and air with V_p of 12V.

5.5.2 PERFORMANCE CHARACTERIZATION

The scale factor and bias drift were measured for the prototype device in air and the results were summarized in this section. First, zero rate output (ZRO) of this device was measured at matched mode in 1mTorr vacuum and air, as shown in Figure 5-23. The drive output signal of this device was measured to be 609mV and 238mV in 1mTorr vacuum and air, respectively at V_p=12V, which translates into 2.5nm and 0.97nm drive amplitude. A number of rotation rates around the z-axis were applied to this device and the demodulated output sinusoidal signals were measured and recorded. The rate sensitivity was measured to be 28.8µV/°/sec in air at V_p =12V, shown in Figure 5-24. The inset in Figure 5-24 shows the demodulated output signal for the applied rotation rate of 35°/sec with f_{Corilis} of 0.75Hz and amplitude of 7.5°.

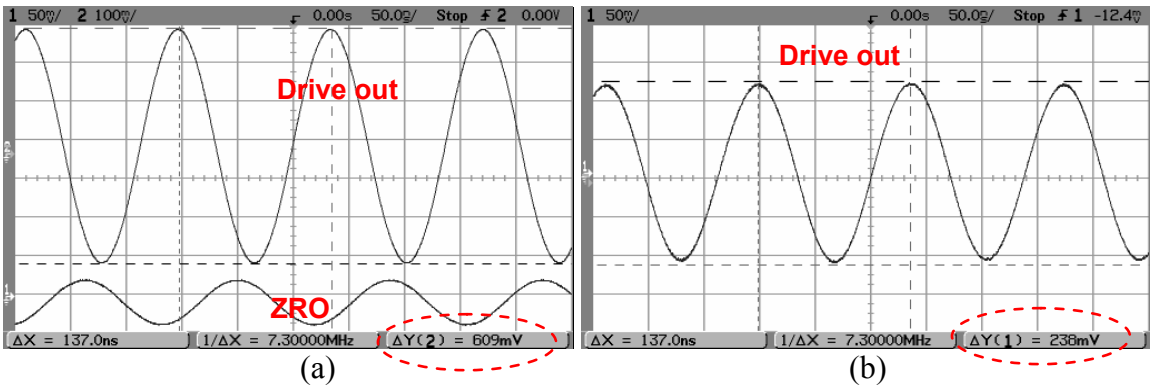

(a) (b)

Figure 5-23: Zero rate output of an 800µm diameter disk gyroscope including uniform 6µm diameter release holes at matched-mode.

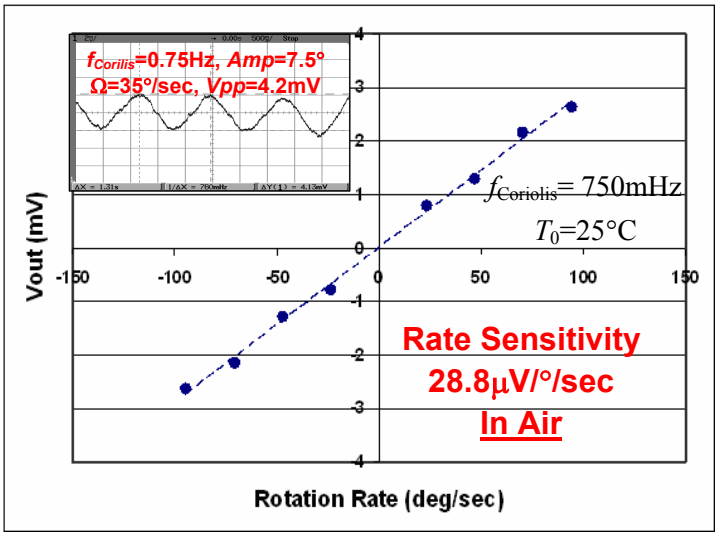

Figure 5-24: The measured rate sensitivity of an 800µm diameter disk gyroscope with uniform 8µm diameter holes in air at $Q_{\text{matched-mode}}$ of 9,000 with V_p=12V.

Similarly, the scale factor stability and bias drift were measured for this prototype device in air. It was observed that the matched mode Q remained constant over a period of 24 hours at a fixed room temperature and pressure. As before, the zero rate output (ZRO) of the prototype was sampled and an Allan variance analysis was performed to characterize the long-term stability of the matched-mode device. The root Allan variance plot of this device in air at matched mode is shown in Figure 5-25. The measured bias stability of this device in air is estimated to be 2.55 °/sec with the Q of 9000 and V_p=12V.

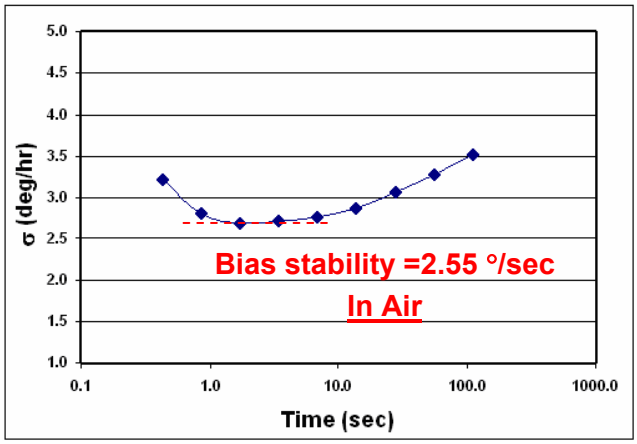

Figure 5-25: Root Allan Variance plot of an 800µm diameter disk gyroscope with uniform 8µm diameter release holes at zero rate output (ZRO).

5.5.3 TEMPERATURE CHARACTERIZATION

A similar prototype device was characterized over a temperature range of -5°C to 70°C in air. The modes remained matched over this temperature range. Figure 5-26 shows the frequency response of the matched mode prototype device in air at -5°C and 55°C.

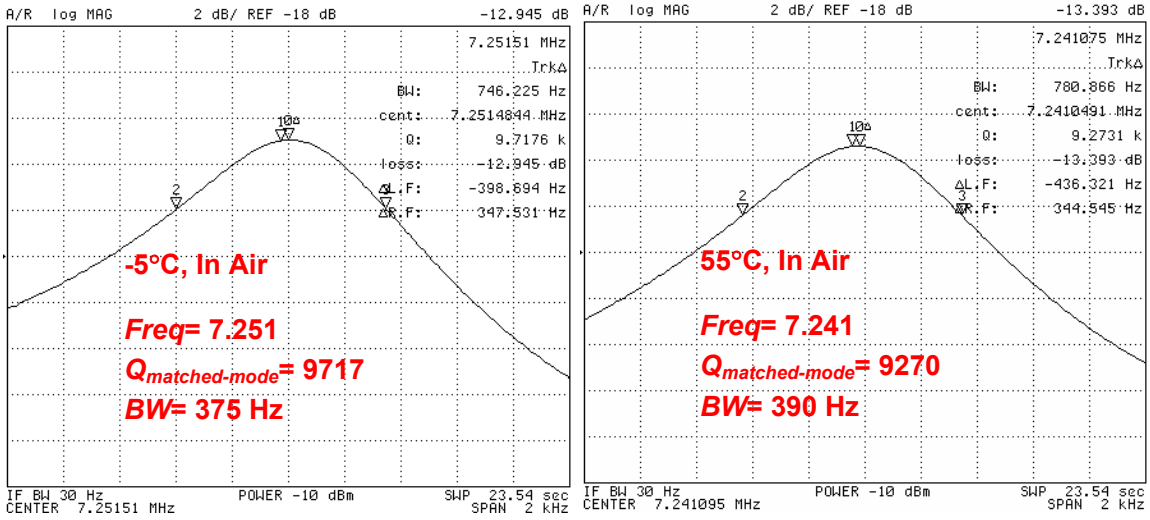

Figure 5-26: Frequency response of matched-mode in air for the prototype device at -5°C and 55°C.

The temperature-induced frequency drift of this device was measured to have a slope of -25.7ppm/°C in air, Figure 5-27. Also, the matched-mode *Q* was characterized and

measured for this temperature range, observing a ~7.7% reduction in the $Q_{matched\text{-}mode}$ for a temperature range of 75°C, as shown in Figure 5-27. In addition, the frequency bandwidth of this prototype device was characterized in air for the same temperature range. Figure 5-28 demonstrates that the 3-dB and 1-dB frequency bandwidths increased by ~8% over the temperature change of 75°C.

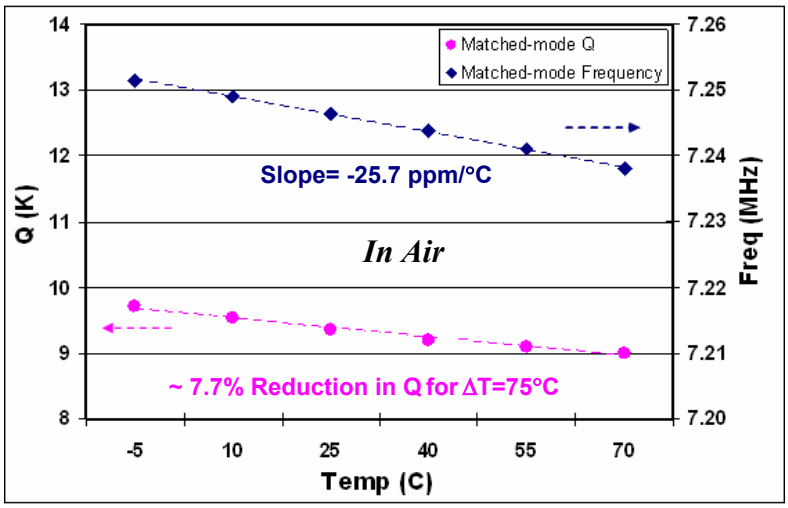

Figure 5-27: Temperature variation of matched-mode frequency and Q in air for an 800µm diameter (100) SCS disk gyroscope with uniform 8µm diameters holes, showing a linear frequency drift profile with a slope of -25.7ppm/°C and a reduction of ~7.7 % in $Q_{matched\text{-}mode}$ for ΔT=75°C in air.

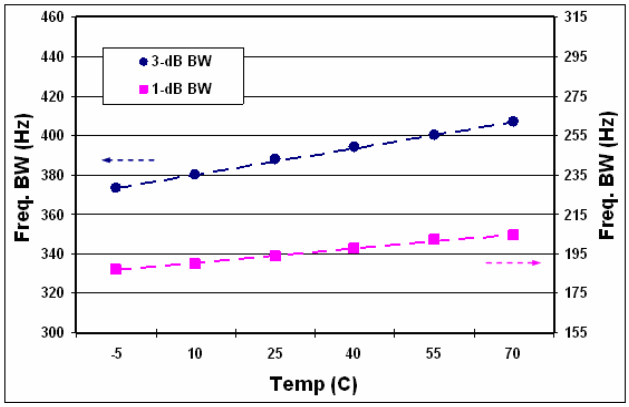

Figure 5-28: Temperature characterization of frequency Bandwidth in air for an 800µm diameter (100) SCS disk gyroscope with uniform 8µm diameters holes, showing an increase of ~7.48% and ~8.2% in 3-dB and 1-dB Bandwidth over 75°C temperature change, respectively.

5.6 RESULTS OF (100) SCS GYROSCOPES WITH 6µM PERFORATIONS

A SEM view of a fabricated 800µm diameter (100) disk gyroscope, with uniform 6µm diameter holes, implemented on 40µm thick SOI, is shown in Figure 5-29. Similarly, boron-doped polysilicon traces are connected to the center of the disk to provide DC bias to the disk. The close-up view of the electrode area shows a capacitive gap of 180nm between the electrode and the disk in 40µm thick device, again yielding a gap aspect ratio of 220.

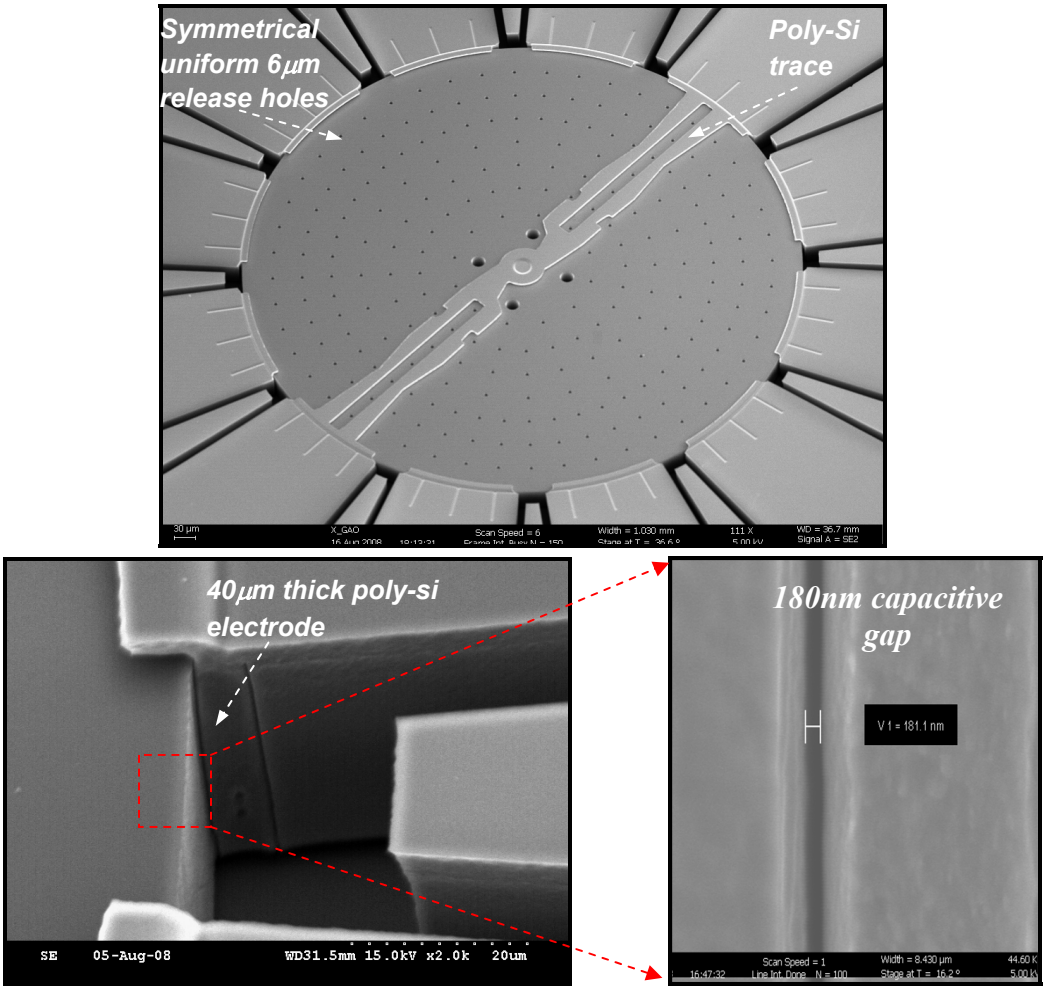

Figure 5-29: SEM view of an 800µm diameter disk gyroscope including uniform 6µm diameter holes in (100) SCS substrate with the capacitive gap of 180nm in 40µm thick disk.

5.6.1 FREQUENCY CHARACTERIZATION

The frequency response of this prototype disk gyroscope was measured and shown in Figure 5-30. As expected, a very small frequency split, ~100Hz, was found. The secondary elliptic modes were observed to be matched at 7.30MHz in 1mTorr vacuum and air. The matched-mode *Q*s of 73,000 and 14,435 respectively were measured in 1mTorr vacuum and air at V_p=7V.

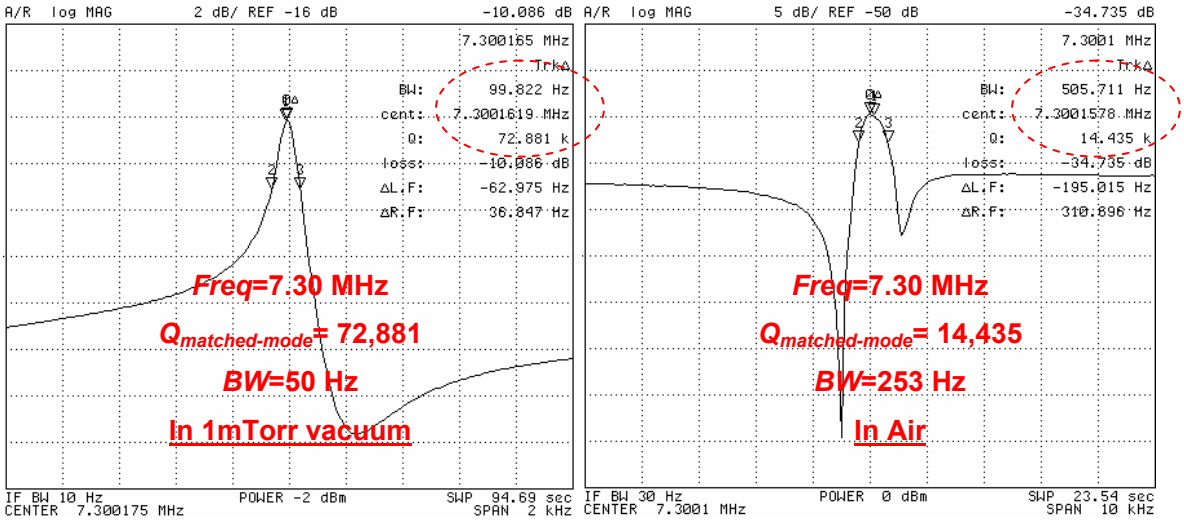

Figure 5-30: The frequency response of the secondary elliptic modes in an 800µm diameter (100) SCS disk with uniform 6µm diameter holes, showing the matched-mode *Q* of 14, 435 in air with V_p of 7V.

5.6.2 PERFORMANCE CHARACTERIZATION

The scale factor and bias drift for an 800µm diameter disk with uniform 6µm diameter release holes were measured in air. This section presents a summary of the results. The zero rate output (ZRO) of this device was measured at matched mode in air, as shown in Figure 5-31 (a). The drive amplitude from the drive output signal was measured to be 0.7nm, which is very low. This could be increased significantly by using larger AC drive

signals, as well as by using a larger V_p. Also the demodulated sinusoidal signal produced by an applied 82°/sec rotation about the *z*-axis is shown in Figure 5-31 (b).

Next, a number of rotation rates around the *z*-axis were applied to this device and the corresponding demodulated output sinusoidal signals were recorded. The rotation rate sensitivity was measured from only one sense electrode *in air*, as shown in Figure 5-32. The measured rate sensitivity of 64.5μV/°/sec is recorded with discrete electronics and V_p of 12.5V, with $Q_{matched\text{-}mode}$ of 14,435. The inset in Figure 5-32 shows the demodulated output signal when the device is rotated at 70°/sec.

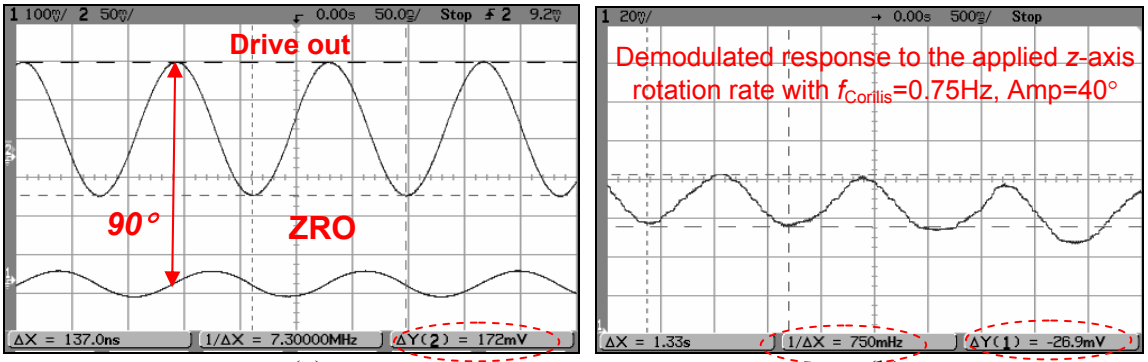

(a) (b)

Figure 5-31: (a) Zero rate output of an 800μm diameter disk gyroscope with uniform 6μm diameter release holes at matched-mode operation, (b) Demodulated rotation response of the prototype gyroscope to the applied 188°/sec *z*-axis rotation rate in air.

Similarly, the scale factor stability and bias drift were measured for this device in air. It was observed that the matched mode *Q* remained constant over a period of 24 hours at a fixed room temperature and pressure. The zero rate output (ZRO) of the prototype was sampled, and an Allan variance analysis was performed to characterize the long-term stability of the matched-mode device. The resulting root Allan variance plot is shown in Figure 5-33. The measured bias instability of this device is estimated in air to be 1.02

°/sec with the Q of 14,435 and V_p=12.5V. A time-slice of the ZRO is also shown in the inset of Figure 5-33.

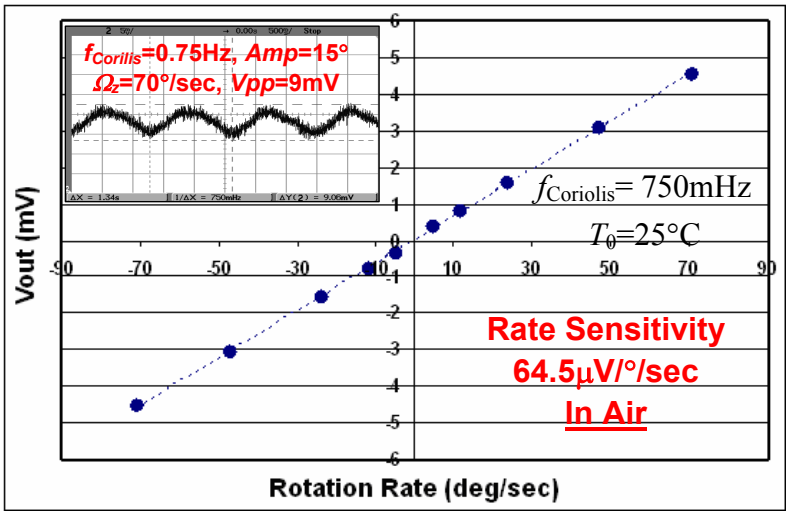

Figure 5-32: The measured rate sensitivity results from one sense electrode of an 800μm diameter disk gyroscope including uniform 6μm diameter release holes in air at Qmatched-mode of 14,435 with V_p=12.5V and discrete electronics.

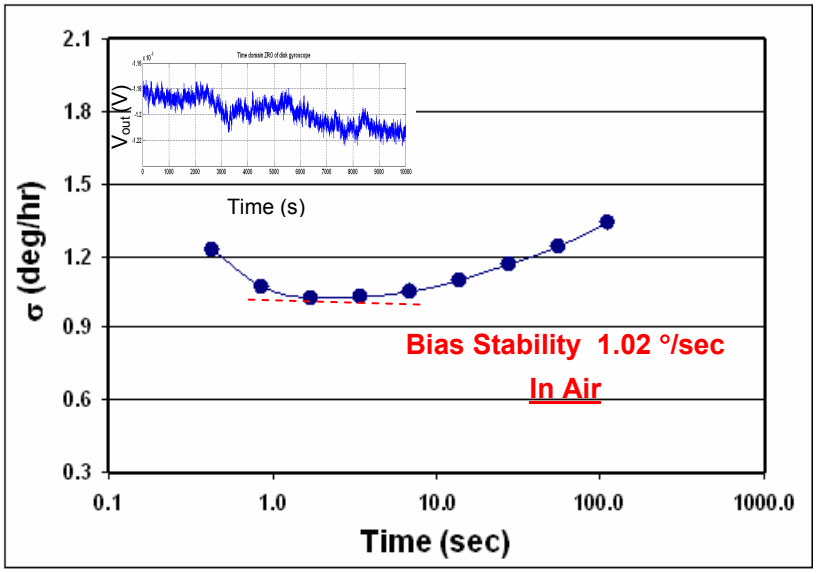

Figure 5-33: Root Allan variance plot of an 800μm diameter disk gyroscope including uniform perforations at zero rate output (ZRO) in air at V_p=12.5V. The inset shows the time domain plot of the ZRO of disk gyroscope.

5.6.3 TEMPERATURE CHARACTERIZATION

A similar prototype device is characterized in air over a 60°C temperature range. The matched-mode operation remained constant over this temperature range. The frequency was found to have a drift with temperature change at a slope of -21ppm/°C, as shown in Figure 5-34a. In addition, the matched-mode Q of this prototype device was characterized in air for the same temperature range. Figure 5-34b demonstrates a reduction of ~6.6% in $Q_{matched\text{-}mode}$ for ΔT of 60°C.

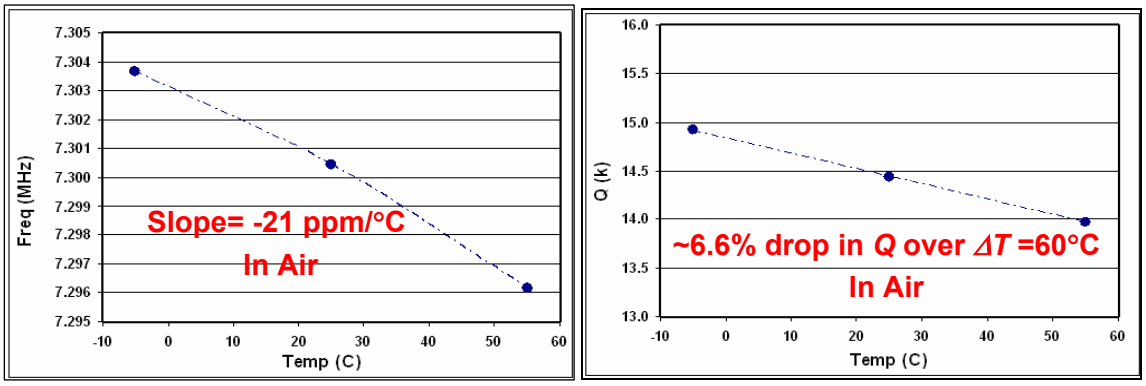

(a) (b)

Figure 5-34: Temperature variation of (a) matched mode frequency (b) matched mode Q in air for an 800µm diameter (100) SCS disk gyroscope including uniform 6µm diameters holes, showing a frequency drift profile with a slope of -21ppm/°C and ~6.6% drop in Q, for ΔT=60°C.

Furthermore, the scale factor is characterized and measured in air at -5°C, 25°C and 55°C, shown in Figure 5-35. The sensitivity declines by 15% over the temperature range of 60°C. It is worth noting that the source voltages (V_p and v_{ac}) are kept constant. The reduction in the sensitivity should track the reduction in the matched mode Q if all other key parameters, such as the source voltages, are kept constant. Since the measured sensitivity was based on driving the device in open-loop configuration, the small variation in the drive amplitude over the temperature was observed. Accordingly, the

drive output and the matched mode Q were recorded for this temperature range. The drive amplitude is then calculated from the the measured drive output. These values are summarized in Table 5-1. If these devices are driven in a closed loop control, the drive amplitude can be maintained constant, resulting in the lower sensitivity reduction due to the temperature change.

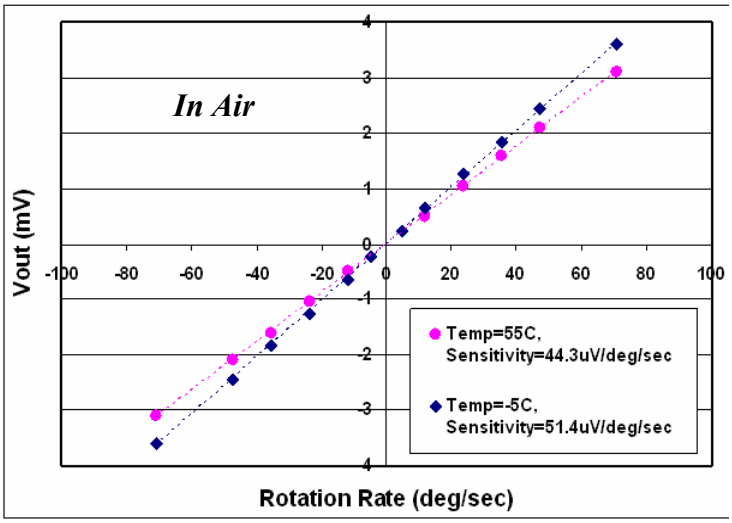

Figure 5-35: The measured rate sensitivity results in air from one sense electrode of an 800µm diameter disk gyroscope including uniform 6µm diameter release holes at T=-5°C and T=55°C with V_p=12.5V and v_{ac}=224mV using discrete electronics.

Table 5-1: The key parameters in temperature characterization of scale factor in air.

Temp (°C)	V_p (V)	q_{drive} (nm)	$Q_{matched\text{-}mode}$ (k)	Sensitivity (µV/°/sec)	
				Measured	Theory
-5	12.5	0.558	14.95	51.4	62.2
49	12.5	0.472	13.972	44.2	49.5

5.7 PERFORMANCE DISCUSSION

The performance specifications for a 1200µm diameter (111) silicon disk and 800µm diameter disk gyroscopes with both nonuniform and uniform release holes are summarized in Table 5-2. As the data show, the measured frequency responses of these devices are within 2% of the ANSYS simulation results. This very small difference can

be readily attributed to slight geometric differences between the fabricated and designed structures.

In addition, the measured rate sensitivity data from 1200μm diameter (111) silicon disk gyroscopes, in 1mTorr vacuum, were ~10% lower than the analytical values. For 800μm diameter devices with nonuniform release holes and with uniform 6μm diameter release holes, the measured sensitivities are ~11.5% and 9% lower than the analytical values for 1mTorr vacuum and in air, respectively. These results also demonstrate very good agreement between theoretical and measured values for scale factor.

Furthermore, the total measured noise for 800μm diameter (100) silicon disk gyroscopes with nonuniform and uniform 6μm diameter release holes are ~1.6× and ~1.3× less than the theoretical values, respectively. However, the measured noise in a 1200μm diameter (100) silicon disk gyroscope with nonuniform release holes is ~1.3× lower than the theoretical value in 1mTorr vacuum. This difference might be due to unexpected environmental noise during the 24-hour ZRO recording period.

It is worth noting that all the measured results are taken from devices operating in open-loop configurations, with discrete-based interface circuitry fed by only a single sense electrode. If all available sense electrodes are coupled, and a fully differential, IC-based architecture is used, the BAW gyroscopes' performances can be improved substantially (i.e. ~6×). If a closed-loop drive configuration is employed, the stability of these devices can be improved significantly by maintaining the drive amplitude constant while varying the temperature and environmental conditions.

Table 5-2: The performance specifications for BAW gyroscopes.

Device Parameters	(111) SCS	(100) SCS	
	Non-uniform Perforated Disk (in 1mTorr Vacuum)	Non-uniform Perforated Disk (in 1mTorr Vacuum)	Uniform Perforated Disk (in Air)
Operating frequency (MHz)	ANSYS 2.93	ANSYS 6.12	ANSYS 7.48
	Measured 2.917	Measured 5.95	Measured 7.30
Device diameter (μm)	1200	800	800
Device thickness (μm)	35	40	40
Capacitive gap (nm)	180	200	200
Polarization voltage (V)	10	13.2	12.5
Measured Q	65,810	235,810	14,435
Angular gain (A_g)	0.4584	0.2314	0.2314
Measured drive amplitude (nm)	7.66	5.19	0.70
Voltage Gain (A_v)	23.2	23.2	720
I_{noise} (pA/√Hz)	2.54	2.54	2.54
R_f (Ω)	33,000	33,000	33,000
Sensitivity (μV/°/sec)	Theoretical 359	Theoretical 293	Theoretical 69.0
	Measured 320	Measured 267	Measured 64.5
Total noise (°/sec /√Hz)	Theoretical 0.0060	Theoretical 0.008	Theoretical 0.86
	Measured 0.0047	Measured 0.021	Measured 0.95
Bias Instability	17 °/hr	77 °/hr	0.95 °/sec

5.8 SUMMARY

A number of perforated disk gyroscopes, as designed in chapter 3, were implemented and operated in their both primary and secondary elliptic modes in, respectively, (111) SCS

and (100) SCS substrates. Among these, the measurement results for 800μm-diameter devices, fabricated on 40μm thick (100) SOI substrates, with non-uniform release holes and uniform 6μm diameter perforations are presented in this Chapter. First, the frequency responses of the elliptic degenerative modes are investigated to identify their quality factors (Q) as well as frequency separation (Δf) between drive and sense modes. The tuning method, as stated in the first part of this paper, is applied to electrostatically tune and match the two degenerative modes. Afterwards, the performance parameters, *i.e.* scale factor and bias instability, were measured for matched-mode operation in 0.1mTorr vacuum and at atmospheric pressure.

The prototype BAW gyroscopes show ultra high quality factors in excess of 150,000 and 14,000 in vacuum and air, respectively. The high frequency of the modes results in a large device bandwidth (from 30Hz to 400Hz) under very high-Q matched-mode condition. For an 800μm-diameter device with non-uniform perforations, the rate sensitivity in vacuum was measured to be 270μV/°/sec, along with a $Q_{matched\text{-}mode}$ of 235,000. However, for an 800μm-diameter device with uniform 6μm diameter holes in air, the scale factor was measured to be 65μV/°/sec, with $Q_{matched\text{-}mode}$ of 14,400.

In addition, these devices were characterized over a typical consumer electronics temperature range of -5°C to 55°C. It was observed that the frequency separation between two modes remained constant and the modes remained matched. Furthermore, the Q and scale factor of these prototypes devices were found to decrease ~6% and ~15% over this temperature range. The measured results demonstrate the high performance stability of BAW gyroscopes even at elevated temperature.

CHAPTER 6

MULTI-AXIS BAW SILICON GYROSCOPE

6.1 OVERVIEW

To date, commercialized multi-axis vibrating gyroscopes [14, 15] have utilized multiple proof masses for detecting rotation rates around multiple axes. Consumer applications require stable, high-performance multi-axis gyroscopes with small form factor, fast response time and high shock survivability. This set of attributes is widely unavailable at low cost in current low frequency vibrating gyroscopes, and can be well served by bulk acoustic wave (BAW) silicon gyroscopes. In an effort to meet these demands, the original *z*-axis design has been developed that enables measurement of rotation rate around the *x* or *y* axes, without utilizing additional disks. This novel approach eliminates the issues with integration of multiple proof masses, resulting in the smallest form factor.

The multi-axis gyroscopes introduced here, operating in the frequency range of 1 to 8MHz have large frequency bandwidth (10-30Hz) and superior shock tolerance. Due to their high frequency of operation, these devices also show reduced susceptibility to common damping mechanisms. This gives them very high, thermally-stable quality factors without the typically required high vacuum environment, and the associated packaging, manufacturing, and reliability complications.

This chapter introduces design and implementation of a capacitive gyroscope capable of sensing rotation rates around *x* and *z*-axes. We present an 800μm-diameter multi-axis disk gyroscope implemented in thick (100) silicon-on-insulator (SOI) substrate. A single

disk is operated separately in out-of-plane and in-plane modes, whose Coriolis coupling allows measurement of rotation rates around the in-plane and out-of-plane axes. The revised high aspect-ratio poly- and single crystalline silicon (HARPSS) fabrication process was used to implement the disk gyroscopes in 40μm thick SOI substrates. Very small gap sizes of 200nm are provided for both in-plane and out-of plane capacitive transduction sites. With vibration amplitudes less than 20nm in all directions, high frequency disk gyroscopes are semi-stationary devices requiring very small DC and AC actuation voltages.

6.2 PRINCIPLE OF OPERATION

As schematically shown in Figure 6-1, the Coriolis-based high frequency multi-axis gyroscope consists of a center-supported disk structure with capacitively-coupled in-plane and out-of-plane drive, sense and control electrodes [111]. To measure rotation rate around the *x* or *y* axes, the disk's degenerative out-of-plane modes are excited. This requires in-plane electrodes around the perimeter of the resonating disk structure. Also, using only a single disk to potentially measure rotation rate around *x*- and *z*-axes necessitates compatible electrodes for in-plane and out-of plane transduction. To achieve this, out-of-plane electrodes in *z*-axis BAW gyroscopes are extended over the disk to form the in-plane electrodes. The capacitive gap between the in-plane electrodes and the disk is ~200nm, the same as the gap between the out-of-plane electrodes and the disk. In order to isolate in-plane electrodes from out-of-plane electrodes, and significantly reduce any parasitic coupling, a 2μm gap is designed between these electrodes.

Similar to *z*-axis BAW gyroscopes, the capacitive multi-axis BAW disk gyroscope is supported by a small island of buried oxide layer (BOX), shown in Figure 6-1. The symmetry of the structure guarantees that the support is self-aligned to the center of the disk during the BOX etch step. Boron-doped polysilicon traces attached at the center of the disk, to which they are self-aligned, provide a DC bias voltage to the disk. In addition, to implement these devices in SOI, release holes are added to the disk (though not shown in Figure 6-1).

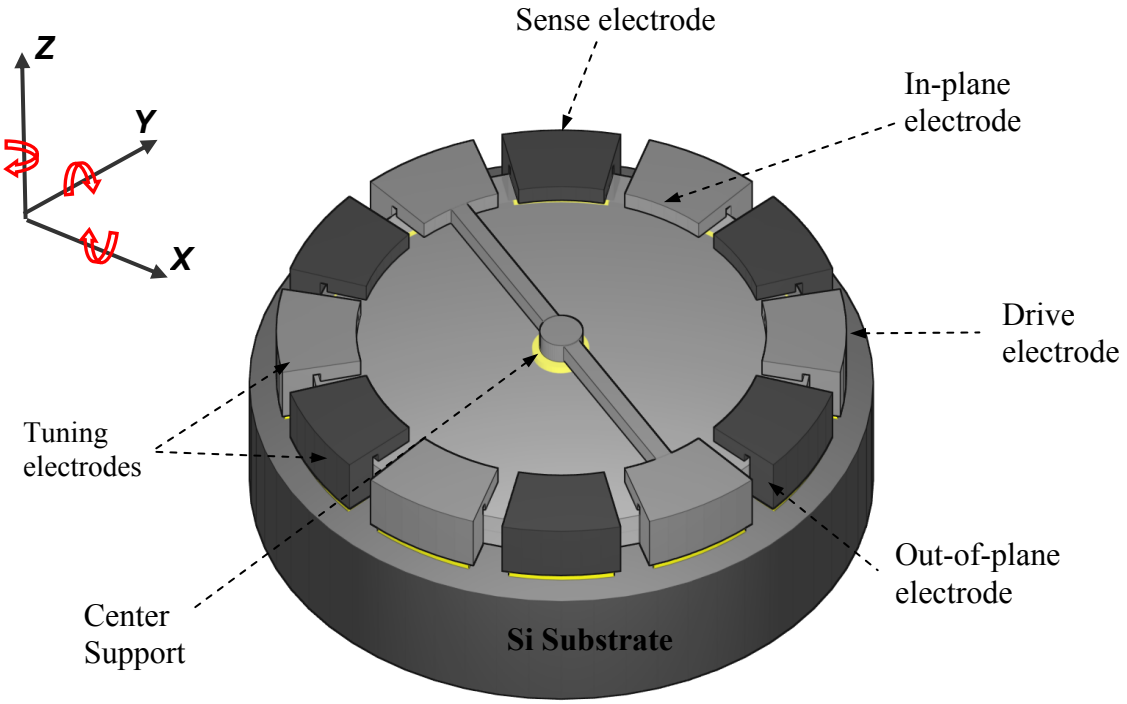

Figure 6-1: Schematic diagram of high frequency multi-axes disk Gyroscope in (100) silicon.

To actuate the capacitive BAW disk gyroscopes in their out-of-plane modes, an AC signal at the selected resonant frequency is applied to a drive electrode, along with the application of DC bias to the disk itself. While the disk is driven in its first degenerative out-of-plane mode, the gyroscope is rotated around one of the in-plane axes (*i.e. x*-axis or *y*-axis). Coriolis acceleration transfers energy between the two out-of-plane degenerative

modes. As energy builds up in the second mode, output current is created at the sense electrode. An interface circuit amplifies, demodulates and filters the sense current to yield the rotation-induced Coriolis signal.

6.3 DESIGN OF MULTI-AXIS (100) SCS DISK

To design a multi-axis disk gyroscope implemented in (100) silicon wafers as an extension of a single-axis gyroscopes, a set of design rules should be considered which will be discussed in this section. First, the out-of-plane mode shapes should be compatible with the in-plane mode shapes to enable operation of both modes in a same disk. Second, the cross talk sensitivity between the two in-plane rotation rate (Ω_x and Ω_y) should be avoided.

To address the former, the anti-node lines of both in-plane and out-of-plane modes should be the aligned to allow the existence of compatible perforations and electrodes in a single disk. It is worth noting that in multi-axis BAW gyroscopes, fabrication limits prevent the disk from having perforations underneath the in-plane electrodes. In addition, perforations in the disk should be carefully designed to ensure the minimum frequency separations between the in-plane degenerative modes and between the out-of plane degenerative modes. Also, the in-plane electrodes need to be located at anti-node lines of the out-of-plane modes to provide the large transduction area. These requirements limit the out-of-plane modes to have the same spatial symmetry as the in-plane mode. Due to the anisotropic nature of (100) SCS, only the high-order out-of plane modes are compatible with the secondary elliptical in-plane modes, which exhibit 30º spatial symmetry.

A further constraint on the choice of out-of-plane modes comes from the need for independent measurement of rotation rates around *x*- from *y*-axis. In order to eliminate the cross-sensitivity between *x*-axis and *y*-axis rotations, each in-plane sensing axis must coincide with the node-line of one mode and anti-node line of the other mode. For instance, to measure the applied *x*-axis rotation rate, the anti-node of the drive mode must coincide with the *x*-axis while the node-line of this mode is aligned with *y*-axis. When the rotation rate around the *x*-axis is applied, the energy transfers from the drive mode to sense mode and sense mode at *y*-axis is excited due to the Coriolis effect. In this case, with the simultaneous application of *y*-axis rotation rate, there will be no transfer of energy from the drive mode to the sense mode since the node-line of the drive mode is placed at *y*-axis. Thus, the proposed design will distinguish the in-plane rotation rates from each other. A similar method can be employed to measure the applied *y*-axis rotation rate.

A number of disk structures with a variety of perforation arrangements are designed to operate in their degenerative out-of-plane and in-plane modes. Two major categories of release hole configurations were designed. In both categories, the perforations ultimately form equally-spaced concentric rings of holes, and produce structures that are symmetric about the *x* and *y* axis. The first category places holes of non-uniform diameter along radial lines of the disk, with the radial lines aligned to the node-lines of both the in-plane and out-of plane mode shapes. This entails radial lines located every 30° or 15°. The second category incorporates uniform-sized holes of smaller size and higher density.

ANSYS simulations results, shown in Figure 6-2, demonstrate suitable degenerative out-of plane and in-plane modes for an 800μm diameter disk with nonuniform holes in 40μm

thick (100) silicon substrate. The high-order degenerative out-of-plane modes for this device occurred at 1MHz with a frequency separation of <100Hz. However, the second elliptic in-plane modes of this device were observed at 6MHz with a frequency split of ~1kHz. The larger frequency separation seen for the in-plane modes is attributed to the release holes being placed away from the disk edges, due to the in-plane electrodes.

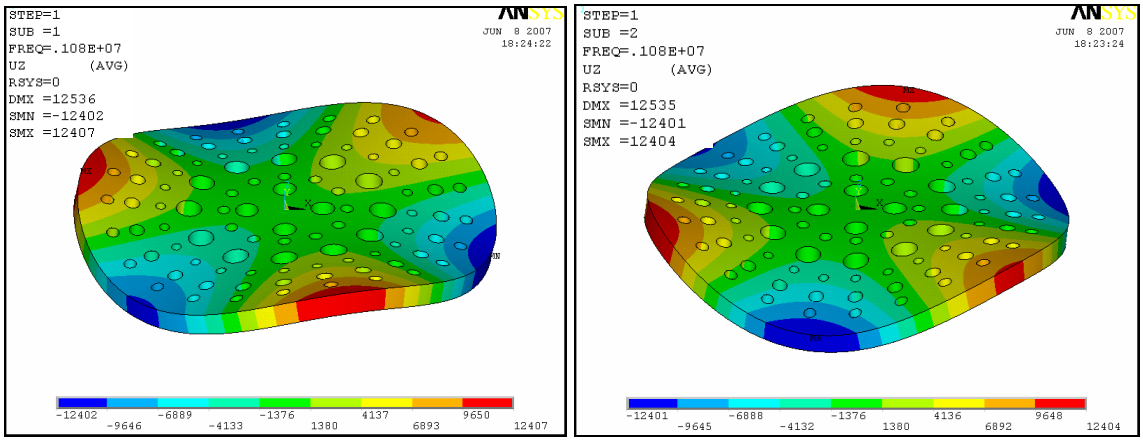

(a)

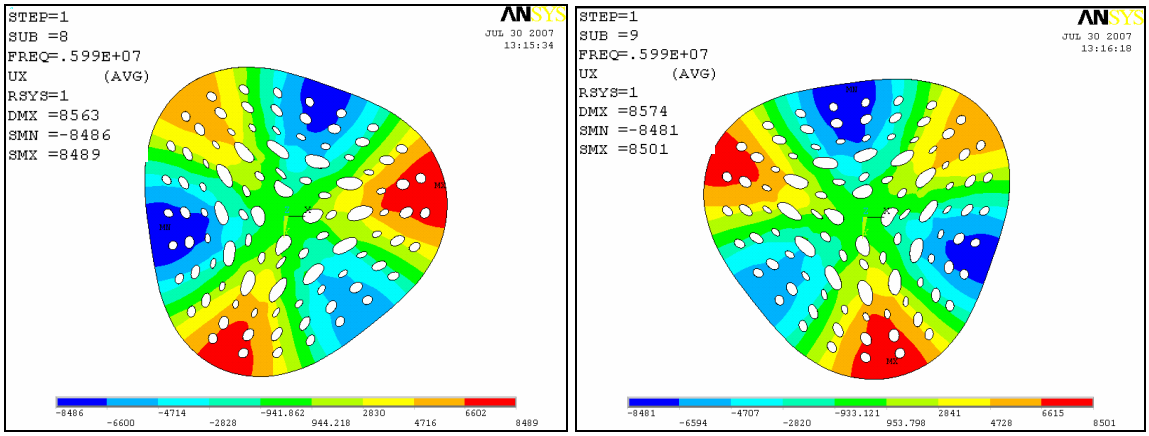

(b)

Figure 6-2: ANSYS simulations of an 800µm diameter 40µm-thick (100) Si disk structure with non-uniform sized release holes: (a) two degenerative out-of plane modes at 1MHz; (b) two degenerative in-plane modes at 6MHz. Both modes are spatially 30° apart.

To study the effect of the disk perforations on the frequency splits between in-plane degenerative modes and between out-of-plane degenerative modes, finite element

modeling is employed. A variety of uniform hole sizes were designed and simulated in ANSYS, as shown in Figure 6-3. As expected, the disks with uniform smaller release holes exhibit smaller frequency splits. This is because the frequency behavior of disk with uniform small holes more closely mirrors that of the solid disk. For a 6μm diameter uniform release holes in an 800μm diameter disk in 40μm thick (100) silicon, ANSYS simulation indicates a frequency split of 30Hz between degenerative out-of-plane modes and a frequency split of 110Hz between degenerative in-plane modes (Figure 6-4).

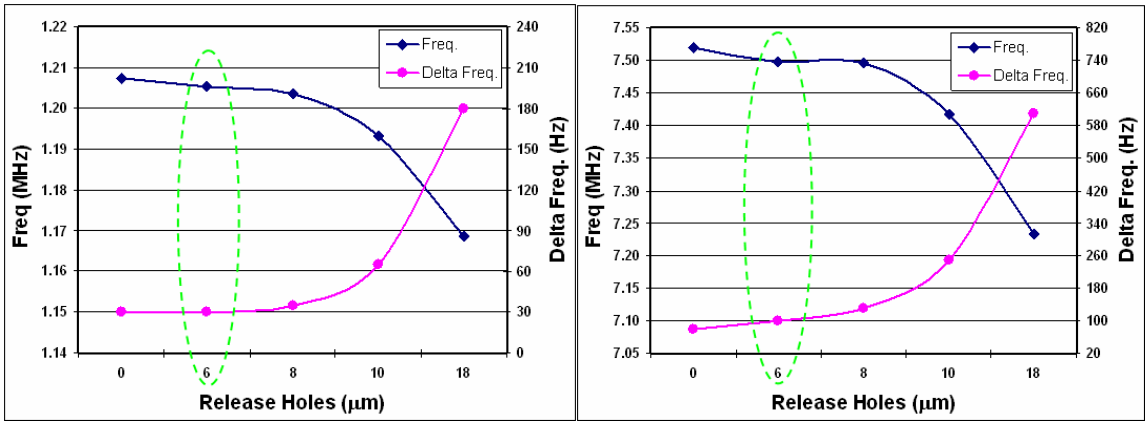

(a) Out-of-plane modes (b) In-plane modes

Figure 6-3: ANSYS simulation results of secondary elliptic in-plane and out-of plane modes in 800μm diameter disk gyroscopes in 40μm thick (100) silicon, showing the effect of release hole sizes on the frequency splits between two modes and on the operating frequencies.

It is worth noting that 50,000 elements were used for all ANSYS models. This large number was chosen to minimize the simulation errors on the frequency split values. Also, the distance between the holes at the center of the disk needs be large enough to ensure the buried oxide at the center of the disk survives the release etch. The center post diameter is designed to be at most one twentieth of the disk diameter to minimize the losses through support [74, 75] and to enhance the *Q* of the device.

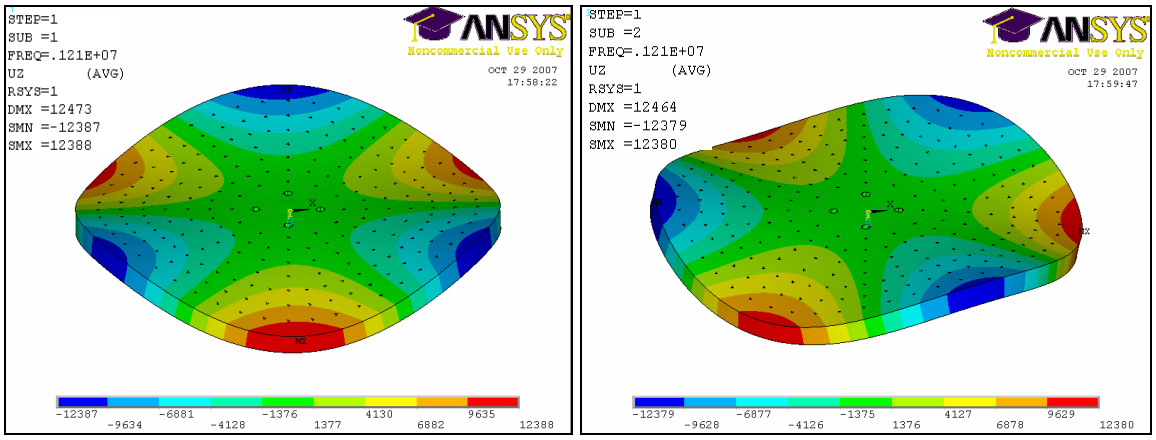

(a)

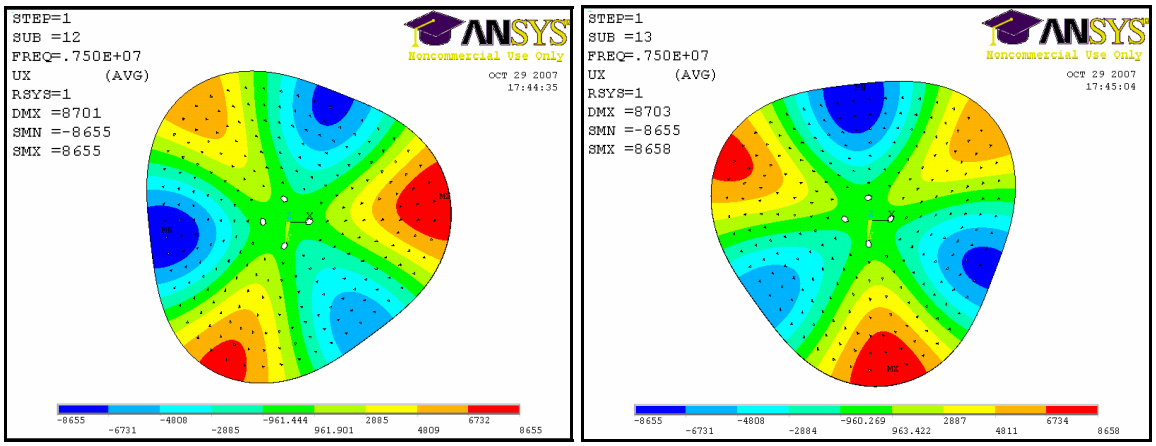

(b)

Figure 6-4: ANSYS simulations of an 800µm diameter 40µm-thick (100) Si disk structure with uniform 6µm diameter release holes: (a) two degenerative out-of plane modes at 1.2MHz with Δf=30Hz; (b) two degenerative in-plane modes at 7.5MHz with Δf=100Hz. Both modes are spatially 30° apart.

6.4 Out-of Plane Mode Shape Equations

In general, the displacement of a linear elastic body can be expressed as a linear combination of its normal mode shape functions and its amplitudes [80]. For a disk gyroscope, operating in its degenerative out-of-plane modes, the vibration displacement of each point on the disk is a summation of both degenerative mode displacements, as stated in (6-1).

$$
\begin{aligned}
u_r &= q_1\phi_{r1} + q_2\phi_{r2} \\
u_\theta &= q_1\phi_{\theta 1} + q_2\phi_{\theta 2} \\
u_z &= q_1\phi_{z1} + q_2\phi_{z2}
\end{aligned}
\tag{6-1}
$$

Where q_1 and q_2 are the drive and sense amplitudes and ϕ_r, ϕ_θ and ϕ_z are respectively the radial, circumferential and axial mode shape functions.

It is worth nothing that radial displacement for out-of-plane mode shapes is nearly zero and only the circumferential and axial displacements should be considered for this mode shape. The out-of-plane mode shape functions in circumferential and axial displacements are expressed in (6-2).

$$
\begin{aligned}
\phi_{\theta 1} &= U_\theta \cos(m\theta) \qquad \phi_{\theta 2} = -U_\theta \sin(m\theta) \\
\phi_{z1} &= U_z \sin(m\theta) \qquad \phi_{z2} = U_z \cos(m\theta)
\end{aligned}
\tag{6-2}
$$

Where U_θ and U_z are the normalized displacements in the tangential and axial directions and m is the mode number and m=3 for the out-of-plane mode shapes used in the work. The normalized displacements for a disk vibrating in its flexural out-of-plane modes are stated in (6-3) from [112].

$$
\begin{aligned}
U_\theta &= \frac{R^2}{k}\frac{m}{r} J_m\left(\frac{kr}{R}\right)\cos\left(\chi\frac{z}{R}\right) \\
U_z &= -\frac{R\chi}{k} J_m\left(\frac{kr}{R}\right)\sin\left(\chi\frac{z}{R}\right)
\end{aligned}
\tag{6-3}
$$

The normalized displacements are expressed in terms of Bessel functions of the first kind (J_m) as well as trigonometric functions. Also, k and χ are related to each other from (6-5).

$$\chi^2 = \frac{(1-2\nu)(1+\nu)}{(1-\nu)} \frac{{\omega_0}^2 \rho R^2}{E} - k^2 \tag{6-4}$$

Where R and ω_0 are respectively the disk radius and the natural angular frequency; However ρ, E and υ are respectively the mass density, the Young's modulus and the Poisson ratio.

Given disk thickness (h) and disk radius (R) as well as the operating frequency (ω_0) and material properties of the disk (E, ρ, ν), k can be solved by trial and error from (6-5):

$$\left(k^2 - \beta^2\right)^2 \tan\left(\frac{\chi h}{2R}\right) + 4\beta\chi k^2 \tan\left(\frac{\beta h}{2R}\right) = 0 \tag{6-5}$$

In which χ and β can be respectively substituted from (6-4) and (6-6).

$$\beta^2 = \frac{2(1+\nu){\omega_0}^2 \rho R^2}{E} - k^2 \tag{6-6}$$

After evaluating the k by numerical solution from (6-5), χ can be determined from (6-4) and both k and χ will be replaced into (6-3). As a result, the normalized displacements and subsequently the mode shape functions are fully identified. Given the mode shape functions as a function of r, θ and z, the effective mass (M) and Coriolis coupling (γ) can be evaluated respectively from (6-7) and (6-8) by integrating these mode shapes over the disk volume (V).

$$M = \oint \rho\left(\phi_{z1}{}^2 + \phi_{\theta 1}{}^2\right) dV \tag{6-7}$$

$$\gamma = \oint \rho\left(\phi_{z1}\phi_{\theta 2} - \phi_{z2}\phi_{\theta 1}\right) dV \tag{6-8}$$

Next, the angular gain can be estimated for the disk while operating at its out-of-plane mode using (3-41). Furthermore, the sensitivity of the multi-axis disk gyroscopes due to the in-plane applied rotation rate (Ω_x or Ω_y) can be analyzed in the similar method as expressed in Chapter 3 for the single-axis disk.

6.5 FABRICATION

The fabrication process flow for the high-frequency multi-axis disk gyroscopes developed in this work is shown in Figure 6-5. This process is similar to the fabrication process flow for *z*-axis BAW gyroscopes. The process starts with growth and patterning a 2μm thick silicon oxide layer. The in-plane electrodes, perforations and center anchor are patterned in this first mask, to be self-aligned with the disk. Then the trenches are etched only around the disk and at the release holes. LPCVD silicon oxide is grown at 950°C to form the capacitive in-plane and out-of plane gaps. Then, LPCVD polysilicon are deposited (at 588°C and 250mTorr with 100sccm SiH_4) and the trenches are refilled. After etching polysilicon on the surface, the SACOX is patterned and removed everywhere except around the disk and release hole edges and on the in-plane electrode area. This 200nm thick SACOX is protected on the surface to define the out-of-plane gaps between the disk and in-plane electrodes. Next, the second LPCVD polysilicon layer is deposited, boron-doped and annealed.

The polysilicon is patterned on the surface to form the poly traces, in-plane electrodes, and pads. Afterwards, the polysilicon as well as part of silicon substrate are etched inside the trenches, followed by a final release in hydrofluoric acid (HF).

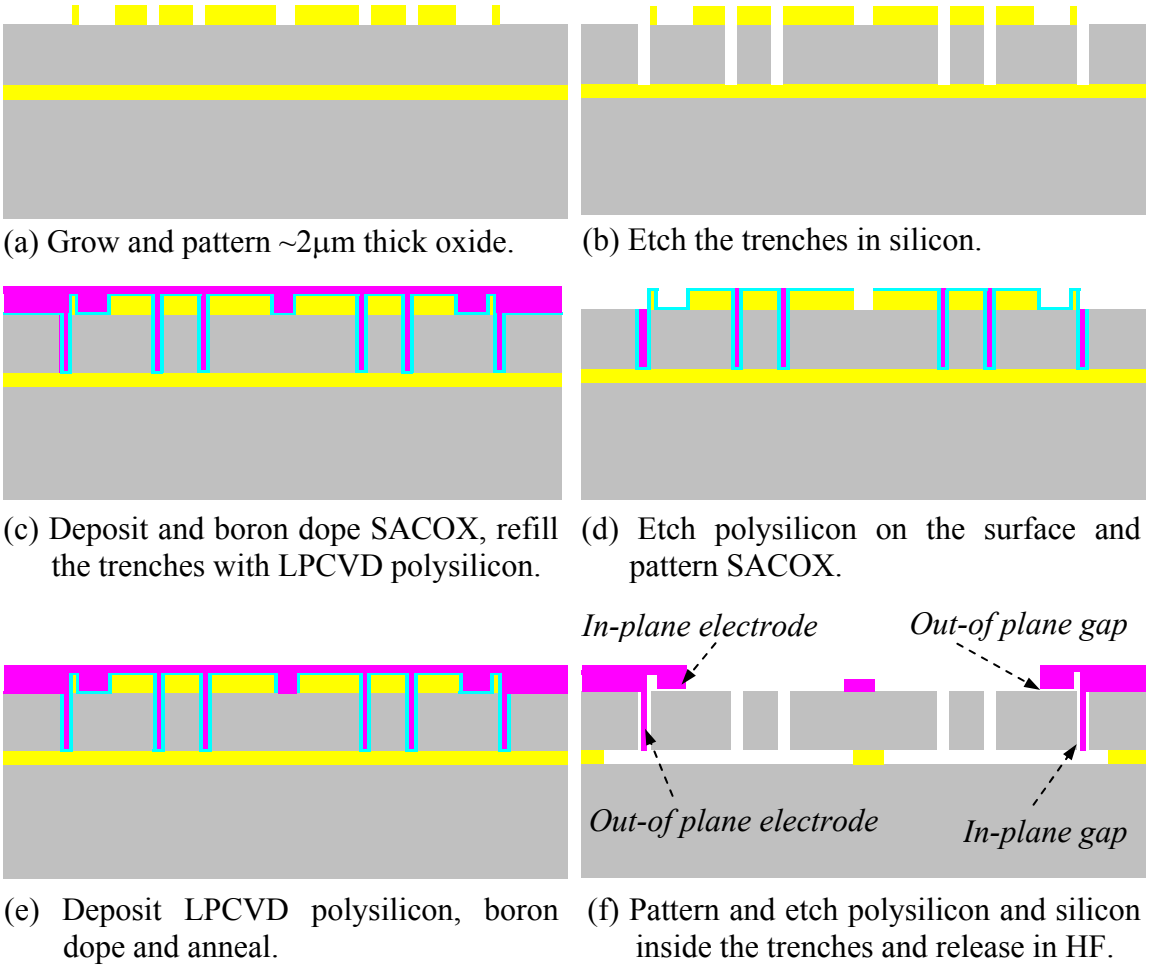

(a) Grow and pattern ~2μm thick oxide.

(b) Etch the trenches in silicon.

(c) Deposit and boron dope SACOX, refill the trenches with LPCVD polysilicon.

(d) Etch polysilicon on the surface and pattern SACOX.

(e) Deposit LPCVD polysilicon, boron dope and anneal.

(f) Pattern and etch polysilicon and silicon inside the trenches and release in HF.

Figure 6-5: Fabrication process flow for multi-axis single-disk gyroscopes in SOI substrates.

The key difference between multi-axis and single-axis disk gyroscopes is that the poly electrodes are extended over the disk (typically 20-50μm) to form in-plane electrodes for driving and sensing the out-of-plane modes. The capacitive gap between the in-plane electrodes and disk is the same as the vertical gap, typically 200nm. The in-plane

electrodes are co-implemented with out-of plane electrodes using a connector section with large gaps of 2.5μm gap at the edge of the disk.

6.6 MEASUREMENT RESULTS

A number of high frequency multi-axis disk gyroscopes were fabricated in thick (100) SOI wafers using the revised HARPSS process. Figure 6-6 shows a SEM view of a center-supported multi-axis disk gyroscope implemented in (100) SCS. The SEM view of the in-plane and out-of-plane electrode area with 200nm capacitive gaps is shown in Figure 6-6.

To excite in-plane and out-of plane modes, a sinusoidal drive signal was applied to a single drive electrode. The output signal was monitored at a sense electrode located 90° away from the drive electrode. The frequency response of the out-of-plane modes, and *x*-axis rotation response were measured for a variety of thick (100) silicon disk gyroscopes. Unlike in-plane degenerative modes, out-of-plane modes possess frequency response that depends on the thickness of resonating disk. As ANSYS simulations show, thicker disks operate at higher frequency in their out-of-plane modes. In this section, the measurement results for 60μm and 40μm thick (100) silicon devices are presented.

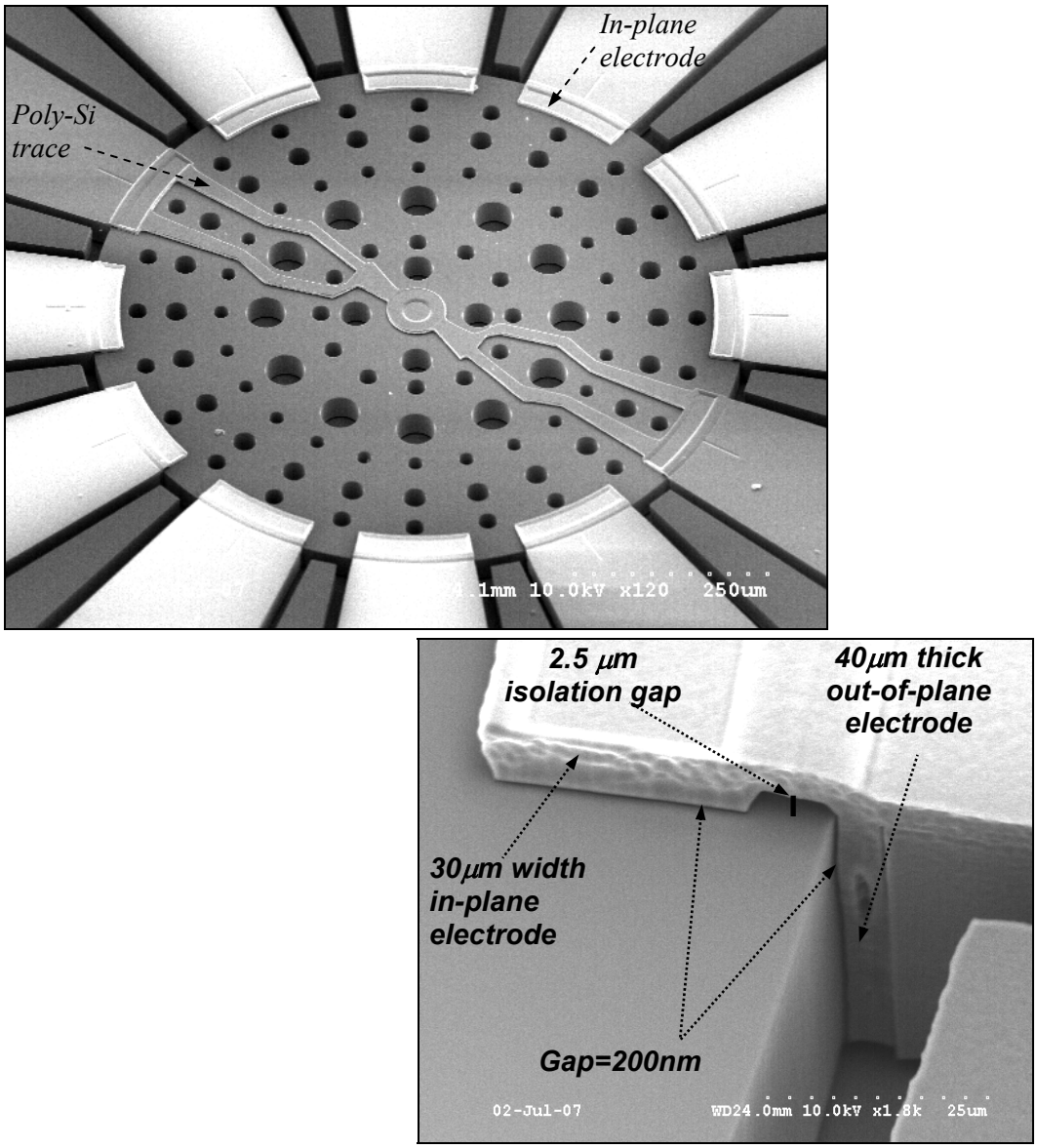

Figure 6-6: SEM view of an 800μm diameter (100) multi-axis silicon disk gyroscope. The poly trace on top provides DC bias to the center of the disk. The close-up SEM view shows the in-plane and out-of plane electrode area with 200nm capacitive gap.

6.6.1 RESULT OF 60μM THICK (100) SCS DISK

An 800μm diameter disk gyroscope implemented in 60μm thick (100) SCS substrates was characterized and the results are presented here. The out-of-plane modes of this gyroscope were observed at 1.5MHz (as predicted by ANSYS) with a frequency split of 32Hz, as shown in Figure 6-7. The measured *Q*'s of a 60μm thick device, before

balancing, were recorded to be 70,000 and 62,000 in 1 mTorr and 1 Torr vacuum, respectively.

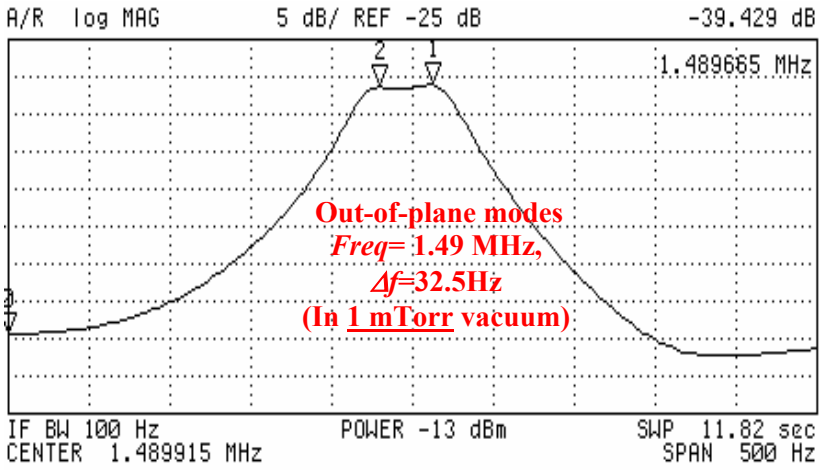

Figure 6-7: The out-of-plane modes of an 800μm diameter (100) SCS disk gyroscope (60μm thick) at 1.5MHz in 1mTorr vacuum with Δf=32Hz and V_p=9V.

The small initial frequency separation of 32Hz between the drive and sense modes of this device was completely eliminated by the application of proper voltages to the tuning electrodes. The matched-mode quality factor of the device was found to be 72,000, as shown in Figure 6-8. At 1Torr, the corresponding matched mode measured Q was 62,000.

The zero rate output (ZRO) of the prototype gyroscope is recorded after balancing the two modes, shown in Figure 6-9 (a). As expected, the sense signal is 90^o out of phase with the drive signal. The sensor output voltage was measured for various rotation rates around the x-axis. The demodulated rotation response to the applied 75°/sec x-axis rotation rate was measured and shown in Figure 6-9 (b).

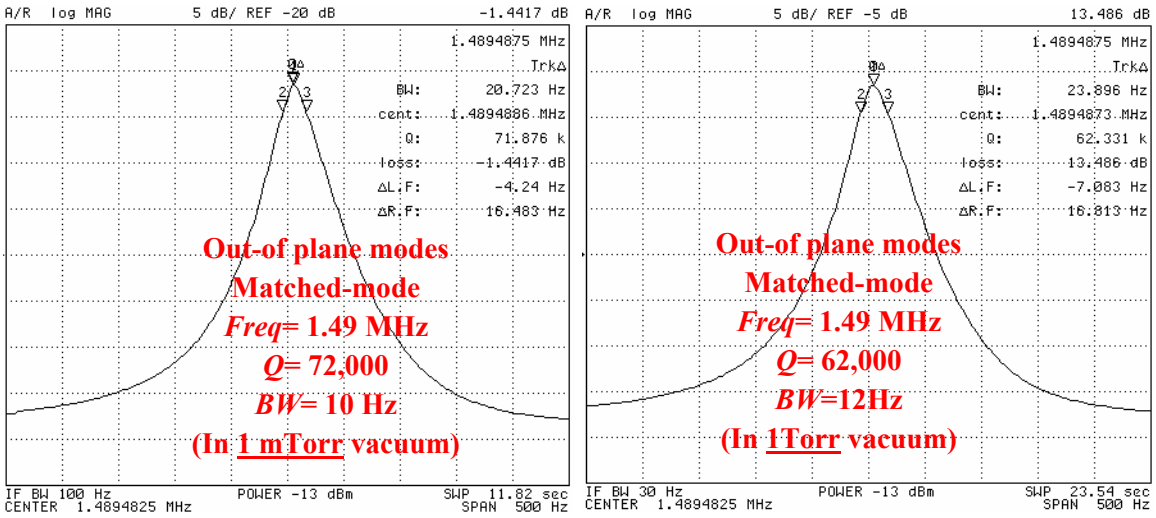

(a) (b)

Figure 6-8: The matched out-of-plane modes of an 800μm diameter (100) SCS disk gyroscope (60μm thick) at 1.5MHz with V_p=11V: (a) In 1mTorr vacuum; (b) In 1Torr vacuum.

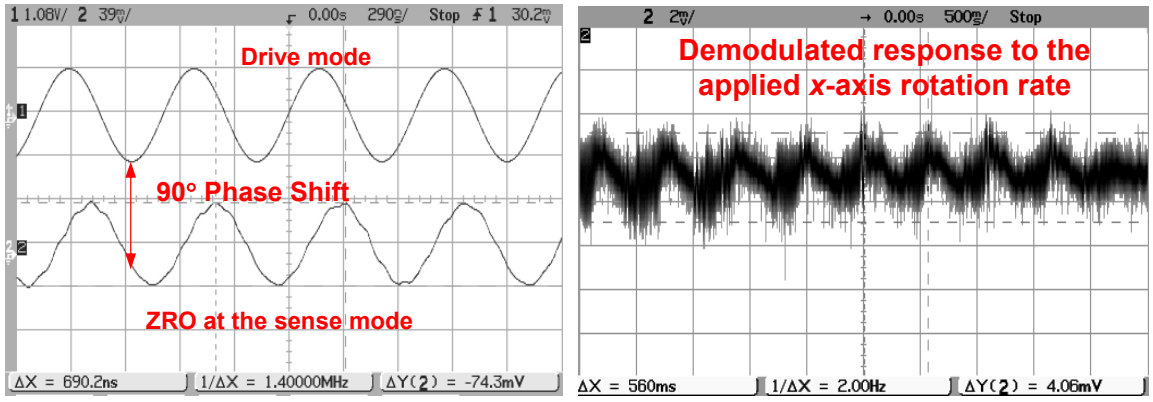

(a) (b)

Figure 6-9: (a) Zero rate output of the prototype gyroscope (b) Rotation response of 60μm thick multi-axis disk gyroscope to the applied 75°/sec *x*-axis rotation rate.

6.6.2 Result of 40μm thick (100) SCS Disk

The out-of plane modes of an 800μm diameter disk gyroscope in 40μm thick (100) SCS were observed at 1MHz with nearly matched-mode *Q* of 60,000 1mTorr vacuum, Figure 6-10.

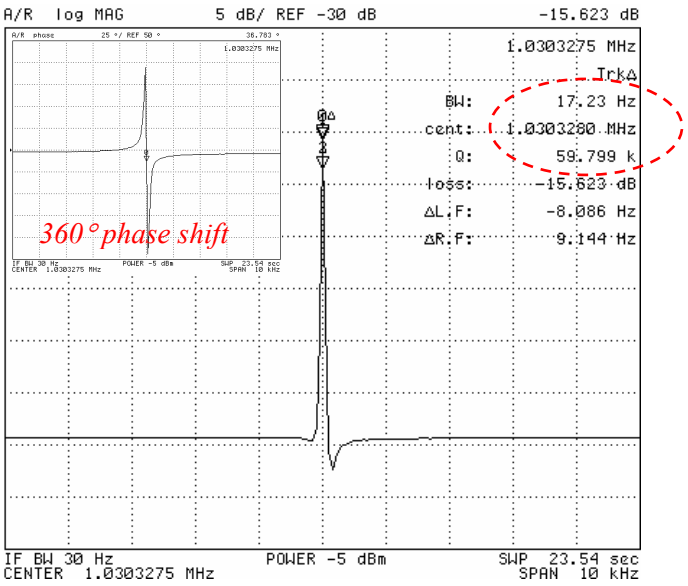

Figure 6-10: The out-of-plane modes of an 800μm diameter (100) SCS disk gyroscope (40μm thick) at 1MHz in 1mTorr vacuum with V_p=3V. The inset shows the phase response for the matched out-of-plane modes.

A very small frequency split of <30Hz was observed without tuning, and the two modes were matched with tuning voltages of only 3.5V. Also, there was a very large quadrature error between the two modes. The other assigned electrodes around the disk were thus utilized to minimize this quadrature error. The frequency response of the matched out-of-plane modes were measured and recorded before and after balancing. A collection of frequency and the time responses are shown in Figure 6-11.

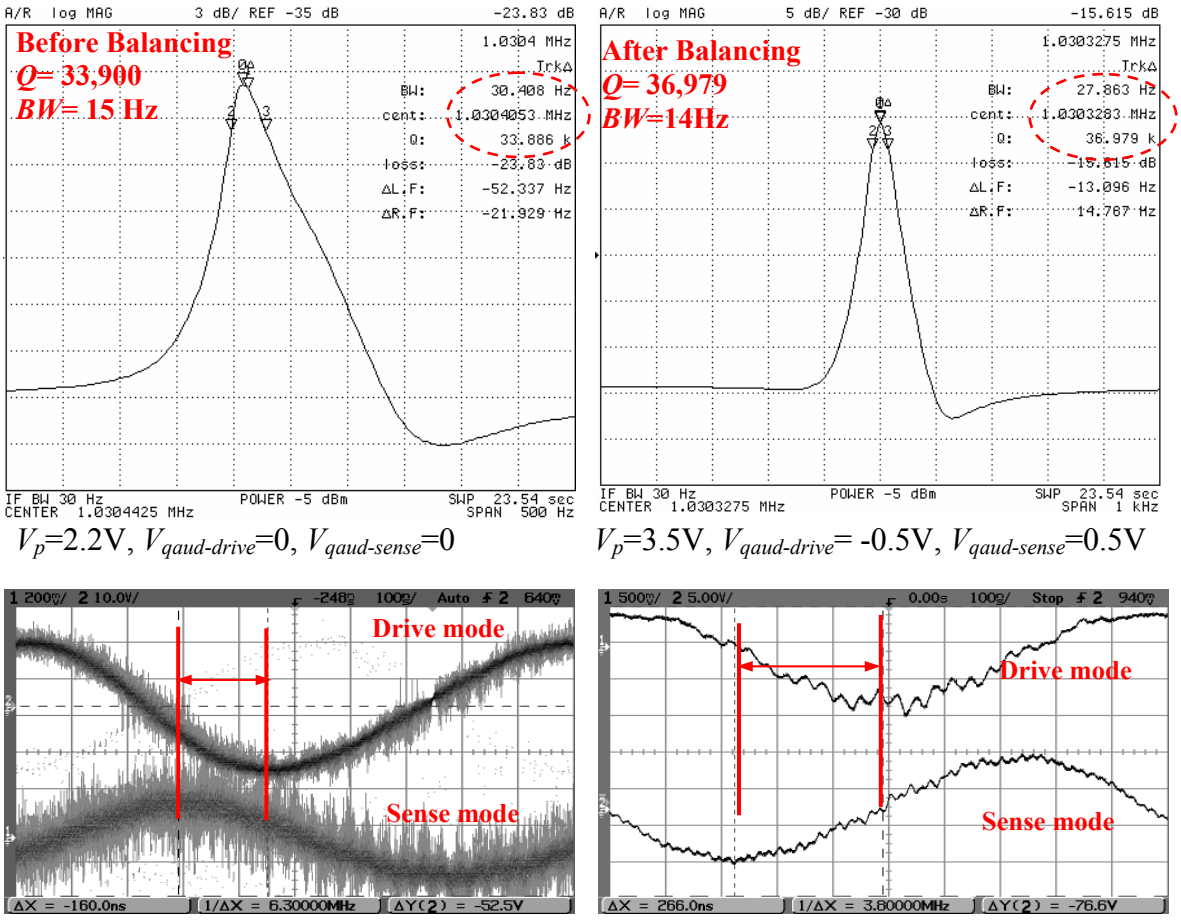

V_p=2.2V, $V_{qaud\text{-}drive}$=0, $V_{qaud\text{-}sense}$=0

V_p=3.5V, $V_{qaud\text{-}drive}$= -0.5V, $V_{qaud\text{-}sense}$=0.5V

126° Phase shift

88° Phase shift

Figure 6-11: Collection of plots showing quadrature cancellation between two out-of-plane modes.

The ZRO of the prototype gyroscope after balancing is shown in Figure 6-12 (a). The bottom trace is the ZRO at the sense electrode and the top trace shows the output of the drive mode. Subsequently, the rotation rate around the *x*-axis was applied to this device and the output signal due to the application of 309°/sec around *x*-axis rotation rate was measured and shown in Figure 6-12 (b). The similar rotation response can be observed when the *y*-axis rotation rate is applied to the device.

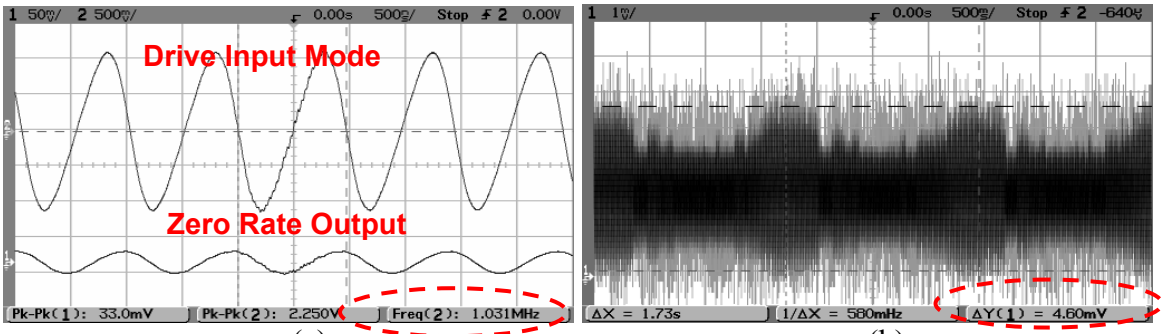

(a) (b)

Figure 6-12: (a) Zero rate output of the multi-axis gyroscope implemented in 40µm thick (100) silicon substrate, (b) Rotation response of an 800µm diameter, 40µm thick multi-axis disk gyroscope to the applied 309°/sec *x*-axis rotation rate.

The sensor output voltage was measured for some applied angular speeds around the *x*-axis. The scale factor was measured from only one sense electrode at matched mode operation after balancing, as shown in Figure 6-13. A sensitivity of 14.1µV/°/sec was measured from the sense mode with V_p=6V.

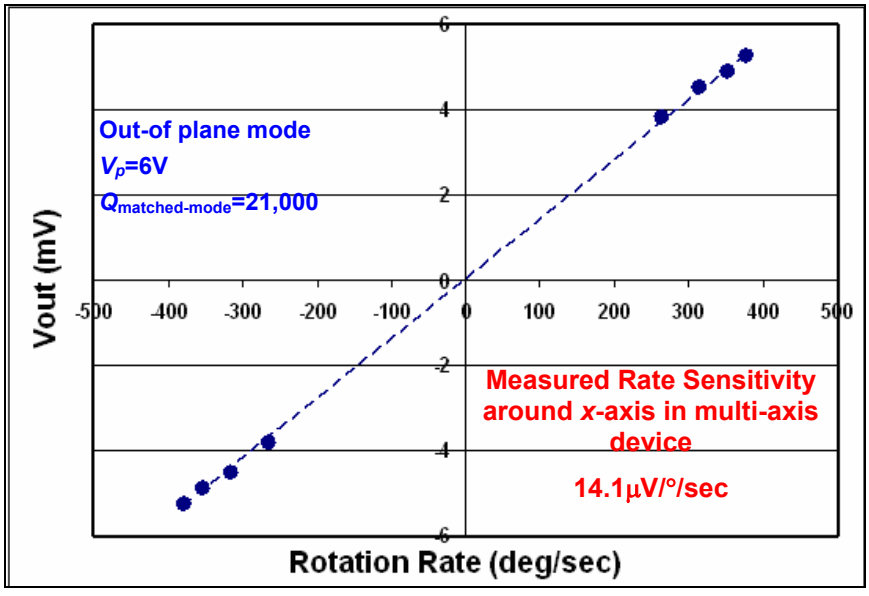

Figure 6-13 : The measured rate sensitivity results from one sense electrode of an 800µm diameter disk gyroscope at matched-mode operation after quadrature cancellation with V_p=6V with discrete electronics.

Furthermore, an identical multi-axis disk gyroscope was operated in *z*-axis sensing mode (using the in-plane modes). Its performance was characterized and is presented here.

The frequency response of this device when operating in its in-plane modes are shown in Figure 6-14. The Q of the drive and sense modes were measured to be 200,000 and 14,000, respectively. Also, the initial frequency separation of 1250Hz was observed between two in-plane modes, which was in good agreement with ANSYS simulation results (from section 6-2). As expected, the multi-axis disks with nonuniform perforations showed large frequency separation between their in-plane degenerative modes.

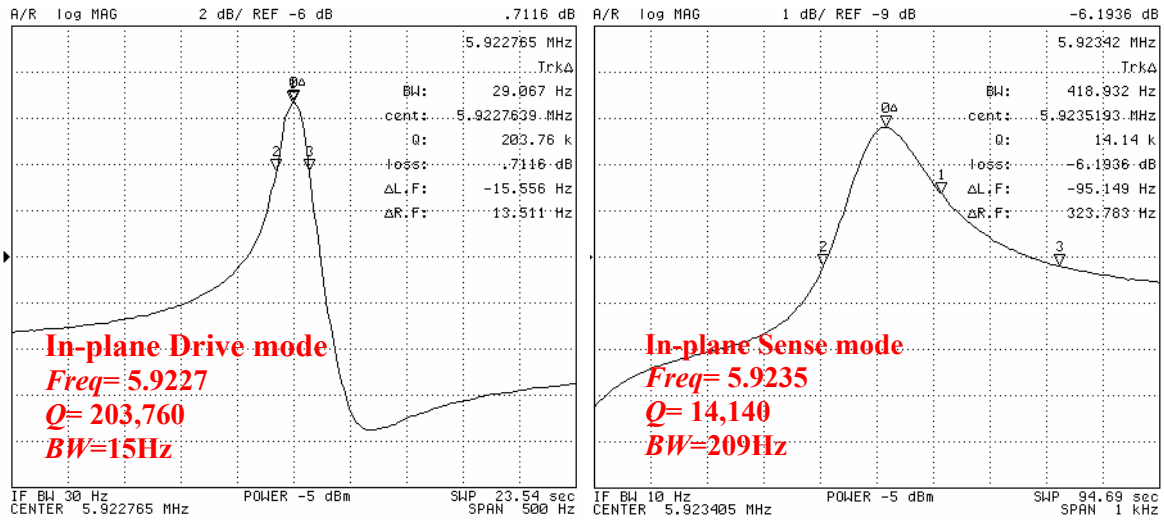

Figure 6-14: The in-plane modes of an 800μm diameter (100) SCS multi-axis disk gyroscope (40μm thick) at 5.92MHz in 1mTorr vacuum with V_p=10V with Δf=1250Hz.

The two in-plane modes of this device were electrostatically tuned and matched using the tuning method discussed in Chapter 3. Given that the frequency of the drive mode is lower than the sense mode frequency (f_{drive}=5.9227 < f_{sense}=5.9235MHz), the tuning voltages of $V_{T\text{-drive}}$>0 and $V_{T\text{-sense}}$<0 were applied to the tuning electrodes. The frequency responses of the modes after the application of optimal tuning voltages are recorded and shown in Figure 6-15. As shown in Figure 6-15, large tuning voltages are required to

match this large frequency split. The multi-axis disk design needs to be further optimized for minimum frequency separations so that lower tuning voltages may be used.

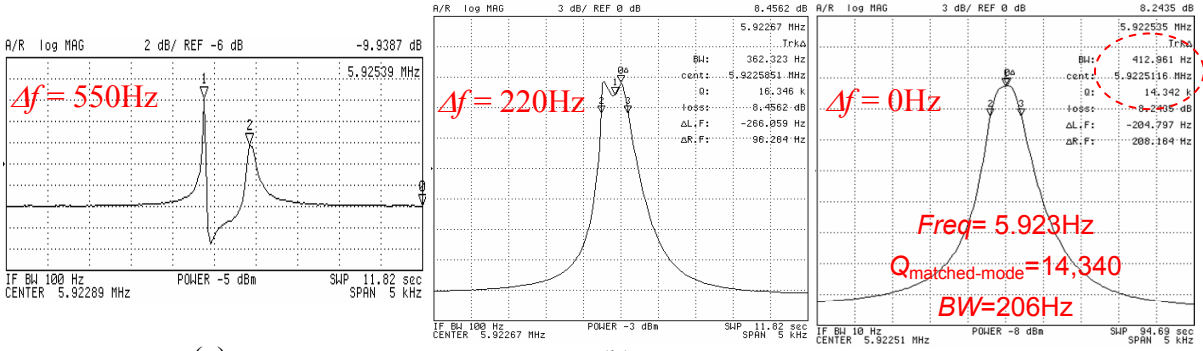

(a) V_p=10V, $V_{T\text{-}drive}$=10V, $V_{T\text{-}sense}$=10 V

(b) V_p=12V, $V_{T\text{-}drive}$=12V, $V_{T\text{-}sense}$= -12 V

(c) V_p=25V, $V_{T\text{-}drive}$=25V, $V_{T\text{-}sense}$= -18 V

Figure 6-15: Collection of plots showing electrostatic frequency tuning and matched-mode of in-plane modes in an 800µm diameter multi-axis disk gyroscope in (100) SCS.

The zero rate output (ZRO) of an 800µm diameter multi-axis disk gyroscope at matched mode was measured and shown in Figure 6-16. The bottom trace is the ZRO at the sense electrode and the top trace shows the output of the drive mode. Also, a phase shift of ~90° is measured between the drive and sense modes.

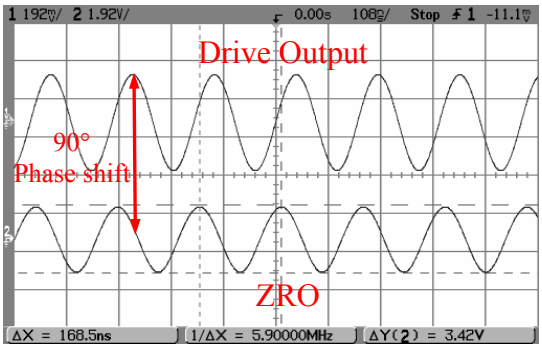

Figure 6-16: Zero rate output of an 800µm diameter multi-axis disk gyroscope at matched-mode in-plane modes.

Subsequently, a number of rotation rates around the *z*-axis were applied to this device and the demodulated output sinusoidal signals were measured. The scale factor is measured from only *one sense electrode*, and the result is shown in Figure 6-17. A measured sensitivity of ~27μV/°/sec was achieved with V_p of 25V and $Q_{matched\text{-}mode}$ of 15,000 in 1mTorr vacuum, as shown in Figure 6-17.

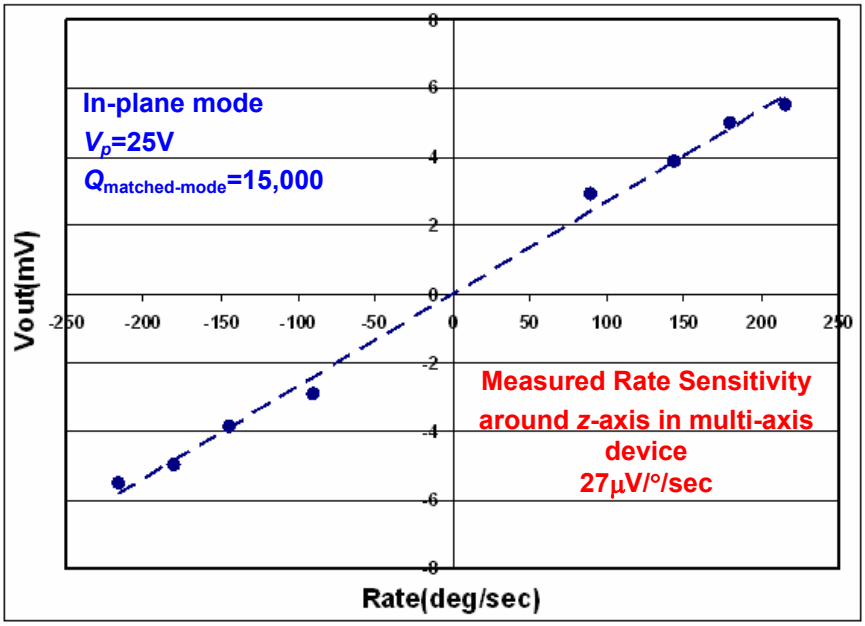

Figure 6-17: The measured rate sensitivity results from the matched in-plane modes in an 800μm diameter multi-axis disk gyroscope with V_p=25V and Q=15,000 with discrete electronics.

6.6.3 Results of Optimized Design

According to the ANSYS simulation results presented in section 6-2, a disk with uniform 6μm diameter holes should have a frequency separation less than 100Hz between its in-plane and out-of plane modes. To demonstrate this, 800μm diameter disks with uniform 6μm diameter release holes were fabricated and their frequency responses were recorded. Figure 6-18 shows a SEM view of a center-supported multi-axis disk gyroscope with

6μm diameter perforations, implemented in 40μm thick (100) SCS. The capacitive gap between the in-plane electrode and the disk was the same as the out-of plane electrode and the disk, which was ~200nm.

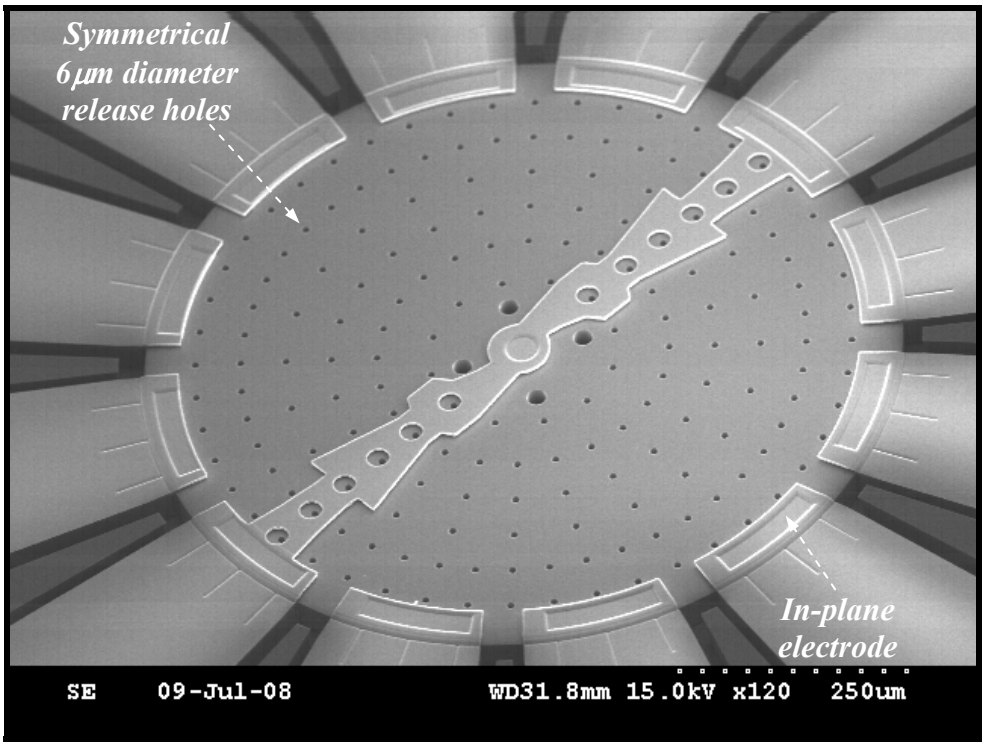

Figure 6-18: SEM view of an 800μm diameter (100) multi-axis silicon disk gyroscope with uniform 6μm diameter holes.

The frequency response of the out-of-plane modes and in-plane modes were recorded and are shown in Figure 6-19. As expected, the two modes were matched and there might be a very small frequency split of less than 60Hz (from the measured f/Q) between two out-of-plane modes and less than 104Hz (from the measured f/Q) between the in-plane modes. The measured frequency behaviors from the prototype optimized device in both in-plane and out-of-plane modes are in good agreement with ANSYS simulation results. The two modes were self-matched without the application of any tuning voltages. The

optimized multi-axis devices were further investigated for their performance parameters in their sensitive in-plane axes (*x*-axis).

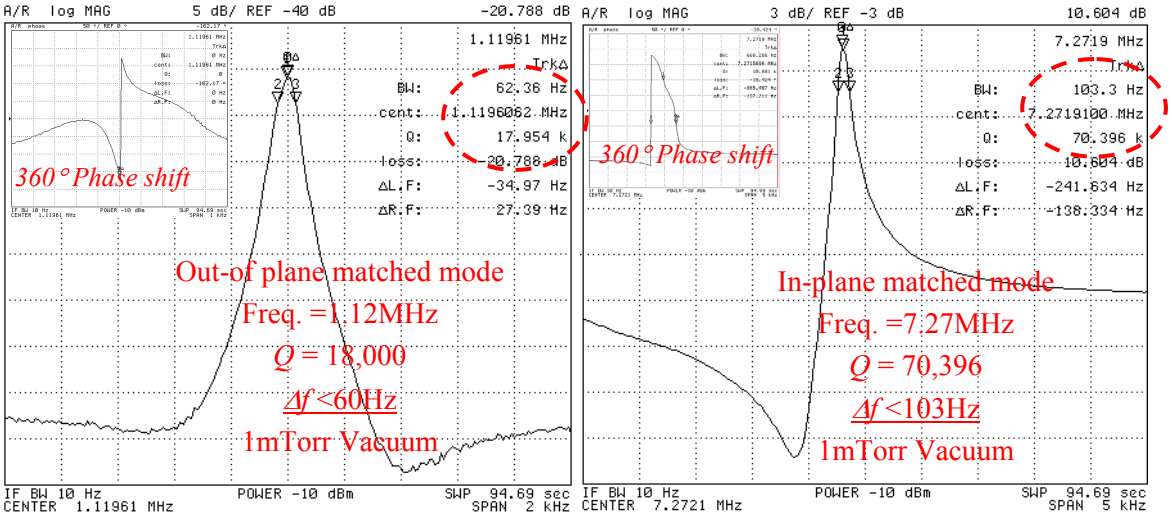

Figure 6-19: The frequency response of an 800µm diameter (100) SCS disk gyroscope with uniform 6µm diameter holes operating at: (a) out-of plane modes, (b) in-plane modes, showing the self-matched mode operation for both in-plane and out-of-plane modes.

The ZRO of the prototype gyroscope was measured and shown in Figure 6-20 (a). The bottom trace is the ZRO at the sense electrode and the top trace shows the output of the drive mode. Subsequently, the rotation rate around the *x*-axis was applied to this device and the output signal due to the application of 23°/sec around *x*-axis rotation rate was measured and shown in Figure 6-20 (b). The similar rotation response can be observed when the *y*-axis rotation rate is applied to the device.

The sensor output voltage was measured for some applied angular speeds around the *x*-axis. The scale factor was measured from only one sense electrode at matched mode operation without the application of any tuning voltages, as shown in Figure 6-21. A sensitivity of 73µV/°/sec was measured from the sense mode with V_p=4V.

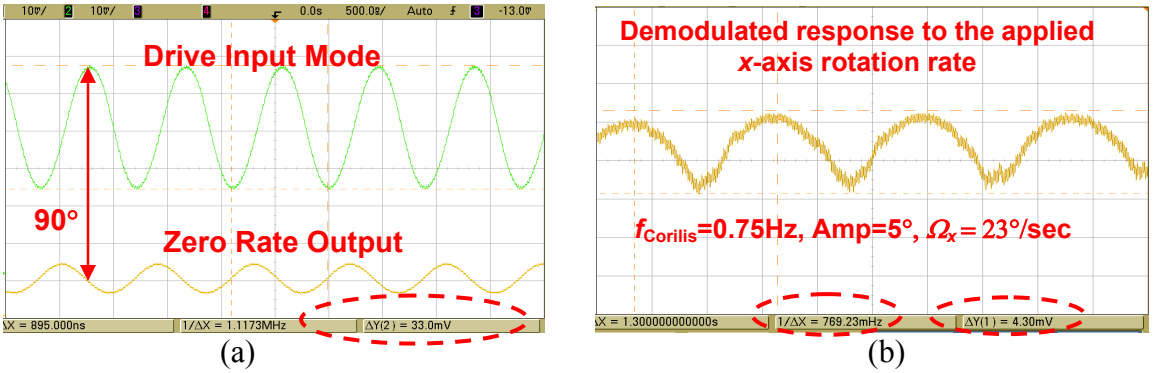

(a) (b)

Figure 6-20: (a) Zero rate output of out-of-plane modes in the multi-axis gyroscope implemented in 40µm thick (100)SCS, (b) Rotation response of an 800µm diameter, 40µm thick multi-axis disk gyroscope to the applied 23°/sec *x*-axis rotation rate.

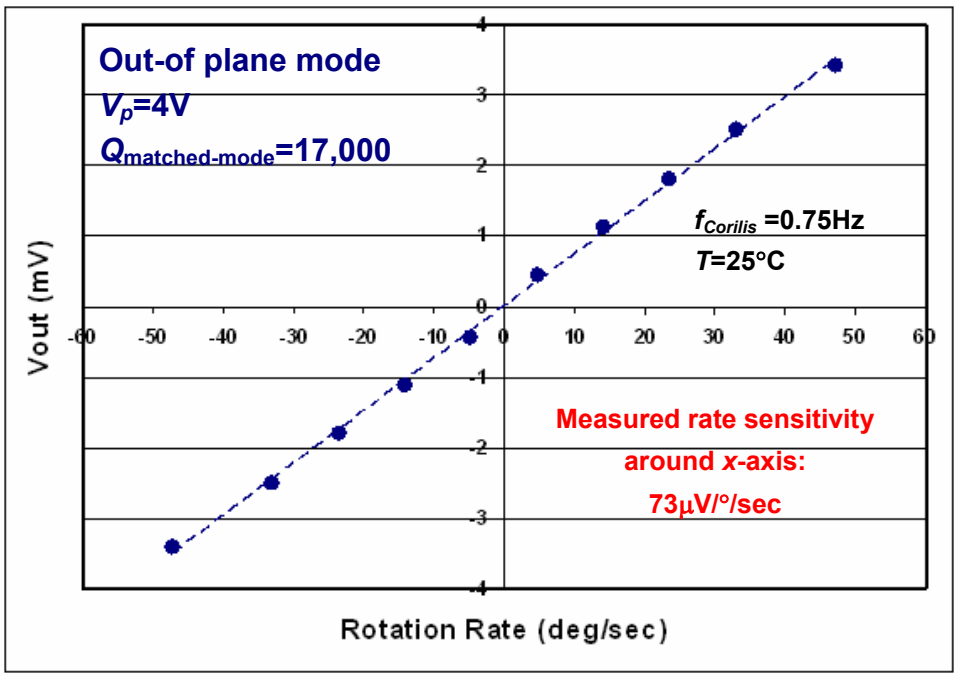

Figure 6-21: The measured rate sensitivity results from one sense electrode of an 800µm diameter disk gyroscope at matched-mode operation after quadrature cancellation with V_p=4V with discrete electronics.

Scale factor stability and bias drift are the next most critical performance parameters in a gyroscope. The scale factor stability is directly affected by the stability of $Q_{\text{matched-mode}}$ over time. It was observed that the matched out-of-plane Q remained constant over a period of 24 hours at a fixed room temperature and pressure. The zero rate output (ZRO)

of the device was sampled. Using the collected ZRO data an Allan variance analysis was performed to characterize the long-term stability of the matched-mode device interfaced with the discrete electronics. The root Allan variance plot of the prototype disk gyroscope is shown in Figure 6-22. The measured bias instability of this sensor around *x*-axis is estimated to be 0.85°/hr with $Q_{\text{matched-mode}}$ of 17,000 and V_p of 4V.

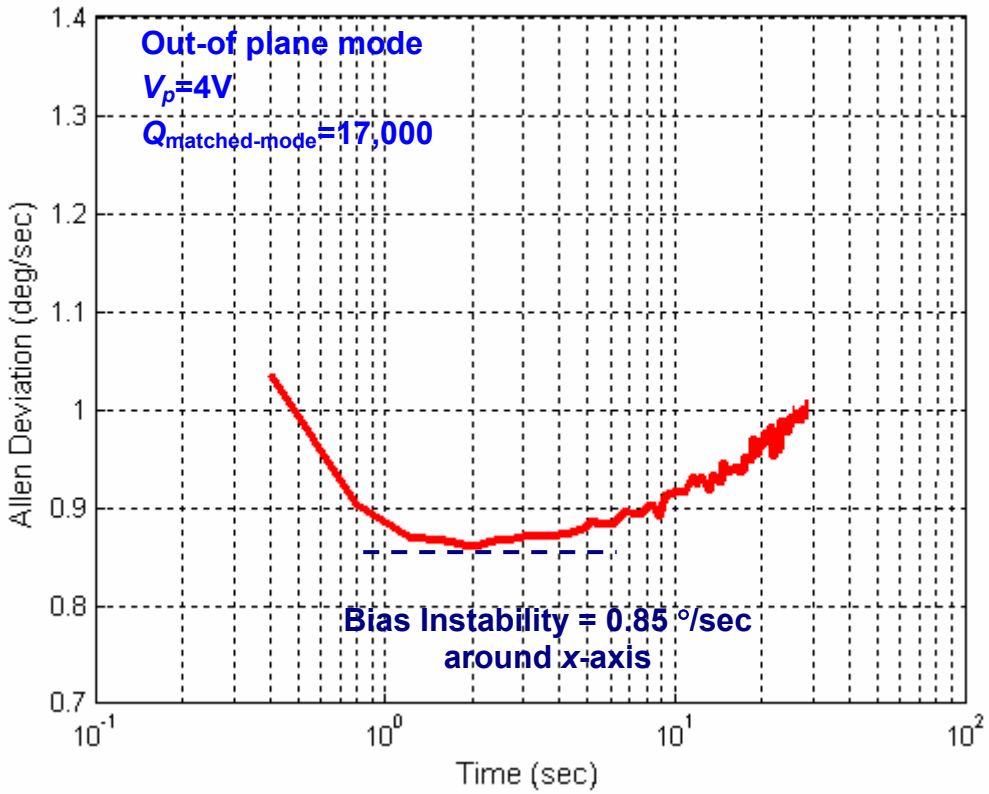

Figure 6-22 : Root Allan variance plot of an 800µm diameter disk gyroscope including uniform 6µm diameter perforations at zero rate output (ZRO) in 1mTorr vacuum.

6.7 SUMMARY

This chapter presented the design, implementation and characterization results of multi-axis disk gyroscopes. The *z*-axis silicon BAW gyroscopes have been further developed to enable sensing of rotation rates around *x*-axis or *y*-axis as well as the *z*-axis. To achieve

this, these devices were operated in their compatible out-of plane and in-plane modes. The out-of plane modes were chosen to have the same spatial symmetry as the in-plane modes have. Also, the electrodes were extended over the disk to form the in-plane electrode for detecting the out-of plane modes. These devices were fabricated in a process flow similar to that used for the *z*-axis silicon BAW gyroscopes. However, the process flow was modified to achieve the same sub-micron capacitive gaps for both in-plane and out-of plane transductions. The measured results from the 60μm thick and 40μm thick devices were presented and the rate sensitivity around *x*-axis and *z*-axis were measured in these devices. Due to the existence of the in-plane electrodes, the outermost ring of release holes had to be removed. It was found that this introduced a large frequency separation between the two in-plane modes, consequently increasing the tuning voltages required to match the two modes. To mitigate this, the effect of perforations on the frequency split of both in-plane and out-of plane modes were studied and modeled in multi-axis devices. It was found that disks with uniform small-sized perforations (<8μm diameter) have minimal frequency separation between both in-plane and out-of plane modes. These optimized designs were implemented in 40μm thick SOI substrates and the frequency responses were presented here. The very small frequency separations were observed between two in-plane and two out-of plane modes. As a result, the multi-axis disks were matched on their both in-plane and out-of plane modes without the application of any tuning voltages. The scale factor of the self-matched mode was measured around *x*-axis from only one sense electrode to be 73μV/°/sec with the application of only V_p =4V. Also, this device exhibits a bias drift of 0.85°/sec with $Q_{\text{matched-mode}}$ of 17,000 at V_p =4V.

CHAPTER 7

CONCLUSIONS AND FUTURE DIRECTIONS

7.1 CONTRIBUTIONS

In this dissertation, the design, implementation and characterization of micromachined capacitive bulk acoustic wave silicon disk gyroscopes were investigated. A list of the technical contributions made through the course of this work has been summarized as follows:

1. *Design and modeling of capacitive BAW silicon disk gyroscopes*: Capacitive disk gyroscopes were designed to operate in their primary and secondary elliptic degenerative modes in (111) and (100) single crystal silicon. Finite element analysis was employed to model the resonating disks and to study the effect of perforations on the frequency separation between their degenerative modes. A comprehensive study of degenerative elliptic modes was performed, in which the normal modal model is derived using the Lagrange method. Based on the modal analysis, angular gain was estimated for both primary and secondary elliptic modes. In addition, an electrostatic tuning method was developed to match the frequencies of the degenerative modes. Sensitivity and resolution for these gyroscopes were derived and analyzed, and the key limitations were discussed.

2. *Modeling of Thermo-Elastic Damping in BAW Disk Gyroscopes*: Finite element analysis (COMSOL Multiphysics) was uesd to model Q_{TED}, the thermo-elastic damping-limited Q, of BAW modes in silicon disk structures. Coupled

deformation and temperature partial differential equations (PDEs) were solved for eigenvalues and Q_{TED} was taken as the ratio of the imaginary part to the real part of the corresponding eigenvalue. Thermoelastic losses were modeled for a variety of disk geometries, and it was found that decreasing the disk diameter lowers Q_{TED} in elliptic modes. It was also found that the Q_{TED} in elliptic modes was not affected by disk thickness, an expected observation attributable to the in-plane motion of these modes. In addition, to understand the effect of release holes size on Q_{TED}, symmetrical uniform sized release holes were added to the COMSOL disk model. Perforations introduce localized dynamic strain concentrations, inducing additional temperature gradients and subsequently additional TED losses. In accordance, Q_{TED} was found to drop substantially for perforated disks with large release holes. It was observed that Q_{TED} of both primary and secondary elliptic modes are larger than 10^6 for a disk with perforation sizes < 8μm. This demonstrates that the total Q is not mainly limited by thermoelastic damping if the release holes are small enough.

3. *Development of a High-Aspect Ratio Fabrication Process with Self-Aligned Buried Oxide Center-Support*: A high aspect ratio process is a key determinant of a micromachined gyroscope's performance, particularly in capacitive disk BAW gyroscopes. In order to excite the disks at their MHz-frequency BAW modes, large electrostatic forces are required, which in turn necessitate large capacitive coupling. Large capacitive coupling is attained with high gap-aspect ratio and very small capacitive gap sizes. Thus, a high aspect ratio process was developed to implement these devices on thick SOI substrates (30-60μm) with sub-micron

capacitive gaps (<200nm). In addition, this process provides self-aligned perforations in the resonating disk, simultaneously eliminating asymmetry issues and reducing the frequency separation between degenerative modes. A small island of buried oxide layer (BOX) within the SOI substrate is used to support the disk at the bottom. The center post diameter is approximately one twentieth of the disk diameter, calling for careful timing of the HF release. Such small support is needed to minimize losses through it, providing high Q of the device. In addition, the symmetry of the HF etch step guarantees that the support is self-aligned to the center of the disk. The boron-doped polysilicon traces on the disk surface provide it with DC bias. Also, each poly electrode partially extends over the top of the disk to provide an out-of-plane shock stop. While the entire fabrication process was challenging, it is worth noting that trench etching and polysilicon etching inside the smaller-sized release holes (<10μm) was particularly difficult to achieve. This required numerous characterizations and recipe optimizations to achieve straight profiles and smooth sidewalls with minimum footing and scalloping.

4. *Experimental Characterizations*: Fabricated capacitive BAW disk gyroscopes, both in (100) and in (111) single crystal silicon, were experimentally characterized. The frequency response and performance parameters of these devices were measured in vacuum. The prototype devices showed ultra high quality factors (Q) in excess of 100,000 and large bandwidth, even under very high-Q matched-mode environment. The rate sensitivity was measured to be 320μV/°/sec for a 3MHz (111) SCS disk gyroscope with $Q_{\text{matched-mode}}$ of 66,000.

However, the measured rate sensitivity for a 6MHz (100) SCS disk gyroscope with $Q_{\text{matched-mode}}$ of 236,000 was 270μV/°/sec. In addition, the *Q*s of these prototype gyroscopes were characterized over a temperature range of 60°C, showing high thermal stability, even at elevated temperatures. Also, this work demonstrated that in these devices, maintaining a high *Q* does not require the high vacuum environment that is needed for low frequency, flexural-based gyroscopes. This simplifies the wafer-level encapsulation of these devices, resulting in better long-term reliability and reduced cost. Furthermore, large frequency bandwidths, in the range 10-30Hz, were achieved for these devices in high matched-mode *Q* in vacuum, making them to be suitable for the relatively fast response time requirements of consumer electronics applications.

5. *Optimized Design and Implementation of BAW Gyro*scopes: It is well-known that operating a vibratory gyroscope in matched mode, wherein the drive and sense mode frequencies overlap maximally, improves performance parameters. However, it is very challenging to electrostatically tune and match the two modes' frequencies without applying large voltages, which are difficult to generate with CMOS electronics. To eliminate this issue, a self-matched-mode BAW gyroscope was designed and implemented. The self-matched-mode operation is provided chiefly through enhanced design of the disk perforations. The release holes are designed with uniform, small size, equal spacing, and a configuration that repeats every 30° (or fraction of 30°) around the disk. This substantially reduces the frequency split by more closely approximating the behavior of the solid disk gyroscope. In addition, the operating frequency of the secondary elliptic modes

was high enough to mitigate air damping losses. This eliminates the need for vacuum packaging, resulting in substantially reduced cost. A number of these optimized disk gyroscopes were fabricated on thick (100) SOI substrates using the modified HARPSS process. The matched secondary elliptical mode of an 800μm diameter disk with 6μm diameter release holes was observed at 7.3MHz with $Q_{\text{matched-mode}}$ of 15,000 in air, providing ~400Hz device bandwidth. The measured sensitivity of this device in air to applied *z*-axis rotation was 65.4 μV/°/sec. In addition, the matched-mode *Q* and scale factor of the prototype device were characterized over a temperature range of 75°C, demonstrating the high thermal stability of these devices.

6. *Design and Implementation of Multi-Axis High-frequency Disk Gyroscopes*: Capacitive *z*-axis BAW gyroscopes are further extended to enable sensing of rotation rates around *x* and *z*-axis. This novel approach eliminates issues associated with integration of multiple proof masses, at the same time producing a very small form factor. Also, from the *z*-axis BAW gyroscope design, they inherit high shock tolerance and large frequency bandwidth. The multi-axis disk gyroscopes operate in compatible in-plane and out-of plane modes. The high aspect-ratio poly and single crystal silicon (HARPSS) fabrication process was revised and utilized to implement these devices in 40μm and 60μm thick SOI substrates. This distinctive process enables very small capacitive gap sizes of 200nm for both in-plane and out-of plane transduction. With vibration amplitudes in the tens of nanometers in each sensitive axis, high frequency disk gyroscopes are semi-stationary devices requiring small DC and AC actuation voltages. In this

research, 800μm-diameter multi-axis disk gyroscopes with both non-uniform and uniform perforations were designed and implemented in 40μm-thick (100) silicon-on-insulator (SOI) substrate. The rate sensitivity of 800μm-diameter disk with non-uniform perforations around the *x*-axis and *z*-axis were measured in (100) silicon. In addition, the multi-axis disks with uniform 6μm diameter release holes were fabricated and characterized. They exhibit self-matched mode in their both in-plane and out-of plane modes. The measured rate sensitivity around the *x*-axis of these disks was measured to be 73μV/°/sec at 1.2MHz-disk with $Q_{\text{matched-mode}}$ of 17,000 in (100) silicon. These multi-axis devices have the potential to measure the rotation rate around the all three sensitive axis using a single disk, which will be the focus of the future research.

7.2 FUTURE DIRECTIONS

Several features are still needed in both single-axis and multi-axis BAW gyroscopes before implementation into commercial products would be feasible. In this section, some of the main tasks are outlined and briefly discussed.

7.2.1 WAFER LEVEL ENCAPSULATION AND PACKAGING OF BAW DISK GYROS

To date, characterization results of BAW gyroscopes have been collected in a vacuum chamber or fully exposed to air. In order for the prototypes to be commercially viable, they need to be packaged to offer long-term reliability. As it was discussed in this research, two major classes of BAW disk gyroscopes were designed, implemented and characterized. The first class includes 6MHz disk gyroscopes with non-uniform perforations, which require low vacuum packaging in the range of 1-10Torr.

The second class, composed of 7.3MHz disk gyroscopes with uniform small perforations, do not need vacuum package. Generally speaking, these devices do not require the same high vacuum packaging as low-frequency flexural-based gyroscopes. This simplifies the requirement for packing of these devices, freeing them from long-term reliability issues such as out-gassing and manufacturing complexity. These devices can be wafer-scale packaged with low cost. However, if low vacuum packaging (1-10Torr) is provided, the performance of these devices could be improved significantly.

7.2.2 MULTI-AXIS SINGLE-DISK GYROSCOPES

In this research, multi-axis devices were designed and modeled to enable measuring the rotation rate around the *x*-axis as well as the *z*-axis. The perforations in these devices were optimized to provide small frequency separation between both in-plane degenerative modes and out-of-plane degenerative modes. The sensitivity results of a multi-axis disk gyroscope to the input rotation rate around *x*-axis and *z*-axis was measured from one device at separate times. However, these devices can be further investigated to measure all three axes using a single disk. In order to fully investigate these devices, the normal modal equations need to be solved for out-of-plane modes to estimate the angular gain. Also, the exact form of sensitivity equation should be derived for *x*/*y*-axis. It is also desired to measure the sensitivity around the *y*-axis from these devices and compare to the *x*-axis measurement results and the cross-sensitivity should be further investigated. Subsequently, an appropriate interface circuit must be developed to separately detect and demodulate the three axis rotation rates.

7.2.3 CLOSED-LOOP OPERATION

In order to improve the dynamic range and to maintain constant oscillation amplitude, these gyroscopes need closed-loop control of both drive and sense modes. Closed-loop operation entails force-balancing the resonating disk along the sense-axis, probably achieved with a negative feedback control loop. The feedback loop would measure the Coriolis-induced sense-mode deflections, and apply the necessary opposing forces to keep the resonating disk stationary (along the sense-axis). Preventing very large deflections should increase the sensor's dynamic range, as it would limit the non-linearity of the capacitive transduction as well as of the mechanical springs.

Also, BAW gyroscopes are driven without drive close loop control, which introduces drive amplitude instability if environmental condition changes. As reported in Chapter 5, the drive amplitude of the 7MHz disk gyroscopes with uniform small perforations was not constant over the temperature range. This contributed to the performance instability of these devices. Utilizing a close loop configuration for the drive mode offers the constant and controllable drive amplitude, improving the performance parameters.

7.2.4 FULLY-DIFFERENTIAL INTERFACE ARCHITECTURE

As mentioned earlier in this dissertation, all the measurement results were taken from a single sense electrode. The scale factor in BAW gyroscopes has the potential to be improved by a factor of ~6 in (100) SCS without changing the deivce design. To accomplish this, six electrodes need to be used for sense mode measurement. From the single electrode presently used, the output signals from two electrodes located at 120° and 240° offset from the sense electrode need to be coupled (signal 1); simultaneously, the three output signals at the three electrodes located 60°, 180° and 300° away should be

coupled together (signal 2). Afterwards signal 1 should be subtracted from signal 2, enlarging the output signal ~6 times, due to the tapping of ~6 times larger capacitive coupling area. This results in much higher sensitivity and lower electronic noise. On the other hand, the same method can be applied for the drive mode as well, which could be used to increase the drive amplitude, and thus lower the Brownian noise floor and improve the sensitivity. The similar method can be employed for the devices operated in their primary elliptic modes in (111) SCS. The performance parameters can be improved by a factor of ~4 in (111) SCS in these devices due to the mode shapes' configuration.

APPENDIX A

THERMOELASTIC COEFFICIENTS

To determine the eignvalues and consequently Q_{TED} of BAW disk structure, the multiphysics model in COMSOL3.4 is utilized. The available general format of thermoelastic equations in this model was expressed in (3-78). Before starting to determine each coefficient in this equation, the displacement matrix should be established with the displacement, velocity and temperature of each node. It is worth noting that the arrangement of each component in the displacement matrix is a determinant key in defining the location of non-zero components in the coefficient matrices. Accordingly, the displacement matrix in our model is defined as below:

$$\begin{bmatrix} u_\phi & \dot{u}_\phi & u_\varphi & \dot{u}_\varphi & u_\psi & \dot{u}_\psi & T \end{bmatrix} \tag{A-1}$$

where u_ϕ, $\dot{u}_\phi$, u_φ, $\dot{u}_\varphi$ and u_ψ, $\dot{u}_\psi$ are respectively the displacement and velocity components in the normalized ϕ, φ and ψ directions and T is the temperature for each node in our geometry model.

Employing the above displacement matrix, all the coefficient matrices are determined as following. The c_1 is a 7×7 matrix in which each component is composed of 3×3 matrices. The elements in c_1 introduce the elasticity factors into the thermoelastic modeling. The non-zero matrices are defined as following:

$$c_{11}=\begin{bmatrix}2+\lambda/\mu & 0 & 0\\ 0 & 1 & 0\\ 0 & 0 & 1\end{bmatrix}\ c_{12}=\begin{bmatrix}0 & \lambda/\mu & 0\\ 1 & 0 & 0\\ 0 & 0 & 0\end{bmatrix}\ c_{13}=\begin{bmatrix}0 & 0 & \lambda/\mu\\ 0 & 0 & 0\\ 1 & 0 & 0\end{bmatrix}$$

$$c_{21}=\begin{bmatrix}0 & 1 & 0\\ \lambda/\mu & 0 & 0\\ 0 & 0 & 0\end{bmatrix}\ c_{22}=\begin{bmatrix}1 & 0 & 0\\ 0 & 2+\lambda/\mu & 0\\ 0 & 0 & 1\end{bmatrix}\ c_{23}=\begin{bmatrix}0 & 0 & 0\\ 0 & 0 & \lambda/\mu\\ 0 & 1 & 0\end{bmatrix} \tag{A-2}$$

$$c_{21}=\begin{bmatrix}0 & 0 & 1\\ 0 & 0 & 0\\ \lambda/\mu & 0 & 0\end{bmatrix}\ c_{22}=\begin{bmatrix}0 & 0 & 0\\ 0 & 0 & 1\\ 0 & \lambda/\mu & 0\end{bmatrix}\ c_{23}=\begin{bmatrix}1 & 0 & 0\\ 0 & 1 & 0\\ 0 & 0 & 2+\lambda/\mu\end{bmatrix}$$

where λ and μ are the lame coefficients and can be expressed as below:

$$\lambda=\frac{E}{1+\upsilon}\left(\frac{\upsilon}{1-2\upsilon}\right) \tag{A-3}$$

$$\mu=\frac{E}{2(1+\upsilon)} \tag{A-4}$$

Where E and υ are respectively the Young's modulus and the Poisson ratio. The α and β are both 7×7 matrices, in which each component is composed of 3×1 matrices. These matrices establish the thermoelastic coefficients into our model. The non-zero matrices are:

$$\alpha_{17}=\begin{bmatrix}-\eta & 0 & 0\end{bmatrix}\ \alpha_{27}=\begin{bmatrix}0 & -\eta & 0\end{bmatrix}\ \alpha_{37}=\begin{bmatrix}0 & 0 & -\eta\end{bmatrix} \tag{A-5}$$

$$\beta_{74}=\begin{bmatrix}\eta & 0 & 0\end{bmatrix}\ \beta_{75}=\begin{bmatrix}0 & \eta & 0\end{bmatrix}\ \beta_{76}=\begin{bmatrix}0 & 0 & \eta\end{bmatrix} \tag{A-6}$$

where η is defined in Chapter 3, (3-75).

The γ_1 matrix is a 7×1 matrix and all the elements should be considered as zero in this model. The a and d_a are both 7×7 matrices of scalars as stated in the followings:

$$a = \begin{bmatrix} 0 & 0 & 0 & 0 & 0 & 0 & 0 \\ 0 & 0 & 0 & 0 & 0 & 0 & 0 \\ 0 & 0 & 0 & 0 & 0 & 0 & 0 \\ 0 & 0 & 0 & 1 & 0 & 0 & 0 \\ 0 & 0 & 0 & 0 & 1 & 0 & 0 \\ 0 & 0 & 0 & 0 & 0 & 1 & 0 \\ 0 & 0 & 0 & 0 & 0 & 0 & 0 \end{bmatrix} \tag{A-7}$$

$$d_a = \begin{bmatrix} 0 & 0 & 0 & i & 0 & 0 & 0 \\ 0 & 0 & 0 & 0 & i & 0 & 0 \\ 0 & 0 & 0 & 0 & 0 & i & 0 \\ -i & 0 & 0 & 0 & 0 & 0 & 0 \\ 0 & -i & 0 & 0 & 0 & 0 & 0 \\ 0 & 0 & -i & 0 & 0 & 0 & 0 \\ 0 & 0 & 0 & 0 & 0 & 0 & -i \end{bmatrix} \tag{A-8}$$

The imaginary numbers appear in (A-8) are placed in an arrangement to ensure that the imaginary and real parts of the eignvalues are swapped. This is needed so that the COMSOL3.4 can find the eignvalues easier.

The next main term is to determine the boundary condition in our model. Three types of boundary conditions are available in the multiphysics model in COMSOL which they can be applied at the surface of the geometry under study.

1- Anchored surface: This implies that displacements for a particular surface are zero.

2- Free surface: This indicates that no normal force is applied to the surface.

3- Mirror symmetric surface: This can be accomplished by choosing a plane where no displacement is allowed perpendicular to this plane while the motion is unconstraint in the plane itself. It is worth noting that all of these boundary conditions include a zero heat flow condition. For our model, it was assumed that the center of the disk is an anchored surface. The general format of boundary condition in COMSOL3.4 is expressed in (A-9).

$$n.(c_1\nabla u + \alpha u - \gamma_1) + q_1 u = g - h^T.u \text{ where } h.u = r \qquad \text{(A-9)}$$

where c_1,α and u are the same matrices as in (A-2) and (A-5) and (A-1). And n is the normal vector to the surface of the geometry. For all boundary conditions, γ_1, q, r, g matrices are set to zero, however h is a 7×7 matrix of scalars to determine the type of applied boundaries in the structure. In our model, a circular area with 40μm diameter is utilized as a center support. Accordingly, h is defined as in (A-10) for the center support area in BAW disk.

$$h = \begin{bmatrix} 1 & 0 & 0 & 0 & 0 & 0 & 0 \\ 0 & 1 & 0 & 0 & 0 & 0 & 0 \\ 0 & 0 & 1 & 0 & 0 & 0 & 0 \\ 0 & 0 & 0 & 1 & 0 & 0 & 0 \\ 0 & 0 & 0 & 0 & 1 & 0 & 0 \\ 0 & 0 & 0 & 0 & 0 & 1 & 0 \\ 0 & 0 & 0 & 0 & 0 & 0 & 0 \end{bmatrix} \qquad \text{(A-10)}$$

Given the material property of the disk, all the elements in the above matrices were evaluated and entered into our multiphysics model in COMSOL3.4. The model is solved for the eignvalues of each selected resonant mode, as presented in Chapter 3.

APPENDIX B

MTALAB CODES TO ESTIMATE DESIGN PARAMETERS

```
% Estimating k_m and h_m
function f=findk(k)
m=3;
v=0.17686;
h=k.*(2./(1-v))^0.5;
f= ((k.*besselj(m-1,k)./besselj(m,k))-m-h.^2/(2*(m^2-1)))...
 .*((h.*besselj(m-1,h)./besselj(m,h))-m-h.^2/(2*(m^2-1)))...
 -(m^2)*((h.^2)./(2*(m^2-1))-1).^2;
figure (1)
x=0.5:.0001:3;
semilogy(x,findk(x));
figure (2)
plot(x,findk(x));
k1= fzero(@(k) findk(k),2)

% Estimating U_r and U_θ at r=R
clear all;
m=3;
k=2.2990;
v=0.177;
R=400.*10^(-6);
ro=2330;
h=k.*sqrt(2./(1-v))
sie=(besselj(m,k)./besselj(m,h)).*(((2.*k.*besselj(m-1,k)./besselj(m,k))+h^2-
2.*m.*(m+1))./((((h.*besselj(m-1,h))./besselj(m,h))-(m+1)).*2.*m));
z=k;
y=h;
DIFFZ=(0.5).*(k./R).*(besselj(m-1,z)-besselj(m+1,z));
DIFFY=(0.5).*(h./R).*(besselj(m-1,y)-besselj(m+1,y));
```

```
UR_R=(R.*DIFFZ+m.*sie.*besselj(m,y))
Utheta_R=(-m*besselj(m,z)-R*sie*DIFFY)

% Estimating the effective mass function
function f=difM(r,theta)
m=3;
k=2.299;
v=0.17686;
R=400.*10^(-6);
ro=2330;
h=k.*sqrt(2./(1-v))
i=1;
sie=(besselj(m,k)./besselj(m,h)).*(((2.*k.*besselj(m-1,k)./besselj(m,k))+h^2-
2.*m.*(m+1))./((((h.*besselj(m-1,h))./besselj(m,h))-(m+1)).*2.*m))
%r=r/R (non-dimensionalized)
z=k.*r./R;
y=h.*r./R;
DIFFZ=0.5.*(k./R).*(besselj(m-1,z)-besselj(m+1,z));
DIFFY=0.5.*(h./R).*(besselj(m-1,y)-besselj(m+1,y));
phi_r1=(R.*DIFFZ+(m.*R./r).*sie.*besselj(m,y)).*cos(m.*theta);
phi_r2=-(R.*DIFFZ+(m.*R./r).*sie.*besselj(m,y)).*sin(m.*theta);
phi_theta1=+(-(m.*R./r).*besselj(m,z)-R.*sie.*DIFFY).*sin(m.*theta);
phi_theta2=+(-(m.*R./r).*besselj(m,z)-R.*sie.*DIFFY).*cos(m.*theta);
f=((phi_r1).^2+(phi_theta1).^2).*r;

% Estimating the coriolis coupling function
function f=difBessel(r,theta)
m=3;
k=2.2990;
v=0.17686;
R=400.*10^(-6);
ro=2330;
h=k.*sqrt(2./(1-v));
```

```
i=1;
sie=(besselj(m,k)./besselj(m,h)).*(((2.*k.*besselj(m-1,k)./besselj(m,k))+h^2-
2.*m.*(m+1))./((((h.*besselj(m-1,h))./besselj(m,h))-(m+1)).*2.*m));
z=k.*r./R;
y=h.*r./R;
DIFFZ=0.5.*(k./R).*(besselj(m-1,z)-besselj(m+1,z));
DIFFY=0.5.*(h./R).*(besselj(m-1,y)-besselj(m+1,y));
phi_r1=(R.*DIFFZ+(m.*R./r).*sie.*besselj(m,y)).*cos(m.*theta);
phi_r2=-(R.*DIFFZ+(m.*R./r).*sie.*besselj(m,y)).*sin(m.*theta);
phi_theta1=(-(m.*R./r).*besselj(m,z)-R.*sie.*DIFFY).*sin(m.*theta);
phi_theta2=(-(m.*R./r).*besselj(m,z)-R.*sie.*DIFFY).*cos(m.*theta);
f=(((phi_r1.*phi_theta2)-(phi_r2.*phi_theta1)).*r);

% Estimating the angular gain and effective mass
clear all;
close all;
G1=dblquad(@(r,theta) (difBessel(r,theta)), 0.1*10^(-9), 400*10^(-6), 0, 2*pi);
M1=dblquad(@(r,theta) (difM(r,theta)), 0.1*10^(-9), 400*10^(-6), 0, 2*pi);
Ag=G1./(3.*M1);
Ur=0.9430;
Ut=0.0705;
ro=2330;
R=400e-6;
h=40*10^(-6);
M2=(M1*h*ro)
G2=G1*h*ro
U=sqrt(Ur^2+Ut^2)
M3=(M2)*(1/U^2)
G3=G2*(1/U^2)
Ag2=G3/(3*M3)
M4=ro*h*pi*(R^2)
mcoef=M3/M4;
```

REFERENCES

[1] J. Marek, "MEMS technology- from automotive to consumer," in *proceedings of IEEE/ASME Conference on Microelectromechanicalsystems (MEMS '07)*, Kobe, Japan, Jan. 2007, pp. 59-60.

[2] R. Neul, et al., "Micromachined angular rate sensors for automotive applications," *IEEE Sensors Journal*, vol. 7, no. 2, pp. 302-309, Feb. 2007.

[3] R. H. Dixon and J. Bouchaud, "Markets and applications for MEMS inertial sensors," in *Proceedings of the SPIE - The International Society for Optical Engineering*, vol. 6113, no. 21, Jan. 2006, pp. 611306-1-10.

[4] E. Mounier and J. C. Eloy, "New emerging MEMS applications," in *Proceedings of the SPIE, The International Society for Optical Engineering*, vol. 6462, no. 8, Feb. 2007, pp. 64620C-1-7.

[5] W. A. Clark, R. T. Howe, and R. Horowitz, "Surface micromachined Z-axis vibratory rate gyroscope," in *Proceedings of the Solid-State Sensors and Actuatos workshop*, Hilton Head, SC, June 1996, pp. 283-287.

[6] H. Xie, and G. Fedder, "A DRIE CMOS-MEMS gyroscope," in *proceedings of the IEEE Sensors'04*, Vienna, Austria, Oct. 2004, pp. 1413-1416.

[7] M. F. Zaman, A. Sharma, B. V. Amini and F. Ayazi, "The Resonating Star Gyroscope," *in Proceedings of IEEE/ASME Conference on Microelectromechanicalsystem (MEMS'05)*, Miami, FL, Jan. 2005, pp. 355-358.

[8] M. F. Zaman, A. Sharma and F. Ayazi, "High Performance Matched-Mode Tuning Fork Gyroscope," in *Proceedings of IEEE/ASME Conference on Microelectromechanicalsystem (MEMS'06)*, Istanbul, Turkey, Jan. 2006, pp. 66-69.

[9] F. Ayazi and K. Najafi, "A HARPSS Polysilicon Vibrating Ring Gyroscope," *in IEEE Journal of Microelectromechanical Systems*, vol. 10, no. 2,pp. 161-179, June 2001.

[10] A. Sharma, M. F. Zaman, M. Zurcher and F. Ayazi, "A 0.1°/hr bias drift electrically-matched tuning fork microgyroscopes," *IEEE/ASME Conference on Microelectromechanicalsystem (MEMS'08)*,Tucson, AR, Jan. 2008, pp. 6-9.

[11] M. F. Zaman, Ajit Sharma, Zhili Hao and Farrokh Ayazi, "A Mode-Matched Silicon Yaw Tuning Fork Gyroscope with Sub-Deg/Hr Allan Deviation Bias Instability," *it is accepted to be published in JMEMS*, 2008.

[12] M. F. Zaman, “Degree-Per-Hour Mode-Matched Micromachined Silicon Vibratory Gyroscopes,” PhD Thesis, in Electrical and Computer Engineering, Georgia Institute of Technology, April, 2008.

[13] “MEMS on the move: motion sensors for the masses,” in *Electronic Design*, vol. 55, no. 14, 43-4, 46-7, 50, July 2007

[14] S. S. Nasiri, “Method of making an X-Y dual mass tuning fork gyroscope with vertically integrated electronics and wafer-scale hermetic packaging,” Patent No., US6939473 B2, Sep. 6, 2005.

[15] “ADIS16365: High-Precision Tri-Axis Inertial Sensor", in *Analog Devices Data Sheet*, 2008.

[16] “ADXRS150 Yaw rate gyroscope,” in *Analog Devices Data Sheet*, 2008.

[17] “IDG-1004 Integrated dual-axis gyroscope,” in *Invensense Data Sheet*, 2008.

[18] C. Machover, *Basics of Gyroscopes,* vol. 1, New York, NY: John F. Rider Publishing, 1963.

[19] H. A. Rosen, “High torque double gimbal control moment gyro,” Patent No., US5437420, July 16, 1993.

[20] F. Klein and A. Sommerfeld, "Über die Theorie des Kreisels (Tr., About the theory of the gyroscope),” *B.G. Teubner*, vol. 4, Leipzig, Berlin,pp. 1898-1914.

[21] D. MacKenzie, *Inventing Accuracy: A Historical Sociology of Nuclear Missile Guidance*, Cambridge: MIT Press, 1990.

[22] A. Michelson and H. G. Gale, F. Pearson, “The Effect of the Earth's Rotation on the Velocity of Light,” in *Astrophysical Journal*, vol. 61, pp. 140-145, April 1925.

[23] H. C. LeFèvre, *The Fiber-Optic Gyroscope*, Norwood, MA: Artech House., 1993.

[24] “GG1320AN ring laser gyroscope,” in *Honeywell Data Sheet*, 2007.

[25] A. Lawrence, *Modern inertial technology*, Springer-Verlag, 1993.

[26] J. S. Yang, H. Y. Fang and Q. Jiang, *“Analysis of a few piezoelectric gyroscopes,”* in *Proceedings of the IEEE/EIA International Frequency Control Symposium and Exhibition,* Kansas City, MO, June 2000, pp. 79-86.

[27] J. Dickinson and C. R. Strandt, “HRG strapdown navigator,” *IEEE PLANS '90: Position Location and Navigation Symposium Record. `The 1990's - A Decade of Excellence in the Navigation Sciences',* Las Vegas, NV, March 1999, pp. 20-23.

[28] J. Soderkvist, "Electrostatic excitation of tuning fork shaped angular rate sensors," in *Journal of Micromechanics and Microengineering*, vol. 7, no. 3, pp. 200-3, Sept. 1997.

[29] Y. Dong, Z. Gao, R. Zhang and Z. Chen, "A vibrating wheel micromachined gyroscope for commercial and automotive applications," in *Proceedings of the IEEE Instrumentation and Measurement Technology Conference,* vol. 3, May 1999, pp. 1750-4.

[30] M. Jammer, *Concepts of Force,* Mineola: Dover Publications, 1962.

[31] L. Meirovitch, *Analytical methods in vibrations*, McMillan Publishing, 1967.

[32] T. B. Gabrielson, "Mechanical-thermal noise in micromachined acoustic and vibration sensors," in *IEEE Transaction Electron Devices*, vol. ED-40, no. 5, pp. 903-909, May 1993.

[33] A. Sharma, "CMOS circuits and systems for sub-degree/hour MEMS gyroscopes," Ph.D. dissertation, in Electrical Engineering, Georgia Institute of Technology, December 2007.

[34] Gyroscope and Accelerometer Panel, IEEE Aerospace and Electronics Systems Technology, "IEEE standard for inertial sensor terminology," *IEEE* 2001.

[35] W. Geiger, B. Folkmer, J. Merz, H. Sandmaier, and W. Lang, "A new silicon rate gyroscope," in *Proceedings of the IEEE Microelectromechanicalsystems Workshop (MEMS'98)*, Heidelberg, Germany, Jan. 1998, pp. 615-620.

[36] A. Sharma, M. F. Zaman and F. Ayazi, "A 0.2°/hr micro-gyroscope with automatic CMOS mode matching," in *IEEE International Solid-State Circuits Conference (ISSCC'07)*, San Francisco, CA, Feb. 2007, pp. 386-610

[37] Lawrence, *Modern Inertial Technology: Navigation, Guidance, and Control*, *New York: Springer-Verlag*, 1993.

[38] J. Bernstein, et. al., "A micromachined comb-drive tuning fork rate gyroscope," *in Proceedings of IEEE/ASME Conference on Microelectromechanicalsystem (MEMS'93)*, Fort Lauderdale, FL, Feb. 1993, pp. 143-148.

[39] S. Bhave, et al., "An integrated, vertical-drive, in-plane-sense microgyroscope," *in Tech. Digest of the International Conference on Solid-State Sensors and Actuators (Transducers '*03), Boston, MA, June 2003, pp. 171-174.

[40] O. Schwarzelbach, G. Fakas and W. Nienkirchen, "New approach for resonant frequency matching of tuning fork gyroscopes by using a non-linear drive concept," *in Tech. Digest of the International Conference on Solid-State Sensors and Actuators (Transducers '*01), Munich, Germany, June 2001, pp.464-467.

[41] Y. Mochida, M. Tamura, and K. Ohwada, "A micromachined vibrating rate gyroscope with independent beams for the drive and detection modes," in *proceedings of IEEE/ASME Conference on Microelectromechanicalsystems (MEMS '99)*, Orlando, FL, Jan. 1999, pp. 618-623.

[42] M.W. Putty and K. Najafi, "A micromachined vibrating ring gyroscope," *in Technical Digest Solid-State Sensor and Actuator Workshop*, Hilton Head Island, SC, 1994, pp. 213-20.

[43] P. Greiff, B. Boxenhorn, T. King and L. Niles, "Silicon monolithic micromechanical gyroscope," *in Tech. Digest of the International Conference on Solid-State Sensors and Actuators (Transducers '91)*, San Francisco, CA, June 1991, pp. 966-968.

[44] J. Bernstein, et al., "A micromachined comb-drive tuning fork rate gyroscope," in *proceedings of IEEE/ASME Conference on Microelectromechanicalsystems (MEMS'93)*, Fort Lauderdale, FL, Feb. 1993, pp. 143-148.

[45] Y. Gianchandani, and K. Najafi, "A bulk silicon dissolved wafer process for microelectromechanical systems" in *proceedings of IEEE/ASME Conference on Microelectromechanicalsystems (MEMS'92)*, Travemunde, Germany, Feb. 1992, pp. 77-85.

[46] H. Xie, and G. Fedder, "A CMOS-MEMS lateral-axis gyroscope," in *proceedings of IEEE/ASME Conference on Microelectromechanicalsystems (MEMS'02)*, Las Vegas, NV, Jan. 2002, pp. 162-165.

[47] W. A. Clark, R. T. Howe and R. Horowitz, "Surface micromachined Z-axis vibratory rate gyroscope," in *Tech. Digest Solid-State Sensor and Actuator Workshop*, Hilton Head Island, SC, USA, June 1996, pp. 283-7.

[48] A. E. Frank, Tsu-Jae King and R. T. Howe, "Integrated MEMS technologies," *in Proceedings MRS Bulletin*, vol. 26, no. 4, pp. 291-295, April 2001.

[49] Y. Mochida, M. Tamura, and K. Ohwada, "A micromachined vibrating rate gyroscope with independent beams for the drive and detection modes," in *Sensors and Actuators A (Physical)*, vol. A80, no. 2, pp. 170-8, March 2000.

[50] H. Song, et al., "Wafer level vacuum packaged de-coupled vertical gyroscope by a new fabrication process," in *proceedings of IEEE/ASME Conference on Microelectromechanicalsystems (MEMS'00)*, Miyazaki, Japan, Jan. 2000, pp. 520-524.

[51] W. Geiger, et al., "Decoupled microgyroscopes and the design principle DAVED," in *Sensors and Actuators A (Physical)*, vol. A95, no. 2-3, pp. 239-49, Jan. 2002.

[52] M. Lutz, W. Golderer, J. Gerstenmeier, J. Marek, B. Maihofer, S. Mahler, H. Munzel and U. Bischof, "A precision yaw rate sensor in silicon micromachining," in *Tech. Digest of the International Conference on Solid-State Sensors and Actuators (Transducers '97)*, Chicago, IL, June 1997, pp. 847-850.

[53] M. S. Weinberg and A. Kourepenis, "Error sources in in-plane silicon tuning-fork MEMS gyroscopes," in *Journal of Microelectromechanical Systems*, vol. 15, no. 3, 479-91, June 2006.

[54] S. Bae, K. Hayworth, K. Shcheglov, K. Yee, and D. Wiberg, "JPL's MEMS gyroscope fabrication, 8-electrode tuning and performance results," in *Proceedings of the Solid-State Sensors and Actuators*, Hilton Head, SC, June 2002.

[55] C. Acar and A. M. Shkel, "An approach for increasing drive-mode bandwidth of MEMS vibratory gyroscopes," in *Journal of Microelectromechanical Systems,* vol. 14, no. 3, pp. 520-528, June 2005.

[56] R. Neul, et al., "Micromachined gyros for automotive applications," in *proceedings of the IEEE Sensors*, Irvine, CA, Oct. 2005, pp. 527-530.

[57] B. Kanani, J. S. Burdess, "The piezoelectric cylinder gyroscope," in *Proceedings of the Institution of Mechanical Engineers, International Conference. Mechatronics: Designing Intelligent Machines (IMechE 1990-8)*, Cambridge, UK, Sept. 1990, pp. 61-6.

[58] D. Hopkin, C. P. Fell, K. Townsend and T. R. Mason, "Vibrating Structure Gyroscope", United States Patent Number 5932804, August 1999.

[59] J. Harris, J. S. Burdess, D. Wood, R. Langford, G. Williams and M. E. McNie "Issues associated with the design, fabrication and testing of a crystalline silicon ring gyroscope with electromagnetic actuation and sensing," in *Journal of Micromechanics and Microengineering*, vol. 8, no. 4, pp. 284-92, Dec. 1998.

[60] M. E. McNie, M. C. L. Ward, J. S. Burdess, A. J. Harris, R. Langford, G. Williams and D. Wood, "Design and fabrication of a micromachined silicon ring gyroscope," in *Proceedings of the European Conference on Solid-State Tranducers and the UK Conference on Sensors and their Applications*, vol. 1, Sept. 1998, pp. 369-72.

[61] S. Chang, M. Chia, P. Castillo-Borelley, W. Higdon, Q. Jiang, J. Johnson, L. Obedier, M. Putty, Q. Shi, D. sparks and S. Zarabadi, "An electroformed CMOS integrated angular rate sensor," in *Sensors and Actuators A (Physical)*, vol. A66, no. 1-3, pp.138-43, April 1998.

[62] F. Ayazi, "The HARPSS Process for Fabrication of Precision MEMS Inertial Sensors," *Mechatronics 12 (2002)*, Nov. 2002, pp. 1185-1199.

[63] T. Juneau, A. P. Pisano and J. H. Smith, "Dual axis operation of a micromachined rate gyroscope," *in Tech. Digest of the International Conference on Solid-State Sensors and Actuators (Transducers '97)*, vol. 2, Chicago, IL, June 1997, pp. 883-6.

[64] S. An, K. Y. Park, Y. Oh and C. Song, "Two-input axis angular rate sensor," in *Proceedings of the SPIE - The International Society for Optical Engineering*, vol. 3673, Newport Beach, CA, March 1999, pp. 219-29.

[65] L. Hao, G. Fedder and L.R. Carley, "Integrated multiple-device IMU system with continuous-time sensing circuitry," *in Tech. Digest of the IEEE Solid-State Circuits Conference (ISSCC'03)*, vol. 1H, San Francisco, CA, Feb. 2003, pp. 204-5.

[66] B. J. Gallacher, J. S. Burdess, and A. J. Harris, "Principles of a three-axis vibrating gyroscope," in *IEEE Transactions on Aerospace and Electronic Systems*, vol. 37, no. 4, 1333-43, Oct. 2001.

[67] B. J. Gallacher, J. A. Neasham, J. S. Burdess and A. J. Harris, "Initial test results from a 3-axis vibrating ring gyroscope," in *Journal of Physics: Conference Series*, vol. 34, no. 1, pp. 662-7, May 2006.

[68] "SMG061 Angular rate sensor," in *Bosch Data Sheet*, 2008.

[69] "SiRRS01 Angular Rate Sensor," in *Silicon Sensing Systems Data Sheet*, 2008.

[70] "MAG-16 MEMS single axis gyroscope," in *Northrop-Grumman Data Sheet*, 2008.

[71] "IDG-300 Integrated dual-axis gyroscope," in *Invensense Data Sheet*, 2008.

[72] H. Johari and F. Ayazi, "Capacitive Bulk Acoustic Wave Silicon Disk Gyroscopes," in T*ech. Digest of International Electron Device Meeting (IEDM'06)*, San Francisco, CA, Dec. 2006, pp. 513-516.

[73] J. Shah, H. Johari, A. Sharma and F. Ayazi, "CMOS ASIC for MHz Silicon BAW Gyroscope," in *IEEE International Symposium on Circuits and Systems (ISCAS'08)*, Seattle, Washington, May 2008, pp. 2458-2461.

[74] Z. Hao and F. Ayazi, "Support Loss in Micromechanical Disk Resonators," in in *proceedings of IEEE/ASME Conference on Microelectromechanicalsystems (MEMS '05)*, Miami, FL, Jan. 2005, pp. 137-141.

[75] Z. Hao and F. Ayazi, "Support loss in the radial bulk-mode vibrations of center-supported micromechanical disk resonators," in *Sensors and Actuators A (Physical)*, vol. 134, no. 2, March 2007, pp. 582-93.

[76] J. Kim, et al, “Why is (111) Silicon a Better Mechanical Material for MEMS?” in *Tech. Digest of the International Conference on Solid-State Sensors and Actuators (Transducers* '01), Munich, Germany, June 2001, pp. 662-5.

[77] H. Guohong and K. Najafi, “A single-crystal silicon vibrating ring gyroscope,” in *proceedings of IEEE/ASME Conference on Microelectromechanicalsystems (MEMS '02)*, Los Vagas, NV, Jan. 2002, pp.718-721.

[78] H. Johari and F. Ayazi, "High frequency capacitive disk gyroscopes in (100) and (111) silicon,” in *proceedings of IEEE/ASME Conference on Microelectromechanicalsystems (MEMS '07)*, Kobe, Japan, Jan. 2007, pp. 47-50.

[79] Z. Hao, S. Pourkamali, and F. Ayazi, "VHF Single Crystal Silicon Elliptic Bulk-Mode Capacitive Disk Resonators; Part I: Design and Modeling," in *IEEE Journal of Microelectromechanical Systems*, vol. 13, no. 6, pp. 1043-1053, Dec. 2004.

[80] M. W. Putty, “A micromachined vibrating ring gyroscope,” Ph.D. dissertation, in Electrical Engineering Department, University of Michigan, Dec. 2000.

[81] M. Onoe, “Contour vibrations of isotropic circular plates,” in *Journal of Acoustic Society American*, vol. 28, no. 6, pp. 1158–1162, Nov. 1956.

[82] W. T. Thompson, *Theory of Vibration with Applications*, Prentice-Hall. Englewood Cliff, New Jersey, 1998.

[83] F. B. Seely, *Advanced mechanics of materials*, New York, Wiley; London, Chapman & Hall, 1932.

[84] S. S. H. Chen and L. Ta Ming “Extensional vibration of thin plates of various shapes,” in *Journal of Acoustic Society American*, vol. 58, no. 4, pp. 828–831, Oct. 1975.

[85] S. S. Rao, *Mechanical Vibration*, 4th edition, Upper Saddle River, N.J., Pearson Prentice Hall, 2004.

[86] J. J. Wortman and R. A. Evans, “Young’s modulus, shear modulus, and Poisson’s ratio in silicon and germanium,” in Journal of applied Physics, vol. 36, no.1, pp. 153-156, Jan. 1965.

[87] S. Pourkamali and F. Ayazi, "Fully Single Crystal Silicon Resonator with Deep-Submicron Dry-Etched Transducer Gaps," in *proceedings of IEEE/ASME Conference on Microelectromechanicalsystems (MEMS ‘04)*, Maastricht, the Netherlands, Jan. 2004, pp. 813-816.

[88] F. Ayazi, “A high aspect ratio high-performance polysilicon vibrating gyroscopes,” PhD. Thesis, in Electrical Engineering Department, University of Michigan, 2000.

[89] R. A. Johnson, *Mechanical Filters in Electronics*, New York: Wiley, 1983.

[90] Z. Hao and F. Ayazi, "Thermoelastic Damping in Flexural-Mode Ring Gyroscopes," in *ASME International Mechanical Engineering Congress and Exposition* (IMECE 2005), Orlando, FL, Nov. 2005.

[91] Duwel, J. Gorman, M. Weinstein, J. Borenstein and P. Ward, "Quality factors of MEMS gyros and the role of thermoelastic damping," in *proceedings of IEEE/ASME Conference on Microelectromechanicalsystems (MEMS '02)*, Los Vagas, NV, Jan. 2002, pp. 214-19.

[92] Duwel, J. Gorman, M. Weinstein, J. Borenstein and P. Ward, "Experimental study of thermoelastic damping in MEMS gyros," in *Sensors and Actuators A (Physical)*, vol. A103, no. 1-2, pp. 70-5, Jan. 2003.

[93] J. Yang, T. Ono and M. Esashi, "Energy dissipation in submicrometer thick single-crystal silicon cantilevers," in *Journal of Microelectromechanical Systems*, vol. 11, no. 6, pp. 775–783, Dec. 2002.

[94] W. Nowacki, *Dynamic Problems of Thermoelasticity*, Leyden: Noordhoof International, 1975.

[95] J. P. Gorman, "Finite element analysis of thermoelastic damping in MEMS," M.S. thesis, Material Science and Engineering Department, Massachusetts Institute of Technology (MIT), Cambridge, MA, 2002.

[96] Z. Hao, A. Erbil, and F. Ayazi, "An Analytical Model for Support Loss in Micromachined Beam Resonators with In-plane Flexural Vibrations," in *Sensors and Actuators A* (*Physical*), vol. A109, no. 1-2, pp. 156-164, Dec. 2003.

[97] R. Abdolvand, H. Johari, G.K. Ho, A. Erbil and F. Ayazi, "Quality Factor in Trench-Refilled Beam Resonators," in *IEEE Journal of Microelectromechanical Systems*, vol. 15, no. 3, pp. 471-8, June 2006.

[98] C. J. Glassbrenner and G. A. Slack, "Thermal conductivity of Si and Ge from 3°K to the melting point" in *Physics Review*, vol. 134, no. 4A, pp. A1058, May 1964.

[99] S. Okhotin, A. S. Pushkarskii, and V. V. Gorbachev, *Thermophysical Properties of Semiconductors*, Moscow, "Atom" Publ. House, 1972.

[100] M. F. Zaman, A. Sharma, B.V. Amini, and F. Ayazi, "Towards Inertial Grade Vibratory Microgyros: A High-Q In-Plane Silicon-On-Insulator Tuning Fork Device," in *Tech. Dig. Solid-State* Sensors*, Actuators, and* Microsystems Workshop, Hilton Head, SC, June 2004, pp. 384-385.

[101] L. Lea and C. short, "DRIE from MEMS to wafer-level packaging," in *Solid State Technology*, vol. 50, no. 12, Dec. 2007, pp. 58-60.

[102] F. Ayazi and K. Najafi, "High Aspect-Ratio Polysilicon Micromachining Technology," in *Tech. Digest of the International Conference on Solid-State Sensors and Actuators (Transducers '99)*, Sendai, Japan, June 1999, pp. 320-323.

[103] S. Pourkamali and F. Ayazi, "SOI-Based HF and VHF Single-Crystal Silicon Resonators with Sub-100 Nanometer Vertical Capacitive Gaps," in *Tech. Digest of the International Conference on Solid-State Sensors and Actuators (Transducers '03)*, Boston, MA, June 2003, pp. 837-840.

[104] H. Johari and F. Ayazi, "Silicon-On-Insulator Bulk Acoustic Wave Disk Resonators," in *Tech. Digest of IEEE Int. SOI Conference*, Niagara Falls, NY, Oct. 2006, pp. 153-154.

[105] N. Kim, et al., "Temperature dependence of quality factor in MEMS resonators," in *proceedings of IEEE/ASME Conference on Microelectromechanicalsystems* (MEMS'06), Istanbul, Turkey, Jan. 2006, pp. 590-593.

[106] M. W. Judy, "Evolution of Integrated Inertial MEMS Technology," in *Tech. Digest of Solid-State Sensors, Actuators and Microsystems Workshop*, Hilton Head Island, SC, June 2004, pp. 27-32.

[107] S. Lewis, et al, "Integrated sensor and electronics processing for >10^8 iMEMS inertial measurement unit components" in *Tech. Digest of International Electron Device Meeting (IEDM'03)*, Washington, DC, Dec. 2003, pp. 39.1.1-39.1.4.

[108] N. El-Sheimy, H. Hou and X. Niu, "Analysis and modeling of inertial sensors using Allan variance," *in IEEE Transactions on Instrumentation and Measurement*, vol. 57, no. 1, pp. 140-149, Jan. 2008.

[109] IEEE Recommended Practice for Inertial Sensor Test Equipment, Instrumentation, Data Acquisition, and Analysis, IEEE Std. 1554-2005,2005, pp. 1–103.

[110] M. Biel, G. Brandl, and R. T. Howe, "Young's modulus of in situ phosphorus-doped polysilicon," in *proceeding of Int. Conference on Solid-State Sensors and Actuators(Transducers '05)*, Stockholm, Sweden, June 1995, pp. 80–83.

[111] H. Johari, J. Shah and F. Ayazi, "High frequency xyz-axis single-disk silicon gyroscope," in *proceedings of IEEE/ASME Conference on Microelectromechanicalsystems (MEMS'08)*, Tucson, AR, Jan. 2008, pp. 856-9.

[112] G. Pickett, "Flexural vibration of unrestrained cylinders and disks," Journal of applied physics, vol. 16, pp. 820-831, Dec. 1945.